UNIVERSITA' DEGLI STUDI DI UDINE

Dottorato di Ricerca in Tecnologie Chimiche ed Energetiche

Ciclo XXVII

HEAT TRANSFER IN GASEOUS MICROFLOWS: CONJUGATE HEAT TRANSFER, RAREFACTION AND COMPRESSIBILITY EFFECTS

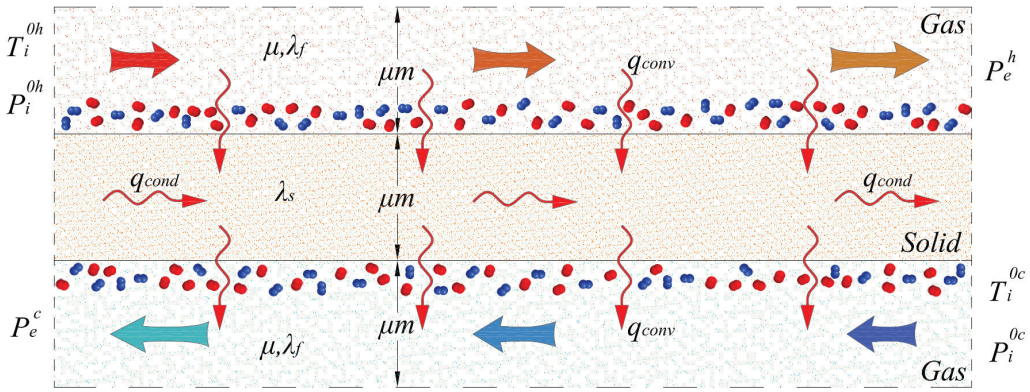

DOTTORANDO: Michele A. Coppola

COMMISSIONE

Prof. Marco Fossa	REVISORE
Prof. Gianluca Morini	REVISORE
Dott. Cristian Marchioli	COMMISSARIO
Prof. Sergio Chibbaro	COMMISSARIO
Dott. Paolo Gualtieri	COMMISSARIO
Prof. Giulio Croce	SUPERVISORE
Prof. Alfredo Soldati	COORDINATORE DEL DOTTORATO

Anno Accademico 2015

UNIVERSITA' DEGLI STUDI DI UDINE

Dottorato di Ricerca in Tecnologie Chimiche ed Energetiche

Ciclo XXVII

HEAT TRANSFER IN GASEOUS MICROFLOWS: CONJUGATE HEAT TRANSFER, RAREFACTION AND COMPRESSIBILITY EFFECTS

DOTTORANDO: Michele A. Coppola

COMMISSIONE

Prof. Marco Fossa	REVISORE
Prof. Gianluca Morini	REVISORE
Dott. Cristian Marchioli	COMMISSARIO
Prof. Sergio Chibbaro	COMMISSARIO
Dott. Paolo Gualtieri	COMMISSARIO
Prof. Giulio Croce	SUPERVISORE
Prof. Alfredo Soldati	COORDINATORE DEL DOTTORATO

Anno Accademico 2015

UDINE, printed in March 2016

ABSTRACT

The aim of the work presented in this thesis is to develop Conjugate Heat Transfer models in order to study the behavior of heat exchange in gaseous microflows. At the scales considered, rarefaction effects play a relevant role so that the need to involve slip flow boundary conditions is fundamental. Since the cases examined lie in the slip regime, a kinetic approach is not necessary.

The wide development of MEMS application, the very fast development in microfabrication technologies, and the increasing industrial applications of microfluidic systems, which are all taking place and evolving in the last decades, require a better knowledge of the behavior of microfluidic systems, especially of gases, which haven't been yet understood as well as liquid ones have. Flows that are involved in this realm have characteristic dimensions of the order of tens of micrometers.

The object of this work is essentially the investigation, and evaluation, of the characteristics and performances of forced convection in micro channels and of Micro Heat Exchangers.

In order to analyze what just introduced, a wide range of computational experiments (or numerical simulations) have been carried out using a Navier-Stokes solver for compressible flows, applying the appropriate boundary conditions.

The Reynolds numbers considered cover the laminar flow regime and the transitional zone. Turbulence has not been investigated here. The micro channels are 10 μm high and have a length to height ratio from 20 to 40, which is enough to study all the effects mentioned. Mach numbers are high enough to allow compressibility effects to appear but always remain in the subsonic regime.

One of the major results is that the importance of the axial conduction in the solid wall has been put in evidence. At microscale it greatly alters the linear distribution of the bulk temperature. Furthermore, another important result of this analysis is that the compressibility effects are remarkable, and in the literature there is really scarce data showing so.

For the micro heat exchanger, different sets of numerical simulations have been carried out using various conductivity ratios between solid and fluid. This allowed to determine axial conduction effects on the heat exchange. It is important to notice that infinite solid conductivity does not imply maximum heat transfer performances: it is easy to check that it simply corresponds to an efficiency of 0.5, lower than the expected values for standard counter current arrangement. Thus, the values are appropriately chosen in order to obtain interesting conjugate heat transfer results that do not yield an efficiency higher than 0.5.

Results show that an optimum axial number exists, although the efficiency is not much greater than 0.5, concluding that a quite low limit exists in these micro devices. Moreover, it has been proven that countercurrent and parallel flow configurations have similar performances.

Finally, it is proved that it is possible to derive a general correlation for the local Stagnation Nusselt number, which is in good agreement with all the results obtained in this study, and it has been proven that it works for the convection heat transfer cases with compressibility effects in the Micro Heat Exchanger.

CONTENTS

NOMENCLATURE

a	speed of sound, [m/s]
CHT	Conjugate Heat Transfer
C_p	specific heat at constant pressure, [J/kg K]
C_v	specific heat at constant volume, [J/kg K]
d	molecular diameter
D_h	hydraulic diameter, [m]
e	energy, [J]
Eck	Eckert number, dimensionless
f	viscous stress tensor
F	convective fluxes tensor
F_v	diffusive terms tensor
h	specific enthalpy, [J/Kg]
H	channel height, [μm]
HEX	Heat Exchanger
i	number of nodes along x, dimensionless
I	Identity matrix, dimensionless
j	number of nodes along y, dimensionless
Kn	Knudsen number, dimensionless
l	mean free path, [m]
L	characteristic length/channel length, [m]
$\dot{m}$	mass flow rate, [kg/s]
$\dot{m}'$	mass flow rate per unit depth, [kg/s·m]
M	axial number (Maranzana number), dimensionless
Ma	Mach number, dimensionless
$\mathbf{n}$	normal unit vector
NS	Navier-Stokes
Nu	Nusselt number, dimensionless
Nu,st	Stagnation Nusselt number, dimensionless

p	pressure, [Pa]
Pr	Prandtl number, dimensionless
q	vector of the conservative variables
q'	heat flux per unit depth, [W/m]
q''	specific heat flux, [W/m^2]
R	molar gas constant, [J/mol K]
Re	Reynolds number, dimensionless
s	wall thickness, [µm]
S_T	temperature jump coefficient, dimensionless
S_p	slip coefficient, dimensionless
$\mathbf{t}$	tangent unit vector
T	temperature, [K]
u	streamwise velocity, [m/s]
U	internal energy, [J]
v	transverse velocity, [m/s]
V	volume, [m^3]
w	velocity along the coordinate z, [m/s]
$\vec{w}$	velocity vector *(u,v,w)*, [m/s]
x	streamwise coordinate, [m]
y	normal coordinate, [m]
z	third spatial coordinate, [m]

Greek Symbols

α	heat transfer coefficient, [W/m^{2}K]
β	pressure ratio $\beta = p_i^0 / p_e$
ε	heat sink and heat exchanger efficiency, dimensionless
ε'	isentropic heat sink performance, dimensionless
λ	conductivity, [W/m K]
Λ	solid/fluid conductivity ratio, dimensionless
ϑ	time, [s]
γ	specific heat ratio, dimensionless

μ	gas viscosity, [kg/ms]
ρ	density, [kg/m^3]
σ_T	temperature accommodation coefficient
σ_v	part of incident particles scattered diffusely
τ	non dimensional temperature ratio
τ_{ii}	viscous stress components, $i=x,y,z$
φ	non dimensional temperature ratio for correlation
$\dot{\varphi}$	work of the friction forces term
ω_i	characteristic variables

Subscripts

b	bulk (mass flow averaged)
cond	conductive
conv	convective
e	exit
f	fluid
g	global
i	inlet
is	isentropic
n	normal
s	solid
t	tangential
tot	total
x	at generic *x* position
w	wall

Superscripts

0	stagnation conditions
c	cold stream
h	hot stream

CHAPTER 1 : INTRODUCTION

Micro and nano scaled technologies have gained great interest in both industrial and academic environments in the past fifteen years. Major application ranges from biomedical to electronic cooling, and in most of these systems the fluid flow and heat transfer correct prediction is a critical step in the design process.

In particular, the use of micro channels for the heat removal is raising a great interest in various industrial fields, such as electronics, micro heat exchangers and bio-engineering. This type of cooling inherently offers high performances in heat transfer, due to the high achievable surface to volume ratio. Thus, the dimensions of channels constituting miniaturized cooling systems, for instance mounted on electronic components, may be as low as of the order of a few microns. Furthermore, although liquid and phase changing fluids offers better heat transfer performances, gas is often used as working fluid.

Several scaling effects thus must be taken into account: as an example, obvious manufacturing constraints imply that most micro channels are characterized by thick walls, and this induces relevant heat conduction through the micro tube walls, as pointed out by several literature references. This has an effect on the heat transfer device performances, and Conjugate Heat Transfer (CHT), combining convective heat transfer in the fluid with conduction through the solid (axial conduction), plays an important role at microscale.

1.1 CHT and Micro HEX state of the art

In recent years, a number of papers in open literature (see as examples [1-4]) were devoted to the detection, analysis and prediction of CHT effects.

An exhaustive literary review on CHT in micro heat exchanger may be found in the article of Yahui, Morini and Brandner [1]. They report that the influence of wall axial conduction on the thermal performance of micro heat exchangers has been

studied by a number of researchers in the past: Peterson [5] numerically examined the CHT effects in microchannels and suggested to use material of very low thermal conductivity in the construction of counter-current micro heat exchangers in order to avoid strong axial conduction across the partition wall. Stief et al. [6] determined numerically the optimal value of the thermal conductivity of the walls of a micro heat exchanger in order to obtain the maximum value of the thermal efficiency; they demonstrated that for counter-current flow configuration the best performance cannot be achieved using materials characterized by very large thermal conductivity, due to the remarkable conjugate heat transfer effects. Such result has been confirmed by Moreno et al. [7], in fact they observed that materials with high thermal conductivity tend to decrease the thermal efficiency of micro heat exchangers. Hung et al. [8] showed numerically that the fluid experiences larger temperature change if the substrate of the micro heat exchanger is made of material with low thermal conductivity. Koyama and Asako [9] proved numerically that the reduction of the partition wall thickness, between the hot and the cold flow, allows for higher thermal performance of gas-to-gas micro heat exchangers by reducing the conjugate effects between the solid wall and the fluids. In the case of micro heat exchangers operating with liquids, from an experimental point of view, many works do not report whether axial conduction is important in the thermal efficiency of the devices [10,11,12,13]. Contrarily, in the experimental tests of gas micro heat exchangers, the influence of axial conduction has always been recognized as crucial for the optimization of the thermal performance of these devices.

One of the first works on experimental analysis of gas-to-gas micro heat exchangers was carried out by Bier et al. [14], who found that gas micro heat exchangers work like a temperature mixer between hot and cold flows if the partition wall is highly conductive. Meschke et al. [15] showed experimentally lower values of the heat transfer coefficient with respect to the theoretical predictions, based on conventional theory in a ceramic gas micro heat exchanger.

They also explained such reduced values by invoking the strong axial CHT effects across the thick solid walls of their device. Similar conclusions were drawn by Koyama and Asako [16] by conducting a series of experiments with stainless steel gas micro heat exchangers. In their work no significant difference in terms of thermal

performance was found between co-current and counter-current flow arrangement and their main conclusion was that the flow configuration has a negligible influence on the efficiency of gas micro HEX, if strong conjugate effects are present.

Figure 1.1: Examples of stainless steel microscale heat exchangers for process engineering.

What just briefly reported on gas micro heat exchangers puts in evidence how many researchers found that the thermal performance of these devices is degraded by the presence of a significant axial conduction across the partition walls. However, the results reported in these works are not sufficient in order to have a deeper systematic insight into the influence of axial conduction on the performance of gas micro heat exchangers because, although the experimental conditions vary from one work to another, they are far to cover all the cases of interest.

The work carried out in [1] has been done in order to achieve more results that could fill the gap, by means of a parametric experimental analysis of the influence of the conjugate heat transfer on the performance of gas micro heat exchangers using a specific double-layered microchannel heat exchanger, which was presented by the

same authors in [17]. The hot and cold layers of the micro heat exchanger were manufactured into polished PEEK material with large thermal resistance in order to minimize the heat losses. The layers could be rotated in order to transform the heat exchanger in cross flow or counter current flow or parallel flow configuration. The partition foil between the two layers was designed to be exchangeable; in this way it became possible to test different partition foils made with different materials and thicknesses, allowing for comparative study of the influence of axial conduction on thermal performance. In this way the role of the axial conduction across the partition foil has been experimentally investigated for different flow configurations and the results have been compared with the predictions of the correlations developed for the design of conventional-sized heat exchangers [18,19].

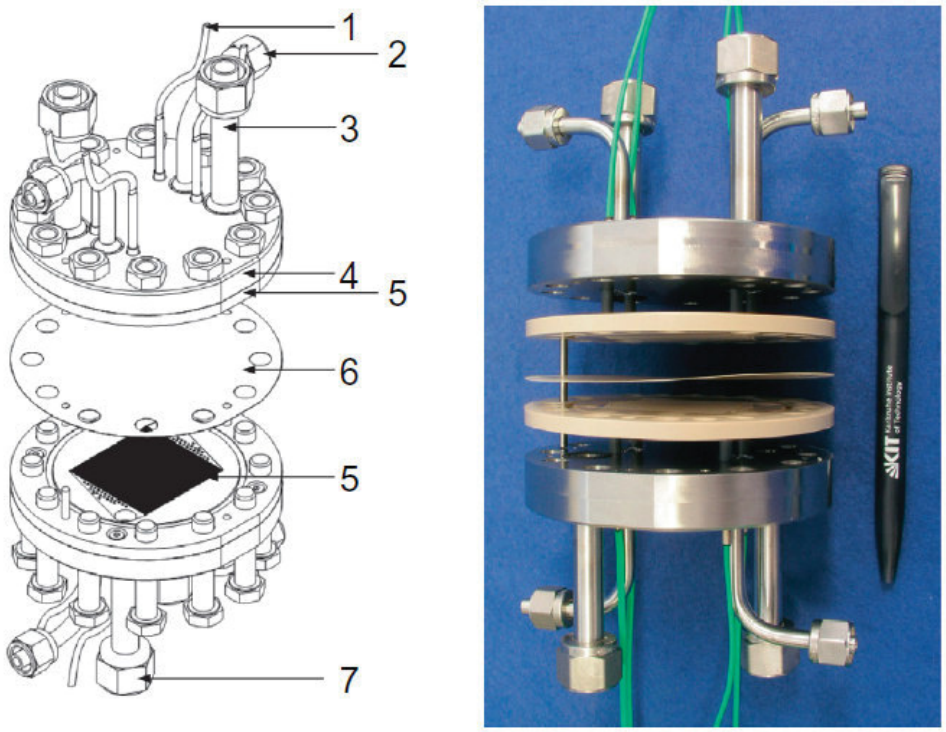

Figure 1.2: Exploded lay-out of the double-layered micro heat exchanger and picture of the manufactured device.

1.2 Heat transfer in Microflows main features

In the context of uncompressible flows it is relatively easy to separate convection and conduction, due to the decoupling of thermal and velocity fields. Thus, the theoretical framework under such conditions is well developed. The importance of CHT can be estimated via a significant non dimensional parameter M identified by Maranzana [5], the axial conduction parameter, which quantifies the magnitude of the axial conduction effect through the walls. Such parameter is given by the ratio between the total convective heat flux and a representative axial conductive flux through the walls, for a fixed inlet/outlet temperature difference.

The device heat transfer performances can be obtained via simplified approaches. The standard procedure for macro scale applies one-dimensional (perpendicular to the flow) heat conduction in the wall. This allows easy modeling in the case of constant convective heat transfer coefficient, and in general avoids the need for fully Conjugate Heat Transfer (CHT) computation whenever such coefficient is known. An example of such approach, compared to full CHT, is given by Croce et al. [21]. A step forward, much more suited to micro scale geometries, is obtained by neglecting the solid temperature gradients normal to the flow, but solving a one dimensional conduction problem in the streamwise direction, as in [22]; furthermore, fully analytical 2D solutions are available for plane channels [20].

On the other hand, gaseous flows, especially at small scales, offer a more challenging configuration. In particular, thermal and velocity fields are closely coupled, and the above mentioned uncoupled models may not be adequate: hence, the evolution of the flow temperature field is a result of both heat transfer and the conversion between internal (i.e. thermal) and kinetic energy. The flow cooling due to the gas acceleration through a microchannel can be significant at either high pressure ratios, inducing high Mach number levels, or at low heat transfer rate. In such cases, care should be taken in the proper definition of the standard heat transfer devices performance parameters, such as the Nusselt number or Heat Sink efficiency measures: the mere transposition of uncompressible flow definition, in fact, may lead to unphysical negative or unbounded, infinite values. Furthermore, at smaller scales, the mean free path of molecules of the gas is of the order of the hydraulic diameter of

the channel, so rarefaction cannot be neglected: slip flow along the wall, as well as temperature jump, does typically decrease the actual device properties. Short channels emphasize most of the above mentioned effects, while in longer ones usually the compressible flow features are confined to a relatively short exit section.

1.3 An overview on the work presented

The wall axial conduction effect on gaseous heat transfer in short channels, i.e. in presence of remarkable rarefaction and compressibility effects, has not been extensively studied yet, and part of the present work is meant to partially fill this gap.

Therefore, in this thesis, we consider at first short plane channels subjected to constant heat flux boundary conditions in a range of moderate Kn number, allowing for the modeling via Navier Stokes equations and the first order slip and temperature jump boundary conditions. The geometrical configuration was already analyzed in [23], and here we focus on low flux, high compressible flows, and is representative of the use of microchannel as a heat sink device, where the main objective is to efficiently remove as much heat as required to keep a solid substrate at a relatively low temperature.

Slip boundary is modeled with a general formulation of the classical first order boundary condition proposed by Maxwell. The investigated range of Knudsen numbers, which are related to the rarefaction, is kept within the limits of applicability of such boundary condition, which cover most of the practical engineering applications. It should be reminded, however, that smaller scale details (such as roughness) effects may require more sophisticated and computationally expensive tools [24]. Viscous dissipation is also taken into account.

The whole length of the channel is simulated, since compressibility and border effects for the axial conduction through the wall exclude the possibility of fully developed flow.

A compressible finite volume flow solver, suitable for high Mach number flows, is applied to full conjugate heat transfer analysis of the problem, investigating the

combined effects of rarefaction, compressibility and axial conduction through the channel walls, thus, taking into account all the effects involved that have been described above.

The main aim is to describe and find suitable parameters to estimate the microchannel heat transfer performances in presence of significant temperature drops related to flow expansion, were the standard definition of Nusselt and/or Heat Sink efficiency may yield misleading values.

The results are thus presented for Nusselt number, the Heat Sink efficiency, resulting wall temperature and a new definition of the heat sink performance which is found to well apply and describe performances of compressible flows.

The same approach and simulation tools are then applied to the analysis of Micro Heat Exchangers configuration, where the main goal is the heat transfer between two different flow streams. Again, heat transfer between gaseous flows (i.e. compressible flows) is considered, in order to achieve a better knowledge of their performances with all the typical effects of the micro scale.

The micro heat exchangers are of increasing interest, for their improved heat exchange capacities due to very large surface-to-volume ratio. The applied research on micro channel heat exchangers using liquid as working media can be considered mature, even though some of the results are not in agreement. But compared with research on liquid flow micro heat exchangers, experimental investigations on gas flows in these devices is relatively scarce [25,26,27].

Even if the hydraulic diameter of the flow passages in micro heat exchangers can be greatly reduced thanks to microfabrication technologies, the partition walls between the flow passages cannot be excessively thin, in order to maintain an adequate mechanical strength. This mechanical constraint makes the partition walls of the micro heat exchangers considerably thicker (in comparison with the hydraulic diameters) than their conventional macroscale counterparts. This physical feature may results, again, in strong wall-fluid conjugate heat transfer effects which influence the thermal performance of micro heat exchangers, especially if the partition walls are made of solid material with a large thermal conductivity.

In order to determine the characteristics of these micro devices, it is necessary, first of all, to fully understand the behavior and the performance of the conjugate heat transfer between two microchannels with the presence of the solid partition wall (CHT). Once these characteristics are well characterized it is possible to better understand the operation of a whole micro heat exchanger.

The dimensions here considered are of the same order of those studied in the heat sink cases and the performances are analyzed in both parallel and counter current configurations. Rarefaction and compressibility effects are still considered.

The results are reported in terms of efficiency and heat transfer coefficients for different cases of CHT (solid/fluid conductivity ratio), pressure drops, inlet temperature and channel length.

The analysis and the data collected from the simulations lead to the derivation of a correlation for the local Nusselt number, as a function of only local parameters, taking into account both compressibility and rarefaction. Such correlation is an essential tool required to develop 3D models, e.g. porous media models, which will help to optimize the design of an entire heat exchanger endowed with micro channels.

CHAPTER 2 : MICRO COMPRESSIBLE FLOWS

A good knowledge of the behavior of compressible flows in the micro scale realm, with the equations and theories applied to describe them, is fundamentally important to understand what is illustrated in this thesis. Moreover, without introducing these concepts, it is hard to deeply understand what kind of numerical models, and why, are adopted to simulate what is studied.

In order to obtain so, an illustration of the following topics will be presented in this chapter:

- Convection in Compressible flows equations;
- Rarefied flows and Slip flow;
- Conjugate Heat Transfer.

2.1 Convection in compressible flow equations

2.1.1 Introduction

In this subchapter convection processes that originate in fluids with a compressible behavior are discussed. For such fluids, the density variations are no longer negligible, unlike to what applies for incompressible fluids. The transformation from kinetic energy to thermal energy, and vice versa, play a fundamental role in the flows involved, thus dynamic and thermal domains are strongly coupled. Hence continuity, momentum and energy equations have to be solved simultaneously.

Nevertheless, the equations, and therefore the numerical schemes, must thoroughly describe phenomena typical of gas dynamics such as shock waves and chocked conditions.

From a mathematical point of view the density variations permit to write the continuity equations in a mass transport form completely equivalent, except for the absence of diffusive terms, to the momentum and energy transport equations. It is thus possible to select as independent variables the velocity, temperature and density, or their appropriate combinations, and algebraically calculate the pressure from the values of temperature and density with the equation of state of the gas. As a result one of the main problems in modeling the Navier-Stokes equations for incompressible flows is solved: the necessity of the introduction of an appropriate differential equation for the pressure.

Furthermore, new difficulties rise in the formulation of the convective terms which may result dominant with respect to the diffusive ones as, normally, fluxes with a high Mach number are also characterized by a high Reynolds number. As a consequence, the solution algorithms for compressible flows derive from algorithms used for the Euler equations, in which the diffusive terms are neglected.

A special attention to the direction of propagation of the perturbations must be paid, in order to correctly define the boundary conditions, both physical and numerical.

Finally, the presence of discontinuities in the flow field, such as the ones generated by shock waves, require special care. The choice of the independent variables must take into account the existence of the discontinuities, favouring a formulation in terms of the conservative variables.

2.1.2 Equations of motion of a compressible fluid

The equations that govern the thermal field and motion of a compressible fluid are summarized below. The continuity equation will have its general form, that is:

$$\frac{\partial \rho}{\partial \vartheta} + \nabla \cdot (\rho \vec{w}) = 0 \tag{2.1}$$

The momentum equation is normally expressed in its conservative form:

$$\frac{\partial}{\partial \vartheta}(\rho \vec{w}) + \nabla \cdot (\rho \vec{w} \vec{w}) = -\nabla p + \nabla f + \rho \vec{g} \tag{2.2}$$

where f represents the viscous stress tensor that for a laminar flow has the following expression:

$$f = \mu[\nabla \vec{w} + (\nabla \vec{w})^T] + \mu(\nabla \vec{w}) \cdot I \tag{2.3}$$

and I is the identity matrix. Respect to the incompressible formulation, a second term appears related to the non zero divergence of the velocity field. Introducing the Stokes relation

$$\mu_\lambda = -\frac{2}{3}\mu \tag{2.4}$$

the viscous terms can be explicated for the compressible flow in the laminar regime. In the three dimensional case the viscous stress tensor assumes the following form:

$$f = \mu \begin{bmatrix} 2\frac{\partial u}{\partial x} - \frac{2}{3}(\nabla \cdot \vec{w}) & \frac{\partial u}{\partial y} + \frac{\partial v}{\partial x} & \frac{\partial u}{\partial z} + \frac{\partial w}{\partial x} \\ \frac{\partial u}{\partial y} + \frac{\partial v}{\partial x} & 2\frac{\partial v}{\partial y} - \frac{2}{3}(\nabla \cdot \vec{w}) & \frac{\partial v}{\partial z} + \frac{\partial w}{\partial y} \\ \frac{\partial u}{\partial z} + \frac{\partial w}{\partial x} & \frac{\partial v}{\partial z} + \frac{\partial w}{\partial y} & 2\frac{\partial w}{\partial z} - \frac{2}{3}(\nabla \cdot \vec{w}) \end{bmatrix} = \begin{bmatrix} \tau_{xx} & \tau_{xy} & \tau_{xz} \\ \tau_{yx} & \tau_{yy} & \tau_{yz} \\ \tau_{zx} & \tau_{zy} & \tau_{zz} \end{bmatrix} \tag{2.5}$$

Since in most of the applications with high velocity flow the natural convection term is negligible, the buoyancy term ρg will be omitted from now on. Thus, eq. (2.2) assumes the following:

$$\frac{\partial}{\partial \vartheta}(\rho\vec{w}) + \nabla \cdot (\rho\vec{w}\vec{w} + pI) - \nabla f = 0$$

or

$$\frac{\partial}{\partial \vartheta}(\rho\vec{w}) + \nabla \cdot [(\rho\vec{w}\vec{w} + pI) - f] = 0 \tag{2.6}$$

The energy equation will also be expressed in a conservative formulation, but however, the viscous term and the kinetic energy variations are no longer negligible. The potential energy variation, normally, results irrelevant. In the first principle general expression, applied to a generic fluid domain, the internal energy must be substituted with the global internal energy, such that:

$$U_g = \int_V \left(\rho\hat{u} + \rho\frac{w^2}{2} \right) dV = \int_V \rho\hat{u}_g \, dV \tag{2.7}$$

and consequently the global internal energy per mass unit u_g is defined. Considering the kinetic energy fluxes that enter and exit the domain, we can write the following equation:

$$\frac{\partial Ug}{\partial \vartheta} = \sum \dot{m}_i \left(\bar{h}_i + \frac{w_i^{\,2}}{2} \right) - \left(\bar{h}_e + \frac{w_e^{\,2}}{2} \right) + q + \dot{\varphi} = 0 \tag{2.8}$$

in which the work of the friction forces term $\dot{\varphi}$ has, in general, the following expression:

$$\dot{\varphi} = \nabla \cdot (f \cdot \vec{w}) \tag{2.9}$$

The sum of specific enthalpy and specific kinetic energy is defined as total enthalpy or stagnation enthalpy h^0:

$$h^0 = \left(h + \frac{k^2}{2} \right) \tag{2.10}$$

The last quantity, that physically represents the enthalpy that the fluid would have if arrested in a isentropic way, is of remarkable importance in the study of gas dynamics.

Following the procedure used to obtain the energy equation for incompressible flows, which is available in literature, the complete energy equation for compressible flows can be deduced as showed below:

$$\frac{\partial}{\partial \vartheta}(\rho \hat{u}_g) + \nabla \cdot (\rho \vec{w} h^0) = \nabla \cdot (f \cdot \vec{w}) + \nabla \cdot (\lambda \nabla \cdot T) \tag{2.11}$$

or else

$$\frac{\partial}{\partial \vartheta}(\rho \hat{u}_g) + \nabla \cdot [(\rho \vec{w} h^0) - f \cdot \vec{w} - \lambda \nabla \cdot T] = 0 \tag{2.11}$$

It's easy to notice that the continuity equation (2.1), the momentum equation (2.6) and the last (2.11) have the same mathematical structure and, therefore, can be expressed all together in a general form as follows:

$$\frac{\partial q}{\partial \vartheta} + \nabla \cdot [F - F_v] = 0 \tag{2.12}$$

In the last expression (2.12) q is a vector and it represents the vector of the conservative variables:

$$q = \begin{Bmatrix} \rho \\ \rho \vec{w} \\ \rho \hat{u}_g \end{Bmatrix} \tag{2.13}$$

whilst the convective fluxes are indicated with F:

$$F = \begin{Bmatrix} \rho\vec{w} \\ \rho\vec{w}\vec{w} + pI \\ \rho\vec{w}h_0 \end{Bmatrix} \tag{2.14}$$

The (2.14) can be explicated with its own components:

$$F = \begin{Bmatrix} \rho\vec{w} \\ \rho\vec{w}\vec{w} + pI \\ \rho\vec{w}h_0 \end{Bmatrix} = \left\{ \begin{bmatrix} \rho u \\ \rho u^2 + p \\ \rho uv \\ \rho uw \\ \rho uh_0 \end{bmatrix} \begin{bmatrix} \rho v \\ \rho uv \\ \rho v^2 + p \\ \rho vw \\ \rho vh_0 \end{bmatrix} \begin{bmatrix} \rho w \\ \rho uw \\ \rho vw \\ \rho w^2 + p \\ \rho wh_0 \end{bmatrix} \right\} = \begin{Bmatrix} F_x & F_y & F_z \end{Bmatrix} \tag{2.15}$$

The diffusive terms appear in the tensor F_v:

$$F_v = \begin{Bmatrix} 0 \\ f \\ f \cdot \vec{w} + \lambda\nabla T \end{Bmatrix} \tag{2.16}$$

which may be also explicated with its own components as below:

$$F_v = \begin{Bmatrix} 0 \\ f \\ f \cdot \vec{w} + \lambda\nabla T \end{Bmatrix} = \begin{Bmatrix} F_{vx} & F_{vy} & F_{vz} \end{Bmatrix} \tag{2.17}$$

where

$$F_{vx} = \begin{bmatrix} 0 \\ \tau_{xx} \\ \tau_{xy} \\ \tau_{xz} \\ u\tau_{xx} + v\tau_{xy} + w\tau_{xz} + \lambda\dfrac{\partial T}{\partial x} \end{bmatrix}$$

$$F_{vy} = \begin{bmatrix} 0 \\ \tau_{xy} \\ \tau_{yy} \\ \tau_{yz} \\ u\tau_{xy} + v\tau_{yy} + w\tau_{yz} + \lambda \dfrac{\partial T}{\partial y} \end{bmatrix}$$

$$F_{vz} = \begin{bmatrix} 0 \\ \tau_{xz} \\ \tau_{xz} \\ \tau_{zz} \\ u\tau_{xz} + v\tau_{yz} + w\tau_{zz} + \lambda \dfrac{\partial t}{\partial z} T \end{bmatrix} \tag{2.18}$$

In the convective terms and in the expression of the total enthalpy the static pressure appears, which has to be calculated with the equation of state of the gas starting from the values of ρ and u_g calculated with the equations. For an ideal gas model the internal energy can be expressed as $\hat{u} = c_v T$, indicating with T the absolute temperature. The equation of state of the gas, hence, can be written as follows:

$$p = \frac{\rho}{\gamma - 1}\left[\hat{u}_g - \frac{1}{2}(u^2 + v^2 + w^2)\right] \tag{2.19}$$

with γ denoting the specific heat ratio $\gamma = c_p / c_v$. The temperature T is:

$$T = \frac{1}{c_v}\left[\hat{u}_g - \frac{1}{2}(u^2 + v^2 + w^2)\right] \tag{2.20}$$

It is important to notice how the energy equation (2.11) is tightly coupled with the equations of motion and with the continuity equation, both because the pressure p appears in it (in the total enthalpy expression h^0), and for the connection between temperature and density imposed by the equation of state of the gas. This is the

reason why continuity, momentum and energy equations are often solved simultaneously.

From equation (2.12) it is possible to explicate the 5 scalar equations that form the system:

$$\frac{\partial \rho}{\partial \vartheta} + \frac{\partial(\rho u)}{\partial x} + \frac{\partial(\rho v)}{\partial y} + \frac{\partial(\rho w)}{\partial z} = 0 \tag{2.21}$$

$$\frac{\partial(\rho u)}{\partial \vartheta} + \frac{\partial(\rho u^2 + p)}{\partial x} + \frac{\partial(\rho uv)}{\partial y} + \frac{\partial(\rho uw)}{\partial z} - \frac{\partial \tau_{xx}}{\partial z} - \frac{\partial \tau_{xy}}{\partial z} - \frac{\partial \tau_{xz}}{\partial z} = 0 \tag{2.22}$$

$$\frac{\partial(\rho u)}{\partial \vartheta} + \frac{\partial(\rho uv)}{\partial x} + \frac{\partial(\rho v^2 + p)}{\partial y} + \frac{\partial(\rho vw)}{\partial z} - \frac{\partial \tau_{xy}}{\partial z} - \frac{\partial \tau_{yy}}{\partial z} - \frac{\partial \tau_{yz}}{\partial z} = 0 \tag{2.23}$$

$$\frac{\partial(\rho u)}{\partial \vartheta} + \frac{\partial(\rho uw)}{\partial x} + \frac{\partial(\rho vw)}{\partial y} + \frac{\partial(\rho w^2 + p)}{\partial z} - \frac{\partial \tau_{xz}}{\partial z} - \frac{\partial \tau_{yz}}{\partial z} - \frac{\partial \tau_{zz}}{\partial z} = 0 \tag{2.24}$$

$$\begin{aligned} &\frac{\partial \rho \hat{u}_g}{\partial \vartheta} + \frac{\partial \rho u h^0}{\partial x} + \frac{\partial \rho v h^0}{\partial y} + \frac{\partial \rho w h^0}{\partial z} \\ &- \frac{\partial \rho \left(u\tau_{xx} + v\tau_{xy} + w\tau_{xz} + \lambda \frac{\partial T}{\partial x} \right)}{\partial x} \\ &- \frac{\partial \rho \left(u\tau_{xy} + v\tau_{yy} + w\tau_{yz} + \lambda \frac{\partial T}{\partial y} \right)}{\partial y} \\ &- \frac{\partial \rho \left(u\tau_{xz} + v\tau_{yz} + w\tau_{zz} + \lambda \frac{\partial T}{\partial z} \right)}{\partial z} = 0 \end{aligned} \tag{2.25}$$

The structure of equation (2.12) permits to decouple the spatial discretization from the time discretization. In most algorithms the spatial derivatives are discretized in the first place, by transforming the gradient of the flux vectors in an appropriate algebraic expression. The remaining equation is an ordinary differential equation in

which only the time derivative appears. Such equation can be solved with standard numerical methods (e.g. explicit Runge Kutta or implicit Euler method).

The equations just derived are valid for laminar flows. For turbulent flows, that frequently occur in high speed gaseous flows (at least in macro scale), the Reynolds tensors must be appropriately modeled. In the simplest case, the effect of the turbulence can be described adding to the laminar coefficients μ and λ the turbulent contributions μ_t and λ_t .

2.1.3 Disturbances propagation and boundary conditions

As already mentioned, in high speed flows the convective terms are rather relevant. Therefore, it is interesting to perform an analysis of the propagation direction of the perturbations on the base of Euler's equations for non viscous flows:

$$\frac{\partial q}{\partial \vartheta} + \nabla \cdot F = 0 \tag{2.26}$$

which are obtained from the Navier Stokes equations with the Reynolds number that tends to infinity. The considerations that we will obtain allow to set correctly the boundary conditions for various flow regimes.

Let's consider the quasi linear form of the Euler equations:

$$\frac{\partial q}{\partial \vartheta} + (\mathrm{A} \cdot \nabla) q = 0 \tag{2.27}$$

explicable as

$$\frac{\partial q}{\partial \vartheta} + \mathrm{A}_x \frac{\partial q}{\partial x} + \mathrm{A}_y \frac{\partial q}{\partial y} + \mathrm{A}_z \frac{\partial q}{\partial z} = 0 \tag{2.27}$$

where A contains the Jacobian matrices of the tensor F defined by (2.14, 2.15):

$$\mathrm{A} = \frac{\partial F}{\partial q} = \left\{ \mathrm{A}_x \quad \mathrm{A}_y \quad \mathrm{A}_z \right\} = \left\{ \frac{\partial F_x}{\partial q} \quad \frac{\partial F_y}{\partial q} \quad \frac{\partial F_z}{\partial q} \right\} \tag{2.28}$$

For an ideal gas the homogeneity condition appears, that is:

$$F = \mathrm{A}q \tag{2.29}$$

It can be proved that the Euler equations system (2.27) is hyperbolic and admits a complete set of real eigenvalues. This allows to individuate specific directions (or characteristic directions) along which the information propagate with velocities given by the eigenvalues of the system.

In particular, once a unit vector n in space is chosen, the eigenvalues Λ_i of the system may be obtained from the solution of the characteristic equation

$$\det\left|\Lambda \mathrm{I} - \mathrm{A} \cdot n\right| = 0 \tag{2.30}$$

The solution of eq. (2.30) yields 5 eigenvalues Λ_i valid for an ideal gas:

$$\begin{aligned} \Lambda_1 &= \Lambda_2 = \Lambda_3 = w \cdot n \\ \Lambda_4 &= w \cdot n + a \\ \Lambda_5 &= w \cdot n - a \end{aligned} \tag{2.31}$$

where a is the speed of sound:

$$a = \sqrt{\gamma R T} = \sqrt{\frac{\gamma p}{\rho}} \tag{2.32}$$

Solving the homogeneous system associated to the eq. (2.30):

$$\left(\Lambda_i \mathrm{I} - \mathrm{A} \cdot n\right) l_i = 0 \tag{2.33}$$

the 5 eigenvectors l_i are obtained. With the eigenvectors it is possible to build the matrix L^{-1} with the vectors on each row and then it can be proved that the matrix $\mathrm{A}\cdot n$ is diagonalizable, such that:

$$L^{-1}(\mathrm{A}\cdot n)L=\Lambda \qquad\qquad L\Lambda L^{-1}=\mathrm{A}\cdot n \tag{2.34}$$

where Λ is a diagonal matrix:

$$\Lambda=\begin{Bmatrix}\Lambda_1 & 0 & 0 & 0 & 0\\ 0 & \Lambda_2 & 0 & 0 & 0\\ 0 & 0 & \Lambda_3 & 0 & 0\\ 0 & 0 & 0 & \Lambda_4 & 0\\ 0 & 0 & 0 & 0 & \Lambda_5\end{Bmatrix} \tag{2.35}$$

Projecting the initial system along the eigenvectors the following expression is obtained

$$L^{-1}\frac{\partial q}{\partial \vartheta}+L^{-1}\mathrm{A}\nabla q=0 \tag{2.36}$$

Defining the variable substitution

$$\delta\omega=L^{-1}\delta q \qquad\qquad \delta q=L\delta\omega \tag{2.37}$$

where δ(.) denotes an infinitesimal variation, and then substituting in eq (2.36)

$$L^{-1}\frac{\partial q}{\partial \vartheta}+\left(L^{-1}\mathrm{A}L\right)L^{-1}\nabla q=0 \tag{2.38}$$

the characteristic equations are obtained:

$$\frac{\partial \omega}{\partial \vartheta}+\left(L^{-1}\mathrm{A}L\right)\cdot\nabla\omega=0 \tag{2.39}$$

The last equations still form a system of coupled equations, as it is possible to diagonalize any linear combination of A_x, A_y and A_z, but not the matrices simultaneously. However, the (2.39) provide essential information. Let's consider a one-dimensional flow, for which the derivates along two of the three dimensions cancel, for instance *y* and *z*, so that the (2.27) reduces to:

$$\frac{\partial q}{\partial \vartheta} + \mathrm{A}_x \frac{\partial q}{\partial x} = 0 \tag{2.40}$$

By choosing the unit vector **n** parallel to the *x* axis we get

$$L^{-1}(\mathrm{A} \cdot n)L = L^{-1}(\mathrm{A}_x)L = \Lambda \tag{2.41}$$

and thus the system reduces to 5 decoupled equations in the new variables, defined as the characteristic variables, ω_i:

$$\frac{\partial \omega_i}{\partial \vartheta} + \Lambda_i \frac{\partial \omega_i}{\partial x} = 0 \qquad\qquad i = 1,..,5 \tag{2.42}$$

each of which represents the propagation equation of a wave in the *x* direction, with velocity Λ_i. The characteristic variables, for an ideal gas, are given by:

$$\delta\omega = \begin{bmatrix} \delta\omega_1 \\ \delta\omega_2 \\ \delta\omega_3 \\ \delta\omega_4 \\ \delta\omega_5 \end{bmatrix} = \begin{bmatrix} \delta\rho - \dfrac{\delta p}{a^2} \\ \delta v \\ \delta w \\ \delta u + \dfrac{\delta p}{\rho a} \\ -\delta u + \dfrac{\delta p}{\rho a} \end{bmatrix} \tag{2.43}$$

The 5 characteristic variables have precise physical meaning: ω_1 corresponds to an entropy wave, as using the definition of speed of sound (2.32) we have:

$$
\begin{aligned}
s_1 - s_2 &= c_v \ln\left(\frac{p_1}{p_2}\left(\frac{\rho_2}{\rho_1}\right)^{\gamma}\right) \\
ds &= c_v \frac{dp}{p} - \gamma c_v \frac{d\rho}{\rho} = \gamma c_v \frac{dp}{\rho a^2} - \gamma c_v \frac{d\rho}{\rho} = -\frac{\gamma c_v}{\rho}\left(d\rho - \frac{dp}{a^2}\right)
\end{aligned}
\tag{2.44}
$$

ω_2 and ω_3 correspond to the velocity transport, ω_4 and ω_5 represent the two acoustic waves.

As in the present one-dimensional case the (2.31) reduce to:

$$
\begin{aligned}
&\Lambda_1 = \Lambda_2 = \Lambda_3 = u \\
&\Lambda_4 = u + a \\
&\Lambda_5 = u - a
\end{aligned}
\tag{2.45}
$$

we have that the local solution is determined by the superposition of three waves with propagation velocity u and two waves with propagation velocity $u \pm a$ respectively.

Let's consider a generic calculation domain Ω, and try to determine what kind of boundary condition is necessary in position P on the border $\partial\Omega$. Let's choose a local coordinate system x,y with the x axis parallel and opposed to the unit vector **n** orthogonal and external to the border. Assuming the flow locally one-dimensional the solution on the border is given by the combination of the waves defined above. If the sign of the propagation velocity of a wave is such as to bring information from the outside of the domain to the inside, the information must be provided imposing appropriate boundary conditions. Conversely, if the propagation velocity of a wave has the same direction of the unit vector **n** (negative propagation velocity), the wave transports information from the inside to the outside of the domain. Such information must be calculated from the solution inside Ω. There will be a set of possible combinations depending on the sign of the velocity orthogonal to the border and on the local Mach number, which determines the sign of Λ_4 and Λ_5. The same considerations are also valid in the general case of one-dimensional flow, with the difference that the 5 waves will be partially coupled [28].

2.2 Rarefied flows and Slip flow

In gas microfluidics, the main micro effect that results from shrinking down the devices size is *rarefaction*. In this case it is purely a scale effect.
Modeling gas microflows requires to take into account several characteristic length scales. At the molecular level, we consider the mean molecular diameter d, the mean molecular spacing δ, and the mean free path l. Gases that satisfy the condition:

$$\frac{d}{\delta} << 1 \tag{2.46}$$

are said to be *dilute gases*. Conversely, if the condition above is not verified, the gas is defined as a *dense gas*. The dilute gas approximation leads to the classic kinetic theory and the Boltzmann transport equation.
For a simple gas, composed of identical molecules considered as hard spheres, at thermodynamic equilibrium the mean free path

$$l = \frac{1}{\sqrt{2}\pi d^2 n} \tag{2.47}$$

depends on the diameter d and the number density $n = \delta^{-3}$ [29].

The continuum assumption erases the molecular discontinuities by averaging the microscopic quantities on a small sampling volume. Such approach requires the sampling volume to be in thermodynamic equilibrium. Consequently, the characteristic times of the flow must be large compared with the characteristic time

$$\tau = \frac{l}{c} \tag{2.48}$$

of intermolecular collisions, defined by the meansquare molecular speed

$$c = \sqrt{3rT} \tag{2.49}$$

where r is the specific gas constant $r=R/M$ and T is the absolute temperature. The number of collisions inside the sampling volume must be high enough to respect thermodynamic equilibrium. This implies that the mean free path must be small compared to the characteristic length L of the sampling volume studied. As a consequence, the thermodynamic equilibrium requires that the Knudsen number Kn, which characterizes the rarefaction of the flow, satisfies:

$$Kn = \frac{l}{L} << 1 \tag{2.50}$$

The Knudsen number is defined as the ratio between the mean free path l and the characteristic length L of the flow examined. It is also related to the Reynolds number Re and the Mach number Ma, by the following expression:

$$Kn = \sqrt{\frac{\gamma\pi}{2}}\frac{Ma}{\mathrm{Re}} \tag{2.50}$$

The last relation is very important because it shows the connection between rarefaction and compressibility effects, the latter having to be taken into account when Ma is greater than 0.2.

2.2.1 Flow regimes classification

Although the Knudsen number is not the only parameter to take into account to describe the similitude between low pressure and confined flows, it results convenient to classify the flow regimes as a function of *Kn* [29]. Such classification, completed with empiricism, is usually accepted and is summarized by the following:

1) *Continuum flow*: for $Kn < 10^{-3}$
   It is accurately modeled by the Navier-Stokes equations with classical no-slip boundary conditions;

2) *Slip flow*: for $10^{-3} < Kn < 10^{-1}$
   The Navier-Stokes equations remain applicable, provided that a velocity slip and a temperature jump are taken into account at the walls;

3) *Transition* regime: for $10^{-1} < Kn < 10$
   The continuum approach of the Navier-Stokes equations is no longer valid. However, the intermolecular collisions are not yet negligible and should be taken into account;

4) *Free molecular* regime: for $Kn > 10$
   The occurrence of intermolecular collisions is negligible compared with the one of collisions between the gas molecules and the walls.

The limits of these different regimes are only indicative and could vary from one case to the other, partly because the characteristic length *L* is rarely unique.

For complex geometrical configurations, it is generally preferable to define *L* from local gradients rather than from simple geometrical considerations [30]. The Knudsen number based on this characteristic length is called the *rarefaction number* [31].

The relationship with the characteristic length L , expressed in μm, is illustrated in figure 2.1, which shows the typical ranges covered by fluidic microsystems presented in literature.

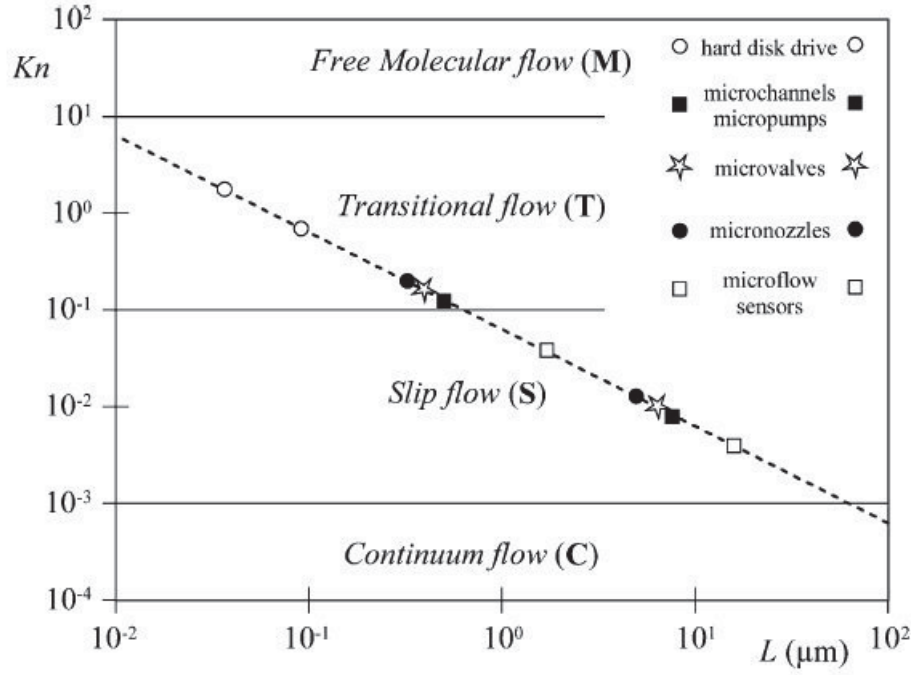

Figure 2.1: Characteristic lengths of typical fluidic microsystems, with the range of Knudsen numbers corresponding to standard conditions [32].

Typically, most of the microsystems which use gases work in the slip flow regime, or in the early transition regime.

2.2.2 Slip flow regime

Due to its great occurrence in gas microsystems, the slip flow regime has been widely studied, since it leads to quite simple models, yet good enough for the optimization of these microsystems for engineering applications.

In solving the Navier Stokes equations at macro scale, the typical boundary condition imposed on the tangential velocity at a solid surface is that of no-slip. Such assumption is essentially an empiric observation and, physically, it is due to the high number of collisions between the wall bound molecules and re-emitted ones.

However, it is known that, for gaseous flows, there always exists a non-zero velocity near the wall called *slip velocity*, as the particle-wall collisions are more than the interparticle ones. Based on a momentum balance at the wall, it can be shown that this *slip velocity* is a function of the velocity gradient near the wall itself.

The first boundary condition, which expresses the slip velocity at the wall, was proposed by Maxwell [33] and has the following form (non-dimensional):

$$u_t - u_w = \frac{2-\sigma}{\sigma} Kn \frac{\partial u_t}{\partial n} + \frac{3}{2\pi} \frac{\gamma-1}{\gamma} \frac{Kn^2 \,\mathrm{Re}}{Eck} \frac{\partial T}{\partial t} \tag{2.51}$$

In the slip regime, there is also another boundary condition to take into account, which expresses a *temperature jump*:

$$T_t - T_w = \frac{2-\sigma_T}{\sigma_T} \frac{3}{2\pi} \frac{2\gamma}{\gamma+1} \frac{Kn}{\mathrm{Pr}} \frac{\partial T}{\partial t} \tag{2.52}$$

The subscripts *w* relates to the wall and the subscripts *t* and *n* to the tangential and normal (exiting the wall) directions, respectively. At the contact point with the wall, the tangential velocity is denoted by u_t and the temperature as T_t. The specific heat ratio is denoted by γ. There are only three independent non-dimensional parameters: the Prandtl number *Pr*, the Reynolds number *Re* and the Knudsen number *Kn* which play a fundamental role if the flow is not isothermal.

The Eckert number *Eck* can be expressed as follows:

$$Eck = (\gamma - 1)\frac{T_0}{\Delta T} Ma^2 \tag{2.53}$$

The tangential momentum and thermal accommodation coefficients σ and σ_T, respectively, account for the interactions of the gaseous molecules with the wall. Their precise determination is problematic, because it depends on the nature of the gas and of the wall, as well as on the state of the surface. A purely specular reflection corresponds to σ=0 and a totally diffusive reflection corresponds to σ=1.

The second term in eq. (2.51) is responsible for the thermal creep effect (or thermal transpiration), which can cause a pressure variation and, as a consequence, a fluid motion contribution from cold to hot temperature, only in the presence of a wall tangential temperature gradient ($\partial T / \partial t = 0$). Assuming full accommodation, in fact, both hot and cold particles will be re-emitted with an average zero tangential velocity. Thus, hotter and faster molecules will lose more momentum than cooler, and thus slower ones. As a net result, the wall exerts a net force from the cold to the hot side.

The boundary conditions (2.51) and (2.52) are called first order boundary conditions; u_t and T_t are then proportional to the transverse velocity and temperature gradients, respectively, and to the *Kn*.

From a theoretical point of view, the slip flow regime is particularly interesting because in simple geometries it generally leads to analytical or semi-analytical models. Such models allow to calculate velocities and flow rates for isothermal and locally fully developed flows between plane plates or in cylindrical ducts with simple sections: circular, annular, rectangular, etc. [34,35,36].

In order to extend the validity of the slip flow regime to higher Knudsen values, many authors proposed second-order boundary conditions [32,37]. The second order terms may involve tangential second derivatives equal to zero ($\partial^2 u / \partial t^2 = 0$) [38].

For instance, in the simple case of a fully developed flow between plane plates, the tangential second derivatives are zero.

Most of the second-order models take the generic form:

$$u_t - u_w = A_1 Kn \frac{\partial u_t}{\partial n} + A_2 Kn^2 \frac{\partial^2 u_t}{\partial n^2} \tag{2.54}$$

Some second-order models are based on a simple mathematical extension of Maxwell's condition, and predict a decrease of the slip velocity compared to the first order model, while other models predict an increase. The latter, which are based on a physical approach of the behavior of the gas near the wall, follow the same trend of some experimental observations [39].

However, the Navier Stokes equations correspond to an approximation of the Boltzmann equation of the kinetic theory, which is first order in Knudsen, and should be associated with first-order boundary condition. [40]

In this thesis, the microflows studied lie in the slip flow regime characterized by Knudsen numbers that allow such flows to be satisfied by first-order boundary conditions.

2.3 Conjugate Heat Transfer

In convection through microchannels the heat conduction in the solid walls can become crucial. This happens because, due to manufacturing constraints, the solid wall thickness is at least comparable to the channel's diameter, or even larger. For microchannels, the ratio of wall thickness to channel diameter is usually much larger than that for macro scale tubes.

The solid heat conduction takes place mainly in the axial (i.e. parallel to the mainstream) direction, this is the reason why we will talk about *axial conduction*. The axial conduction effects are introduced due to the heat transfer in the fluid and in the wall in a direction opposite to the fluid flow. Furthermore, the importance of axial conduction increases with increasing ratio of channel thickness to channel length, and as the channel diameter decreases.

In this case, the temperature problem for the solid wall should be analyzed simultaneously with that for the fluid, in order to obtain the real heat flux distribution on the wall-fluid interface, and this coupled wall-fluid heat transfer is referred to as *Conjugate Heat Transfer (CHT).*

Many experimental studies reported in the literature for microchannels revealed a significantly lower value of fully developed Nusselt number for laminar flow with a further decreasing trend at lower Reynolds numbers.

The computational domain includes both the fluid and solid region: in the latter the velocities are set to zero and only the energy equation is solved.

In figure 2.2, the typical configuration of the heat fluxes involved on a micro channel wall is shown. When we have to do with conjugate heat transfer, two important heat fluxes have to be taken into account; these are the convective flux q''_{conv} between solid and fluid and the, already mentioned above, axial conduction flux q''_{cond}.

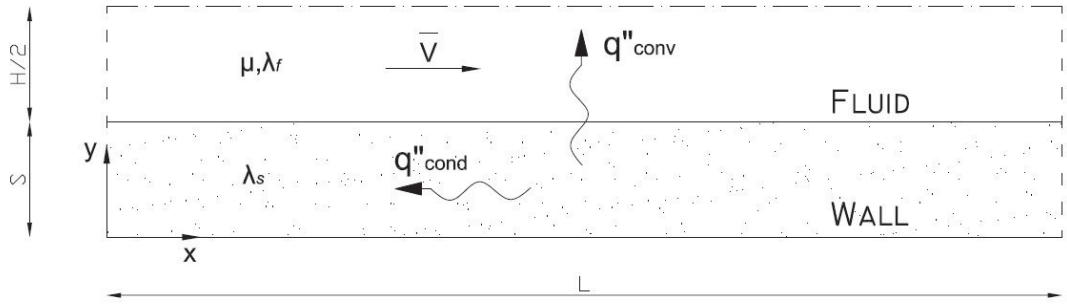

Figure 2.2: Microchannel wall and heat fluxes involved.

The expression for the two fluxes are:

$$q''_{conv} = \rho c_p H \bar{u} (T_{b,x=0} - T_{b,x=L}) \tag{2.55}$$

for the convection flux and

$$q''_{cond} = \frac{\lambda_s s}{L} (T_{b,x=0} - T_{b,x=L}) \tag{2.56}$$

for the conductive one, where $T_{b,x=0}$ is the fluid bulk temperature at the channel's inlet and $T_{b,x=L}$ is the fluid bulk temperature at the channel's outlet.

Maranzana defined an axial number M [20], which relates the axial wall conduction and convective heat flux:

$$M = \frac{q''_{cond}}{q''_{conv}} = \frac{1}{\mathrm{Re}} \frac{1}{\mathrm{Pr}} \frac{\lambda_s}{\lambda_f} \frac{s}{L} \tag{2.56}$$

Such parameter depends, as noticeable, on the geometrical configuration of the channel, the type of fluid, the flow's characteristic, and finally on the ratio between the solid and fluid thermal conductivities. The last plays a fundamental role in the

studies carried out, because it defines the influence of CHT, especially in the study of *Micro Heat Exchangers*.

Solid conductivity is chosen in order to balance axial conduction damage and the need for low normal thermal resistance.

The following figure 2.3 shows an example of the axial conduction influence on the temperature profiles of the flow and solid in a 2D microchannel. Without CHT the temperature profile is linear, but when the axial conduction effect gets relevant, the temperature distribution on the wall changes affecting the overall temperature field and yielding different profiles.

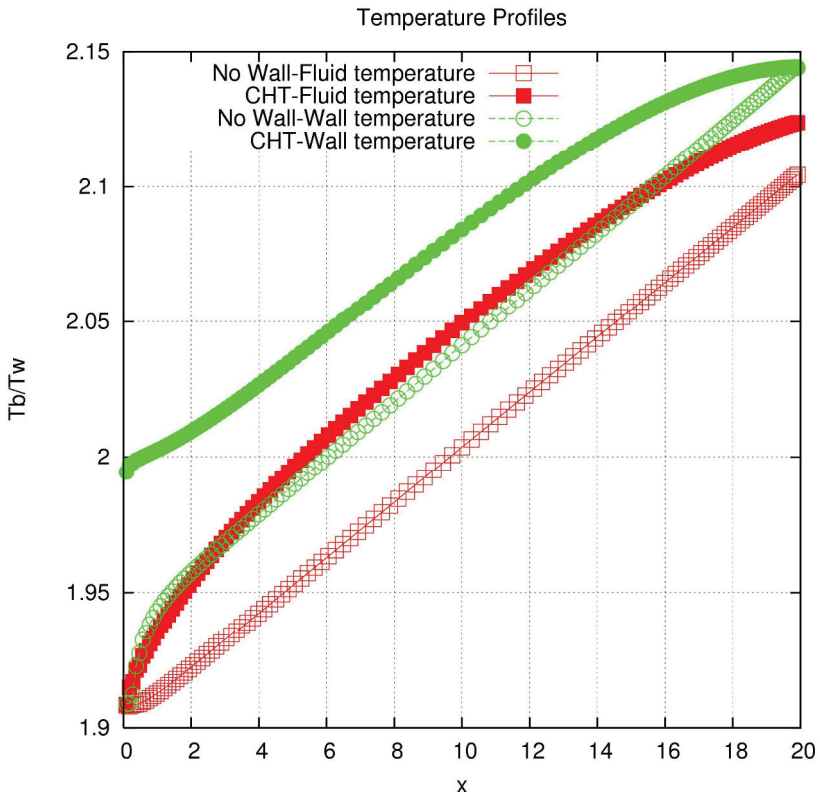

Figure 2.3: Comparison between fluid bulk temperature and wall temperature in a micro channel with and without the presence of the axial conduction (CHT). *L/H=20,* pressure ratio 2.5 [50].

CHAPTER 3 : NUMERICAL MODELS

In this chapter, a description of the models used is presented, in the first place describing the numerical method focusing on the CHT aspects, giving special attention to the interface treatment, which is the most difficult aspect to model in this problem. Then, we will concentrate on the boundary conditions and the physics of the problems. Finally, we will focus on the cases studied, illustrating the geometrical configuration, the material properties and the discretization of the domain. The parameters used in the simulations are also shown, followed by a description of which macro parameters they refer to.

3.1 Numerical Method and Navier-Stokes solver

This chapter exposes the numerical features and methods adopted to analyze the *Conjugate Heat Transfer* in the *Heat Sink* and *Micro Heat Exchanger*.

3.1.1 Governing equations and boundary conditions

The standard approach used to describe the gas flow is based on continuum Navier-Stokes equations. These equations describe the flow in terms of mere average flow velocity, gas density and temperature, thus are much more efficient than kinetic equations, but much less accurate in critical rarefied areas. The inaccuracy of NS equations in the boundary layer can be partially overcome by introducing slip boundary and temperature jump conditions on the solid surface. However, as indicated in the literature, slip conditions are valid only for the local Knudsen number $Kn \leq 0.1$, and any attempts to increase their range, resorting to higher order slip boundary conditions, is not trivial and highly geometrical dependent.

The governing equations of the flow are viscous, compressible two-dimensional NS equations which can be written in terms of conservative variables as:

$$\frac{\partial q}{\partial \vartheta} + \frac{\partial F(q)}{\partial \mathbf{x}} = 0 \tag{3.1}$$

$$q = \left(\rho, \rho\vec{w}, \rho e_{tot}\right), \qquad e_{tot} = e + w^2 / 2 \tag{3.2}$$

where e_{tot} is the total energy per unit mass.

The flux vector $F(q)$ may be decomposed into the convective (inviscid) and diffusive (viscous) components as in chapter 2:

$$F = F - F_v \tag{3.3}$$

$$F = \left(\rho\vec{w}, \rho\vec{w}\vec{w} + pI, \vec{w}\rho h_0\right)^T \tag{3.4}$$

$$F_v = \left(0, f, f \cdot \vec{w} + \lambda\nabla T\right)^T \tag{3.5}$$

As in any compressible flow solver, viscous dissipation term $f \cdot \vec{w}$ is included in the energy equation. Pressure p and total energy per unit mass e_{tot} are linked by the equation of state for ideal gas:

$$p = \rho\left(\gamma\text{-}1\right)\left(e_{tot} - \frac{\vec{w}^2}{2}\right) \tag{3.6}$$

The inlet/outlet boundary conditions are standard and specify the inlet total temperature T^0, total pressure p^0 and flow direction, and the static pressure p_e at the outlet. The compressibility effect of the gas is monitored via the local value of Mach number Ma and the isentropic exit Mach number Ma_{is} (i.e., Ma that would arise from an isentropic flow with the same pressure ratio as the real one):

$$\frac{p^0}{p_e} = \left(1 + \frac{\gamma - 1}{2} Ma_{is}^2\right)^{\gamma/(\gamma-1)} \tag{3.7}$$

$$\frac{T^0}{T_e} = \left(1 + \frac{\gamma - 1}{2} Ma_{is}^2\right) \tag{3.8}$$

$$\rho^0 = p^0 / RT^0 \tag{3.9}$$

At the solid wall the Maxwell first order slip boundary condition is imposed [24, 41]:

$$u_t - u_w = s_p Kn \left(\frac{\partial u_t}{\partial \mathbf{n}} + \frac{\partial u_n}{\partial \mathbf{t}}\right) \tag{3.10}$$

$$s_p = \frac{\sqrt{\pi}}{2} \frac{2 - \sigma_v}{\sigma_v} \left(1 + 0.1366 \sigma_v\right) \tag{3.11}$$

where **n** and **t** are unit vectors normal and tangential to the solid wall, respectively. In computations s_p is around one (i.e., the fraction σ_v of incident particles scattered diffusely is set equal to one). The additional derivative along the tangential direction is essential in capturing even the qualitative behaviour of the slip flow along curved walls.

A Dirichlet temperature boundary condition is imposed at the wall. The wall temperature is fixed at the inlet total temperature value to minimize the effect of viscous dissipation. In the energy equation, the Smoluchowski temperature jump is used:

$$T_t - T_w = s_T Kn \frac{\partial T}{\partial \mathbf{n}} \tag{3.12}$$

$$s_T = \frac{2 - \sigma_T}{\sigma_T} \frac{2\gamma}{\gamma + 1} \frac{1}{\mathrm{Pr}} \tag{3.13}$$

where s_T is the temperature jump coefficient. Since the flow is considered isothermal the temperature accommodation coefficient σ_T equals to one. At the symmetry line the specular boundary condition is imposed.

The non-dimensionalization introduced in the models is reported in **Appendix A**.

3.1.2 Numerical scheme

Navier-Stokes equations are solved by employing a finite difference and finite volume method. The numerical method is described in detail in [42] and has formal second order accuracy in space and time. Thus, here it is only briefly outlined.

Adopting a curvilinear structured mesh, we may define a computational cell of volume Λ_{ij} with faces A_k, $k = 1,\ldots, 4$ around each node. At each of these computational cells the flux balance offers:

$$\Lambda_{ij} \frac{\partial q_{ij}}{\partial \vartheta} = \sum_{k=1}^{4} F(q) \cdot A_k \mathbf{n}_k \tag{3.14}$$

Fluxes are defined via neighbouring value averaging, and an artificial dissipation term d is added to prevent checker boarding and numerical instabilities. Thus, considering a face located at i+1/2 we get:

$$F(q)_{i+1/2} = \frac{F(q)_i + F(q)_i}{2} + d_{i+1/2} \tag{3.15}$$

Artificial dissipation term d are given by a blend of second and fourth order differences, scaled by the maximum eigenvalue of jacobian matrix of vectors F, as suggested in (Pulliam [43]). Second order terms are switched on near discontinuities, as in Pulliam [43]. Viscous flux vectors are evaluated with second order finite differences at i+1/2. The solution is advanced in time via Crank Nicolson integration scheme, and the resulting matrices are decomposed via the spatially factored ADI scheme originally proposed by Beam and Warming (see Hirsh [44]). Following such scheme, two series of block tridiagonal algebraic systems are solved at each time step, rather than the original sparse matrix arising from the flux discretization.

3.1.3 Conjugate Heat Transfer: numerical details on fluid/solid interface treatment

Several approaches may be adopted in order to deal with the fluid/solid interface in a conjugate heat transfer problem. Often, especially in industrial environment, different codes may be used for each domain, and a specific coupling procedure has to be designed in order to enforce heat flux and temperature continuity at the interface. An example may be found in [45].

Here, the simple geometry suggests to solve also the wall conduction problem within the same Navier-Stokes solver used for the fluid domain, simply imposing zero velocities in the solid domain. The different thermal capacities would lead to quite different time scales in the fluid and solid: since we are only concerned with the steady state behavior of the flow, we artificially reduce the solid thermal capacity to the same value as the fluid, to reduce the 'physical' time to convergence.
With a similar approach the interface is just an internal node, and in principle it should not need any special treatment. Some attention has to be given only to pressure discretization: since we explicitly impose zero velocities (rather than trying to force it via an infinite viscosity, as sometime proposed in literature), and obviously we neglect solid elasticity, the pressure has no meaning inside the solid. Thus, the pressure derivative at the interface has to be defined with a one-sided stencil, including only interface and fluid nodes. The same one-sided differencing is required for the temperature, since the strong difference in conductivity and the heat flux continuity yields a change in the temperature slope at the interface, where we have a singular point in first derivatives.

However, in presence of slip flow and temperature jump, this interface is no longer a standard node by any means. In particular, we would have two different values on the same node for both temperature and velocities. Again, this requires one-sided finite difference stencils to evaluate both temperature gradients (on both solid and fluid side) and velocity gradients (only on the fluid side). Furthermore, the problem closure is given by slip and temperature jump equations (2.51-2.52):

$$u_t - u_w = \frac{2-\sigma}{\sigma} Kn \left(\frac{\partial u_t}{\partial \mathbf{n}} + \frac{\partial u_n}{\partial \mathbf{t}} \right) + \frac{3}{2\pi} \frac{\gamma - 1}{\gamma} \frac{Kn^2 \,\mathrm{Re}}{Eck} \frac{\partial T}{\partial \mathbf{t}} \tag{2.51}$$

$$T_t - T_w = \frac{2-\sigma_T}{\sigma_T} \frac{3}{2\pi} \frac{2\gamma}{\gamma+1} \frac{Kn}{\mathrm{Pr}} \frac{\partial T}{\partial \mathbf{t}} \tag{2.52}$$

The present code handles the boundary conditions in a semi-explicit way: the system of equations for the inner nodes is solved assuming Δq=0 at the boundaries (i.e., as if the boundary solution were already converged), and the boundary values are then updated using the updated inner values at time step n+1. Accordingly, we solve the inner equations assuming slip velocity and temperature jump from the previous time step *n*, and then we update them explicitly using equations (2.51-2.52) and imposing zero normal pressure gradient on the fluid side, using the inner values at *n*+1.

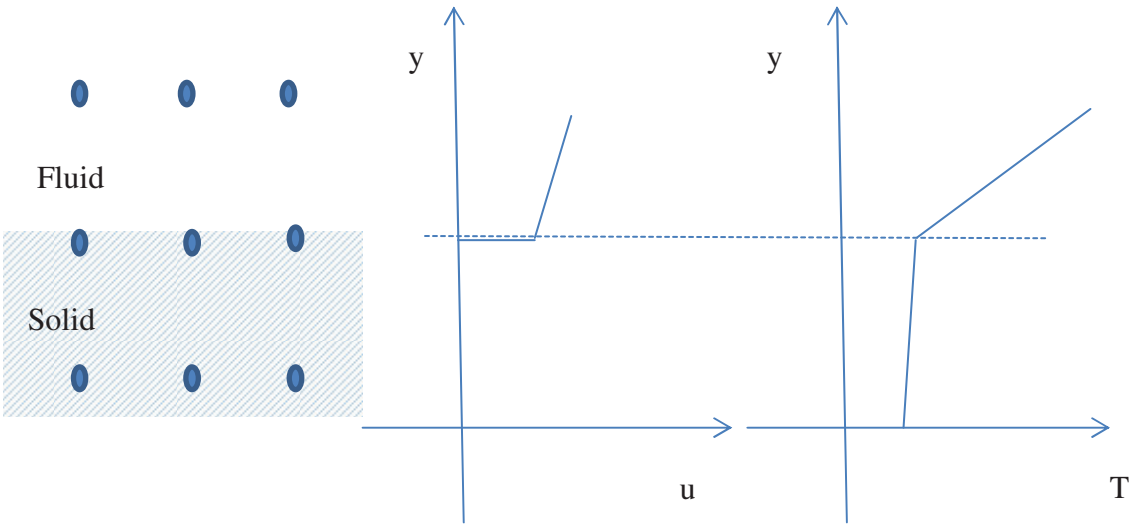

Fig. 3.1: Interface nodes, slip velocity and temperature jump.

It is important to remark that the node on the fluid side of the interface is a standard internal node: thus, in the computation of the face viscous fluxes, it takes automatically into account the product of shear stress and local (slip) velocity.
In other words, the shear work at the interface is correctly considered in the global balance.

3.2 Heat sink model

The viscous, compressible NS equations for 2D laminar flow are solved by employing the hybrid finite difference-finite volume method previously described. The code, also described in [42], which follows standard numerical techniques, has already been applied and validated for the simulations of micro-flows [46]. Here, it is used in conjugate heat transfer (CHT) mode: the computational domain includes both the fluid and solid region, although in the latter velocities are set to zero and only the energy equation is solved.

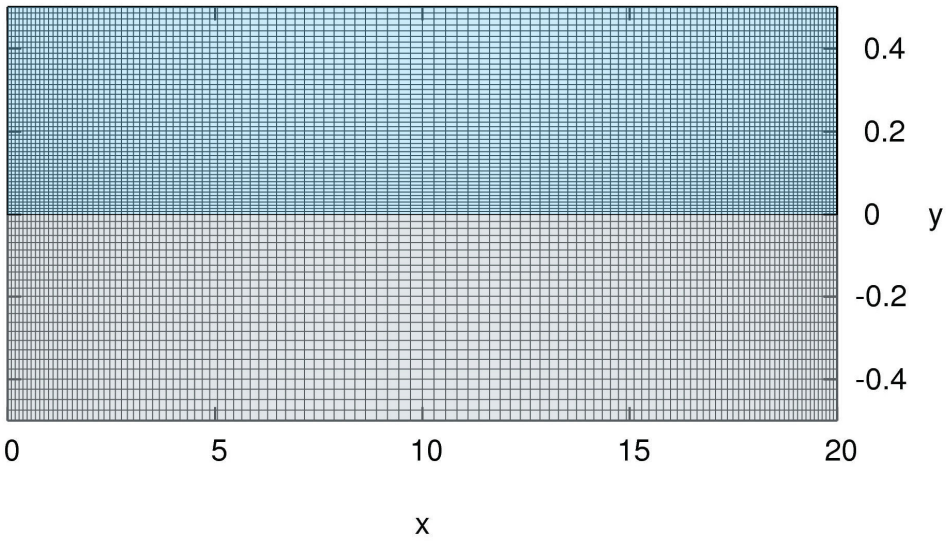

Fig. 3.2: Sketch of the computational domain: in blue the fluid and in grey the solid. In this case L=20, with i=120 nodes along x and j=72 nodes along y.

A plane channel of length L and height H is considered, with a solid of thickness s, as in the sketch in Fig.3.2. Normally, in the CHT simulations, the size of the mesh is 120x72 nodes, with i=120 nodes along the x direction and j=72 nodes in the y one. On the y axis 25 nodes belong to the solid and the remaining 47 to the fluid.

The node density has been concentrated in the fluid domain near the wall due to the presence of high gradients of the velocity field (boundary layer). It has also been concentrated at the inlet and the outlet of the channel where quantities are subjected to stronger derivatives and oscillations. (Fig.3.3)

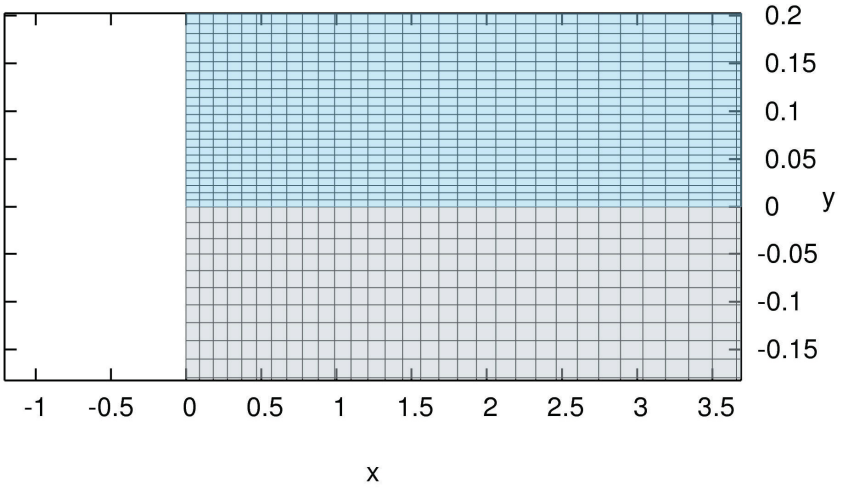

Fig. 3.3: Zoom of the computation grid on the solid/fluid interface at the inlet.

Due to the symmetry, only one half of the physical domain is considered, including the bottom wall of thickness s ($-s < y < 0;\ 0 < x < L$) and the lower half ($0< y <H/2$) of the channel. At the flow inlet we impose stagnation pressure p_0 and temperature T_0 and the flow direction, assumed normal to the boundary, while static pressure p_e is imposed at the outlet. Symmetry is applied to the flow at $y = H/2$.
A constant property gas, with $\gamma=1.4$ and $Pr=0,7$, is considered.

In the solid domain, a fixed flux heat transfer boundary condition is imposed on the lower side ($y = -s$), while the vertical faces at $x = 0$ and $x = L$ are assumed adiabatic. Thermophysical properties, such as viscosity μ and fluid and solid thermal conductivity λ_f and λ_s, are kept constant.

The fluid-solid interface, even if it is only an internal boundary, needs special treatment due to the rarefaction effect. In particular, the Maxwell first order slip boundary condition is here used:

$$u_f - u_w = s_p l\left(\frac{\partial u}{\partial y} + \frac{\partial v}{\partial x}\right) + \frac{3}{4}\frac{\mu}{\rho T}\frac{\partial T}{\partial x} \tag{3.15}$$

with

$$s_p = \frac{\sqrt{\pi}}{2}\frac{2-\sigma_v}{\sigma_v}(1+0.1366\sigma_v) \tag{3.16}$$

Although equation (3.15) includes, for the sake of completeness, the thermal creep term (the one with $\partial T / \partial x$), in the configuration considered its effect results nearly negligible.

In the computations the accommodation coefficient σ_v is set equal to one (i.e., diffuse scattering of wall incident particles). The additional velocity derivative along the tangential direction x in eq.(3.15), although essential in capturing the behaviour of slip flow along curved walls, vanishes for straight walls, as in the present case.

Fluid and solid side temperature on interface differ, due to Smoluchowski temperature jump:

$$T_b - T_w = s_T l\frac{\partial T}{\partial y} \tag{3.17}$$

with

$$s_T = \frac{2-\sigma_T}{\sigma_T}\frac{2\gamma}{\gamma+1}\frac{1}{\mathrm{Pr}} \tag{3.18}$$

where s_T is the temperature jump coefficient. We assume the temperature accommodation coefficient σ_T equal to one.

Viscous effect magnitude is measured via Reynolds number, defined as:

$$\mathrm{Re} = \frac{\vec{\rho}\bar{u}H}{\mu} = \frac{\dot{m}'}{\mu} \tag{3.19}$$

where $\dot{m}'$ is mass flow per unit depth, ρ the density and $\bar{u}$ the average streamwise velocity. Furthermore, if l is the molecule mean free path, we can define, as a measure of rarefaction relevance, a Knudsen number in terms of local (section averaged) values:

$$Kn = \frac{l}{H} = \frac{16}{5}\sqrt{\frac{\gamma}{2\pi}}\frac{Ma}{\mathrm{Re}} \tag{3.20}$$

Finally, a relevant parameter is the axial conduction number M, defined by Maranzana et al [5] as the ratio between a representative conductive axial heat flux:

$$q'_{cond} = \frac{\lambda_s s}{L}(T_{b,x=0} - T_{b,x=L}) \tag{3.21}$$

where the subscript b refers to the bulk temperature, i.e. a mass flow average through the cross section at a given x, and the total convective flux:

$$q'_{cond} = \rho c_p H\bar{u}(T_{b,x=0} - T_{b,x=L}) \tag{3.22}$$

$$M = \frac{q'_{cond}}{q'_{conv}} = \frac{1}{\mathrm{Re}}\frac{1}{\mathrm{Pr}}\frac{\lambda_s}{\lambda_f}\frac{s}{L} \tag{3.23}$$

Eq.(3.23) demonstrates why the flow in short channel at microscale may depart from standard macro scale behaviour: for a fixed channel geometry and material, in order to reduce the axial conjugate heat transfer effect (i.e. keeping M low) a higher Re is required; however, this means increasing the velocities, the Mach number and thus

the compressibility effect. Thus, in most cases either relevant compressibility or relevant conjugate heat transfer will be found. Furthermore, since L appears in the denominator, short channel will emphasize the CHT.

Here, an aspect ratio L/H of 20 is chosen, with a relatively thick wall, so that $s/H = 1$. Several computations were carried out, in order to explore a broad range of conditions. All the parameters are set in non dimensional terms: however, in order to give a little practical perspective, it could be representative of a channel of 10μm in height, subjected to heat flux from 10 to 200 kW/m^2. Such heat fluxes are representative of relatively standard conditions, suitable for single phase heat removal, quite lower than high heat flux conditions, assumed from 1000 kW/m^2 [46].

Further details on the cases analysed and on the parameters used are presented in the next chapter.

3.3 Micro Heat Exchanger model

An array of identical plane channels of height H and length L is considered, alternating hot and cold gas flows in each of them: the elementary periodic cell is reduced to one half of two adjacent channels and the solid wall of thickness s between them.

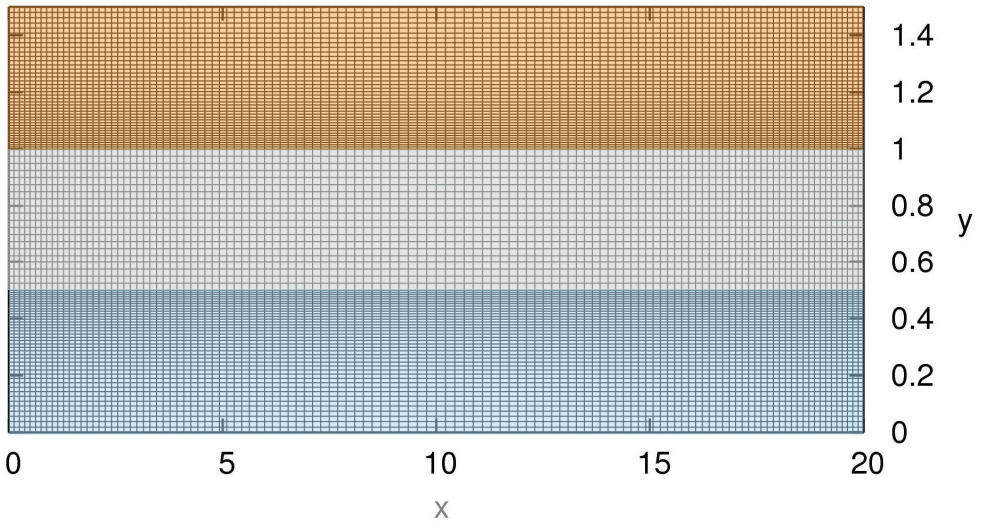

Fig. 3.4: Sketch of the computational domain for the Micro Hheat Exchanger: in orange the hot fluid, in blue the cold fluid and in grey the solid. In this case L=20 with i=120 nodes along x and j=101 nodes along y.

Thus, the computational domain covers the area defined by $0<x< L$ and $0<y< H+s$, as shown in Figure 3.4.

For the mesh used in the simulations, the size of the grid is 120x101 nodes, with i=120 nodes along the x direction and j=101 nodes in the y one. On the y axis 19 nodes belong to the solid domain, one to each fluid/solid interface and 40 to both hot and cold fluid domains.

As for the heat sink, the node density has been concentrated in the fluid domain near the solid/fluid interfaces due to the presence of high gradients of the velocity field (boundary layer). It has also been concentrated at the inlet and the outlet of the channels where quantities are subjected to stronger derivatives and oscillations.

The figure below shows in detail the node density on the internal boundaries and at the inlet and outlet of the channels.

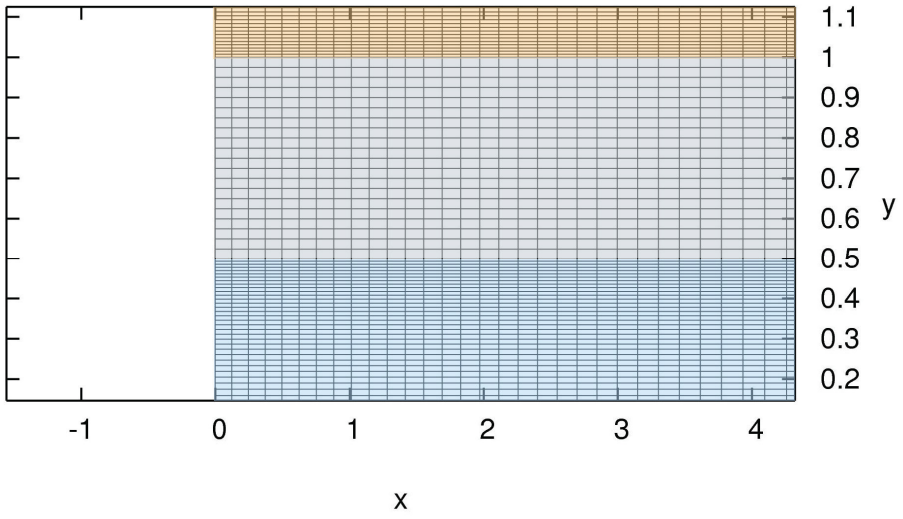

Fig. 3.5: A detailed view of computation grid on the solid/fluid interfaces.

Following standard definitions for compressible flows, we introduce the stagnation state, defined by the pressure p^0 and temperature T^0 that the flow would attain after an adiabatic, isentropic arrest. The two are related via the local Mach number:

$$T^0 = T\left(1+\frac{\gamma-1}{2}Ma^2\right) \tag{3.24}$$

$$p^0 = p\left(1+\frac{\gamma-1}{2}Ma^2\right)^{\frac{\gamma}{\gamma-1}} \tag{3.25}$$

The stagnation temperature gives a measure of the total energy content of the flow, and is thus usually more suited to energy balance considerations; in particular, the stagnation temperature is the temperature that could be measured in the inlet and exit plenums. At the flow inlets we impose stagnation pressure p_i^0 , stagnation temperature T_i^0 and the flow direction, assumed normal to the boundary, while static pressure p_e is imposed at the outlet (usually set equal to the atmospheric pressure). Symmetry is applied at the channels midlines ($y=0$, $y=s+H$). The solid wall vertical faces at $x=0$ and $x=L$ are assumed adiabatic.

The same gas, characterized by a specific heat ratio γ=1.4 flows on the hot and cold sides, and for both channels we keep the same ratio β between inlet stagnation pressure and exit static pressure.

Thermophysical properties, such as viscosity μ and fluid and solid thermal conductivity λ_f and λ_s, are kept constant.

The fluid-solid interface, even if it is only an internal boundary, needs special treatment due to the rarefaction effects. In particular, the Maxwell first order slip boundary condition (3.15)-(3.16) is here used. In the computations the accommodation coefficient σ_v is set equal to one (i.e., diffuse scattering of wall incident particles).

The additional derivative along the tangential direction x in eq.(3.15), although essential in capturing the behavior of slip flow along curved walls, vanishes for straight walls, as in this case as well.

Fluid and solid side temperature on interface differ, due to the Smoluchowski temperature jump condition (3.17)-(3.18). We assume the temperature accommodation coefficient σ_T equal to one. Viscous effect magnitude is measured via Reynolds number, as defined for the heat sink (3.19).

Different aspect ratios *L/H* ranging from 20 to 100 are considered, with a relatively thick wall, so that *s/H*=0.5. Several computations were carried out, in order to explore a broad range of conditions (further details in the next chapter). Since we are dealing with compressible flows temperature and velocity fields are coupled: thus, the heat exchanger performances will also be a function of the operating temperatures.

All the parameters are set in non-dimensional terms. In particular, any single run condition is defined by the pressure ratio $\beta = p_i^0 / p_e$, which is chosen equal for hot and cold side, by the fluid/solid conductivity ratio $\Lambda = \lambda_f / \lambda_s$, by the length of the channel *L* (normalized over channel height *H*) and by representative temperature ratio:

$$\tau = \frac{T_i^h - T_i^c}{T_i^c} \tag{3.26}$$

However, in order to give a little practical perspective, the condition here considered could be representative of a channel of 10μm of height, atmospheric pressure at the outlets and a cold side inlet temperature of 283 K.

CHAPTER 4 : RESULTS AND DISCUSSION

In the present chapter the results obtained from the simulations are exposed and discussed. At the beginning, the cases investigated are described illustrating the parameters chosen and the range of operation.

For the heat sink the results are always compared with an analogous case without solid wall (no CHT). Thereby it is possible to highlight the axial conduction influence on the heat transfer.

For the Micro Heat Exchanger the main task is to evaluate the effectiveness in terms of the Maranzana number, which takes into account the Conjugate Heat Transfer effects, and of different flow configurations. Most of the simulation are performed for short channels where it is rather easy to emphasize compressibility effects.

At the end a correlation for the local Stagnation Nusselt number is derived.

4.1 Heat Sink

As already described in the previous chapters, in micro flows rarefaction effects appear due to the small dimensions involved; the microchannel flows in the cases presented fall into the Slip Flow Regime, which in terms of Knudsen number ranges between $0.001 < Kn < 0.1$.

It is also important to remind that micro flows are characterized by very low Reynolds numbers, and that the pressure drops that are considered generate severe compressibility effects.

Conjugate Heat transfer plays the major role as the size of the hydraulic diameter of the channel is of the same order of the wall thickness.

Now that these conditions are pointed out the ranges of parameters considered can be illustrated.

Several simulations have been carried out using different Reynolds and Isentropic Mach number, which is related to the pressure drop, defined by the following:

$$\mathrm{Re} = \frac{\vec{\rho} u_{is} H}{\mu} \tag{4.1}$$

$$\frac{p_i^0}{p_e} = \left(1 + \frac{\gamma - 1}{2} Ma_{is}^2\right)^{\left(\frac{\gamma}{\gamma-1}\right)} \tag{4.2}$$

A plane short channel of length L and height H is considered, Fig.4.1. The fluid considered is air, which has a specific heat ratio γ= 1.4 and a Prandtl number Pr = 70.

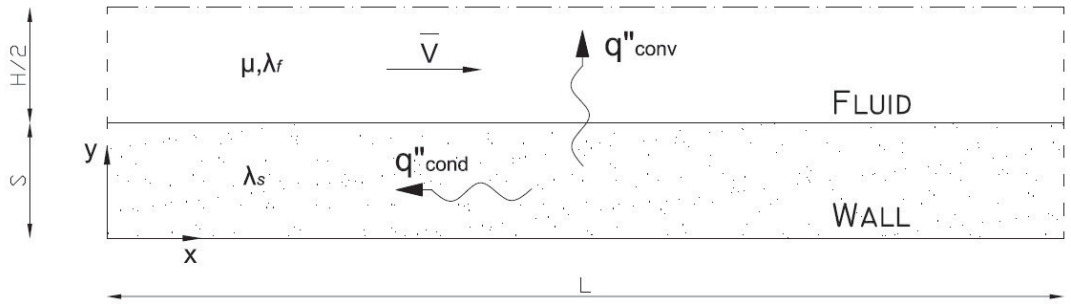

Fig. 4.1: Channel and heat transfer configuration.

The channel configuration is a so called *Heat Sink*, where the fluid removes a fixed heat flux generated below the wall.

The ranges of the parameters used, values that are defined and that characterize each case simulated, are listed below:

- Fluid: air (γ =1.4)
- Reynolds Number: 130 < Re < 280
- Pressure Ratio: 1.2 < β < 3.2
- Channel Height: H = 10 μm
- Channel Length: L = 20H, 40H
- Conductivity Ratio: λ_s/λ_f = 100

The conductivity ratio has been chosen specifically to obtain considerable Conjugate Heat Transfer effects. (Further investigations could yield the optimum value of such ratio).

The heat fluxes considered are the following:

- q'' = 20, 30, 50 , 100, 200 kW/m^2.

Table 4.1 summarizes the ranges of values of all the parameters involved and that characterize the flow under exam.

Parameter	Symbol [dim]	Min value	Max value
Reynolds Number	Re	130	280
Isentropic Mach Number	Ma_{is}	0.6	1.4
Pressure Ratio	β	1.2	3.2
Channel Height	$H\ [\mu m]$	10	
Channel Length	$L\ [H]$	20	40
Conductivity Ratio	λ_s/λ_f	100	
Specific heat Ratio	γ	1.4	
Heat Flux	$q''\ [kW/m^2]$	20	200
Axial Conduction Number	M	0	0.045
Exit Average Mach Number	Ma_e	0.14	0.84
Exit Knudsen number	Kn_e	0.007	0.01

Table 4.1: Main parameter ranges.

From the non-dimensionalization it is possible to show that the simulations are also valid for a channel 20mm long and 1mm high, working with a pressure drop of 2.5 with p_{atm} at the inlet and 40000 Pa at the outlet.

The following table shows all the parameters used in the computation for each simulation carried out.

Heat Sink cases analyzed, L=20H , H=10µm, $T_{0,in}$=300 K (CHT and No wall)				
N	$M_{a,is}$	β	Re_{is}	q'' [KW/m^2]
1	0.6	1.3	134	10
2	0.8	1.5	174	10
3	0.9	1.7	193	10
4	0.95	1.8	202	10
5	1.0	1.9	211	10
6	1.2	2.4	245	10
7	1.4	3.2	275	10
8	0.6	1.3	134	30
9	0.8	1.5	174	30
10	1.0	1.9	211	30
11	1.2	2.4	245	30
12	1.3	2.8	260	30
13	1.4	3.2	275	30
14	0.6	1.3	134	50
15	0.8	1.5	174	50
16	1.0	1.9	211	50
17	1.2	2.4	245	50
18	1.4	3.2	275	50
19	0.6	1.3	134	100
20	0.8	1.5	174	100
21	1.0	1.9	211	100
22	1.2	2.4	245	100
23	1.4	3.2	275	100
24	0.6	1.3	134	200
25	0.8	1.5	174	200
26	1.0	1.9	211	200
27	1.2	2.4	245	200
28	1.4	3.2	275	200

Table 4.2: Simulations and parameters chosen.

4.1.2 Heat transfer performances

The most common performance parameter for heat transfer in micro or macro channels is the *Nusselt Number*, related to the ratio between actual total heat transfer and the conductive one from the fluid to the solid; thus, if α is the local heat transfer coefficient we may define a *Local Nusselt* as:

$$Nu(x) = \frac{\alpha\, D_H}{\lambda_f} = 2\frac{\alpha\,(T_{w,x} - T_{b,x})}{\lambda_f / H \cdot (T_{w,x} - T_{b,x})} = 2\frac{q''}{q_c''} \tag{4.3}$$

and a *Global Nusselt*, averaged over the whole length of the channel:

$$Nu = \frac{1}{L}\int_L \frac{q''\, D_h}{\lambda_f\,(T_{w,x} - T_{b,x})}\, dx \tag{4.4}$$

Fig. 4.2 shows the Nusselt number computed in the standard way, eq.(4.3), vs. the exit Mach number, for different pressure ratios and different heat flux rates. Under all of the conditions Nusselt decreases if the pressure ratio (and, thus, the exit *Ma*) increases. Furthermore, we notice a remarkable influence of the heat flux. Such behavior is related to the very nature of compressible flows, where the temperature change is driven not only by the heat transfer, but also by the conversion between internal and kinetic energy. Thus, the flow acceleration induces bulk flow cooling, increasing the denominator of eq. (4.3) independently on the heat transfer.

As a consequence, Nusselt is lower than for standard laminar incompressible duct flow, and decreases with both an increase in *Ma* (as the acceleration effect increases) and a heat flux reduction (since this increases the relative importance of the acceleration effect).

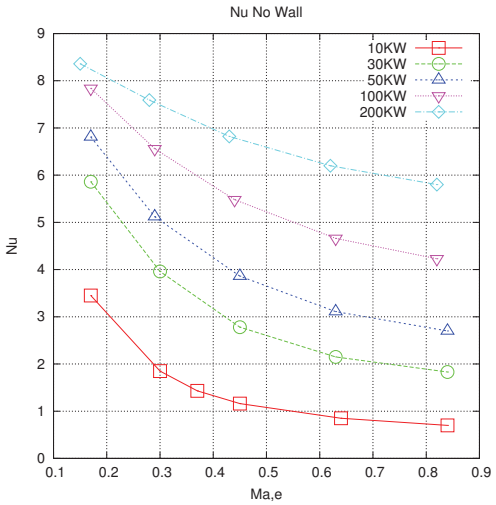

Figure 4.2a: Nusselt number, eq.(4.3), vs. exit Mach number Ma_e, neglecting wall conduction (NW).

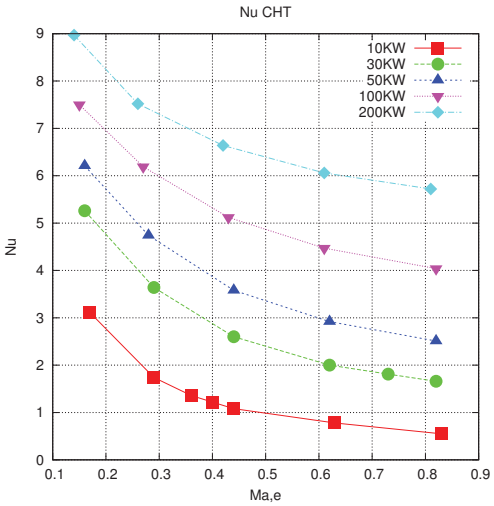

Figure 4.2b: Nusselt number, eq.(4.3), vs. exit Mach number Ma_e, full conjugate computation (CHT)

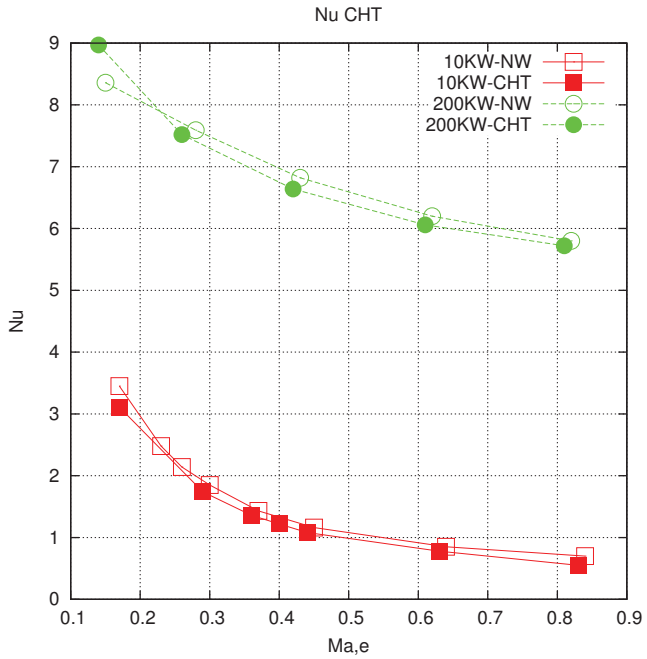

Figure 4.3: Nusselt number, eq.(4.3), vs. exit Mach number Ma_e, full conjugate computation (CHT) and neglecting wall conduction (NW).

However, this reduction in Nusselt number may be misleading: actually, in fact, the increase in Mach and the corresponding cooling means that the fluid is able to keep the wall at a lower temperature, i.e. its performance from an engineering point of view is enhanced. A possible alternative is to define the Nusselt number in term of total (or stagnation) temperature T^0:

$$T^0 = T + \frac{1}{2}\frac{u^2}{c_p} \tag{4.5}$$

In this case, any change in total bulk temperature is, actually, driven exclusively by the heat transfer. Unfortunately, on the other hand, the local heat transfer at the wall is induced by the local gradient in thermodynamic (or static) temperature T, rather than the total one. Therefore, we could have unbounded Nusselt numbers (it goes to infinity if the total bulk temperature is equal to the wall one, while the static one is lower and allows for finite heat transfer) and change of sign.

In the framework of heat removal applications, another popular parameter is the global device heat sink efficiency [47]:

$$\varepsilon = \frac{q'' D_h}{\lambda_f (\overline{T}_w - T^0_{b\,x=0})} \tag{4.6}$$

The parameter ε has an immediate engineering meaning, since it relates the heat flux that has to be removed to the difference between the inlet fluid bulk temperature (i.e. the main characteristic of the available cooling fluid) and the average wall temperature (i.e. the main parameter to be controlled, at least in the framework of electronic equipment) [48].

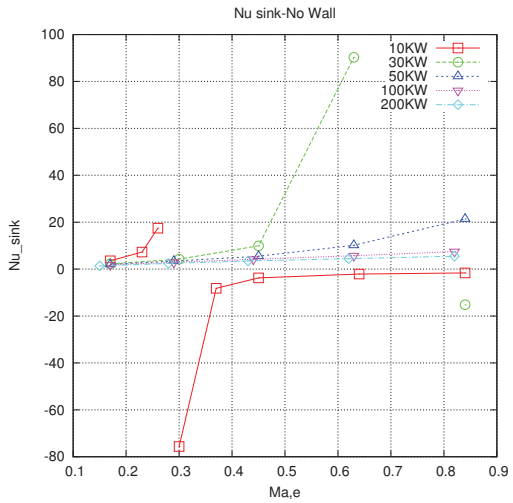

Figure 4.4a: Heat sink efficiency, eq.(4.6), neglecting wall conduction (NW).

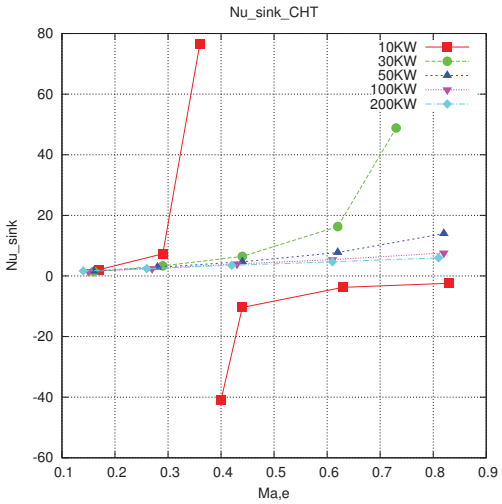

Figure 4.4b: Heat sink efficiency, eq.(4.6), full conjugate computation (CHT).

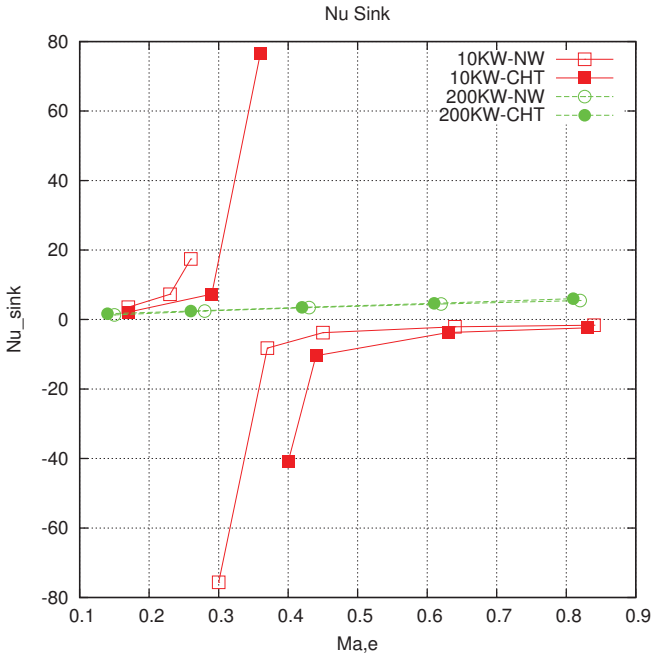

Figure 4.5: Heat sink efficiency, eq.(4.6), full conjugate computation (CHT) and neglecting wall conduction (NW).

In the case of compressible flow, the device designer knows the temperature at the inlet plenum, i.e. the inlet total temperature.

Nevertheless, some difficulties arise also in the evaluation of the heat sink efficiency ε: again, we find unbounded values and sign inversion.

This is related to the fluid cooling due to compressibility effect: in particular, if the pressure ratio and the geometrical configuration allows for high values of Mach number, the major contribution to the wall cooling is related to the fluid direct expansion, and the exit flow (at least at lower heat fluxes) may even be cooler than the inlet flow. This is clear from the comparison between Fig. 4.6 and Fig. 4.7. In Fig. 4.6 we plot the streamwise profile of bulk, total bulk and wall temperature for a low heat flux case (10kW) and a low exit *Ma* of 0.165, in Fig. 4.7, the same plot is reported for a higher exit Mach number equal to 0.4 (i.e., the lowest Mach corresponding, for the chosen heat flux, to a negative ε in Fig. 4.5).

The cooling effect due to the gas expansion mentioned above is a dynamic effect which is described by the Rayleigh flow [49], i.e. at high Mach numbers the conversion from thermal energy to kinetic energy is very strong such that the fluid bulk temperature decreases even if the fluid itself still receives heat from a source.

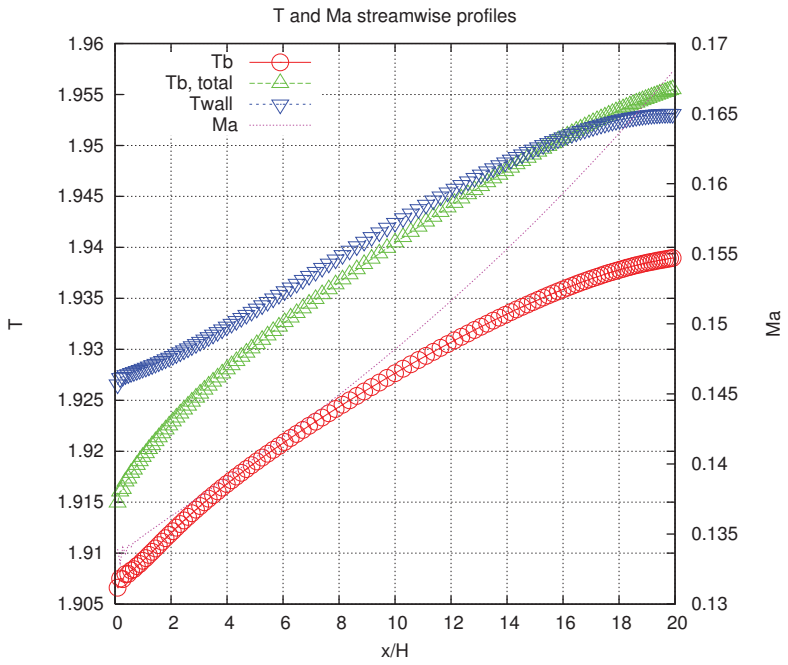

Figure 4.6: Temperature and Mach streamwise profiles, low flux $q'' = 10$, $Ma_e = 0.165$.

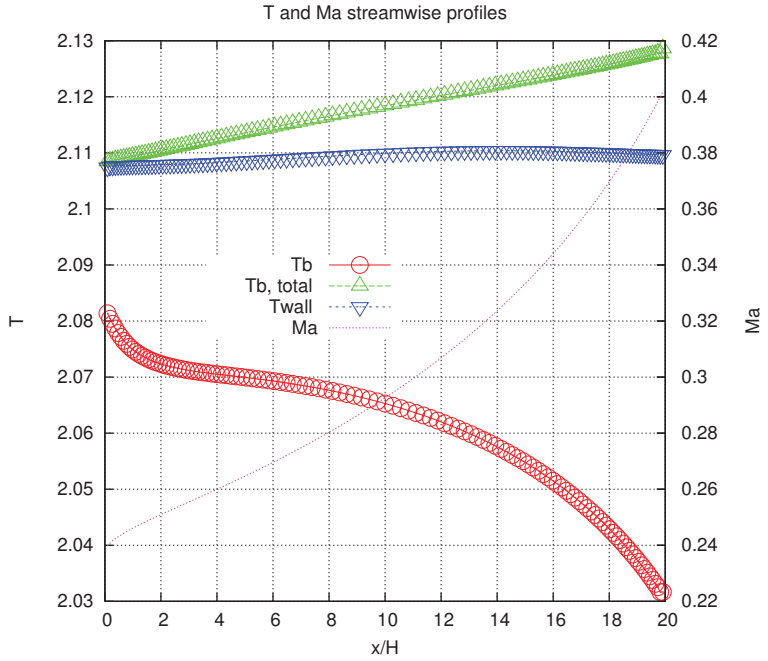

Figure 4.7: Temperature and Mach streamwise profiles, low flux $q'' = 10$, $Ma_e = 0.4$.

In Fig.4.6 temperatures follow the more intuitive pattern, and in particular the wall is warmer than the fluid for most of the channel length, so that it is visually clear that the average wall temperature is higher than both the static and total inlet ones. On the other hand, increasing the Mach number, in Fig.4.7 it is clear that the wall is actually colder than the fluid in the plenum (i.e., wall temperature lower than inlet total one). Thus, the heat sink efficiency at Ma_e=0.4 is negative, and there will be an infinite value somewhere between the condition Ma_e=0.165 and Ma_e=0.4, (vertical asymptote in Fig. 4.5), where the average wall temperature equates the inlet plenum one. Fig.4.8 shows the wall temperature distribution in the case where the asymptote appears.

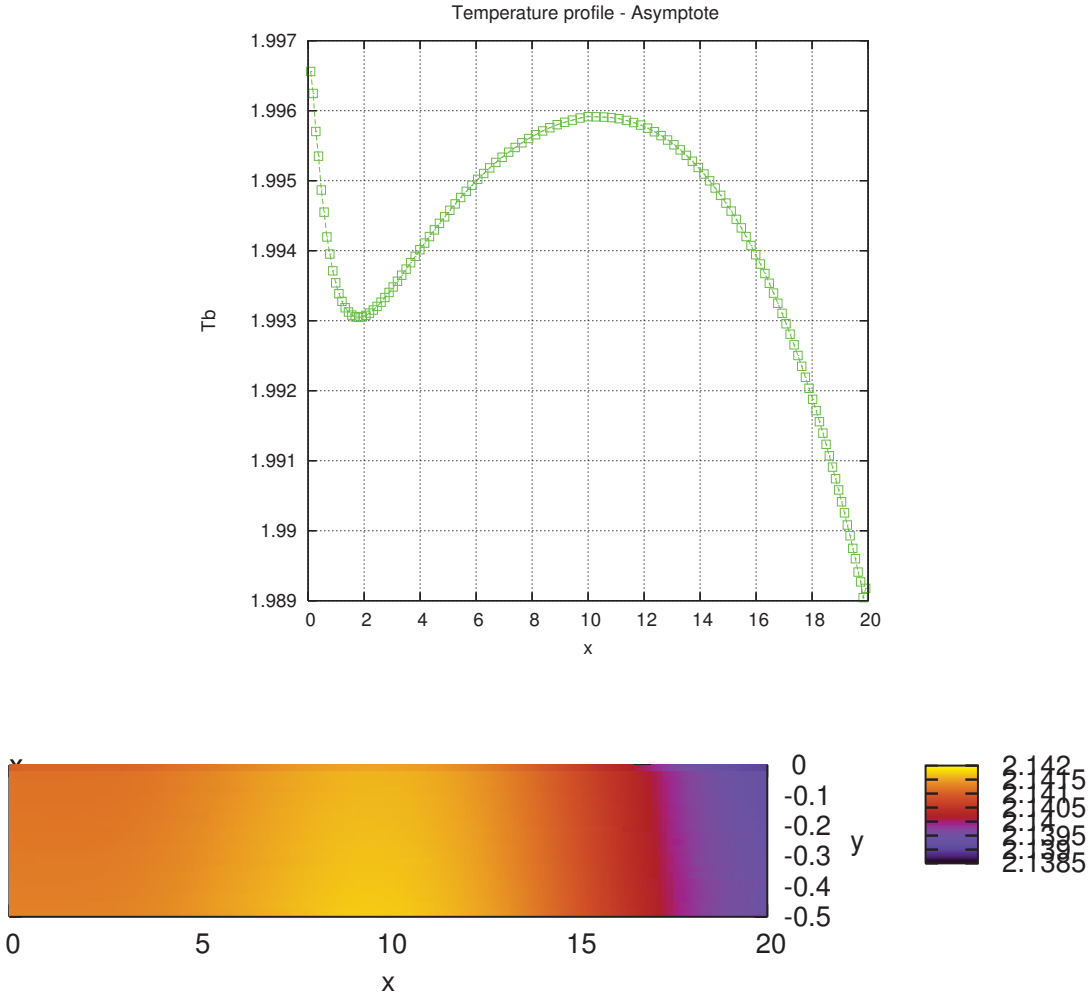

Figure 4.8a and 4.8b: Wall temperature profile and map in the asymptote case, low flux $q'' = 10$, $Ma_e = 0.4$.

Further increasing the mach number the effect enhances yielding a remarkable drop of the bulk temperature towards the exit of the channel as shown by Fig.4.9 where the exit Mach number is approximately equal to 0.8. In this condition the wall temperature near the outlet decreases. It is worth to remind that this condition is close to the maximum efficiency attainable, since for a constant section duct with subsonic inlet the exit Mach cannot exceed unity.

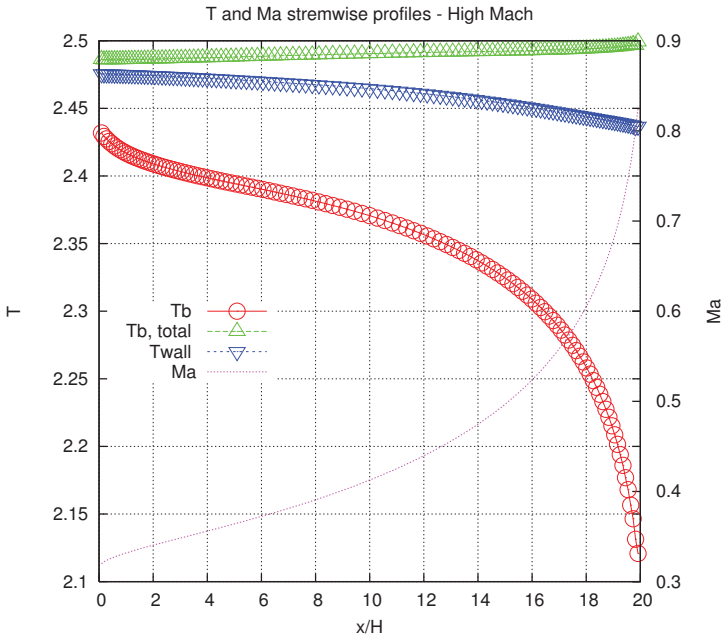

Figure 4.9: Temperature and Mach streamwise profiles, low flux $q'' = 10$, $Ma_e = 0.8$.

4.2.2 Isentropic Heat Sink Performance

The conjugate heat transfer has an impact on the location of such an asymptote: in particular, axial conduction will expand backwards, namely towards the wall low temperature area at the channel exit, thus effectively moving the asymptotes towards lower exit Mach conditions, as shown in Fig.4.5.

In other words, the CHT effect pushes the asymptote towards low Mach numbers which means that the dynamic cooling described above occurs at lower Mach number with the presence of the wall.

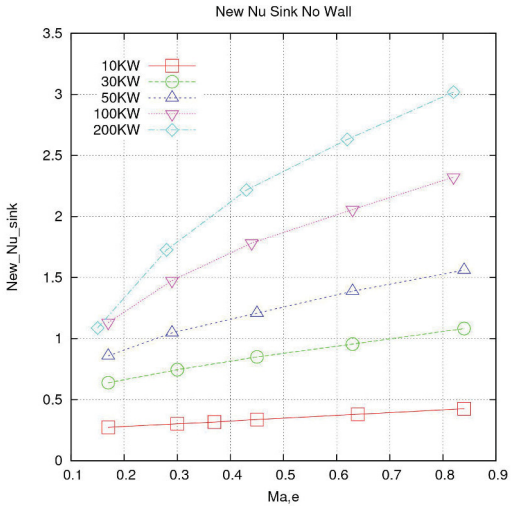

Figure 4.10a: Modified heat sink efficiency, no wall case, eq.(4.8).

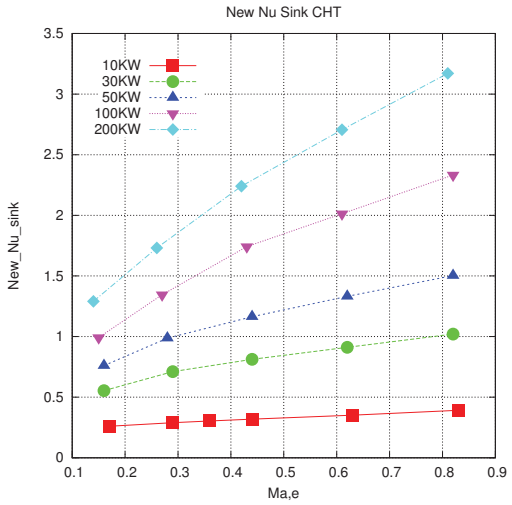

Figure 4.10b: Modified heat sink efficiency, CHT case, eq.(4.8).

Thus, it is not correct to implicitly assume, in equation (4.6), that the inlet temperature is the lowest possible in the system. More reasonably, we can refer to an isentropic exit temperature in choked flow conditions, i.e. at the maximum possible flow rate (as long as we have a constant section duct):

$$T_{e_{is}} = \frac{2T_i^0}{\gamma + 1} \tag{4.7}$$

Therefore, we can reformulate the definition of ε as following:

$$\varepsilon' = \frac{q'' D_h}{\lambda_f (\overline{T}_w - T_{e_{is}})} \tag{4.8}$$

which we called the *Isentropic Heat Sink Performance*.

The results are plotted in Fig.4.10, and show a more reasonable, less puzzling monotonic behavior with respect to the exit Mach number. Now, the heat sink efficiency increases monotonically with exit Mach number, coherently with the observed reduction in average wall temperature.

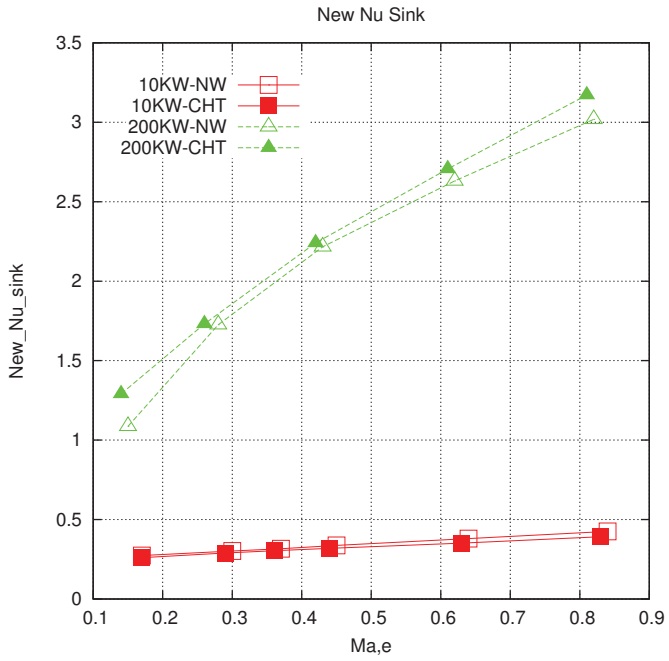

Figure 4.11: Modified heat sink efficiency, eq.(4.8), full conjugate computation (CHT) and neglecting wall conduction (NW).

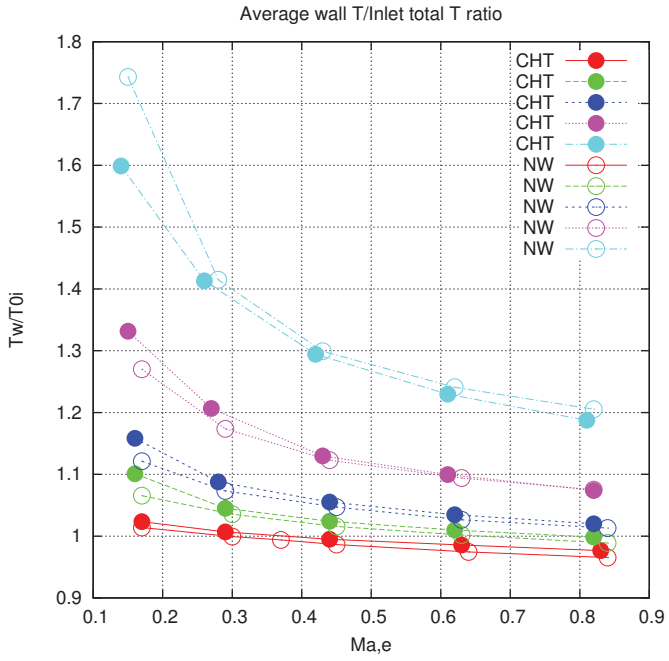

Figure 4.12: Average wall temperature/inlet total temperature ratio: full conjugate computation (CHT), no wall conduction (NW).

It is important to remind that, if we have significant expansion and a high exit Mach number, the exit fluid section might be the lowest temperature one. In such case, the axial conduction heat transfer may be even beneficial to the wall cooling, since it helps to redistribute the high exit heat flux removal along the whole of the wall. This is clear in Fig.4.11, where, at least at higher heat transfer rate, the heat sink efficiency parameter is increased by the axial conduction.

It is worth noting that the axial conduction number, for the high flux results given in Fig.4.11, decreases monotonically from a maximum value M=0.16 at Ma_e=0.14 to a minimum of M=0.02 at M_{ae}=0.8. Nonetheless, the effect of CHT does not follow the same trend: the discrepancies between full CHT and pure fluid computation have a minimum around M_{ae}=0.4 and increase for both lower and higher values. This is because the CHT effect is related to two competing phenomena: the standard heat loss along the wall, bigger for large M (and, here, low Ma), and the exit cooling due to acceleration, at larger Ma (and, here, lower M).

Finally, in Fig. 4.12, we can show the ratio between average wall temperature and inlet total temperature for each heat flux applied: it is again apparent that wall heat conduction contribution has different effects, depending on the heat flux [50].

At the end it is worth showing the temperature distribution on the micro heat sink, for the two extreme cases of heat flux (10 and 200 KW/m^2) and different values of the exit mach number, in order to give a clearer idea of the phenomena occurring (figures 4.13a-4.13f not to scale).

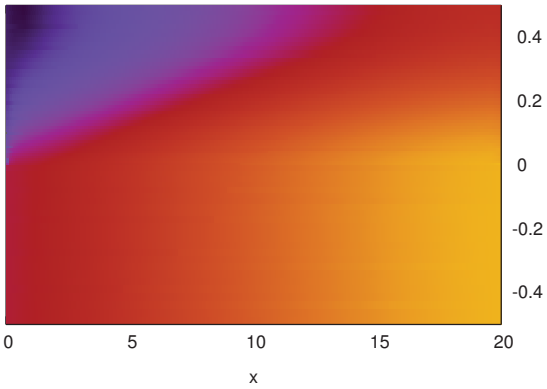

Figure 4.13a: Temperature map for $q" = 10$, $Ma_e = 0.165$.

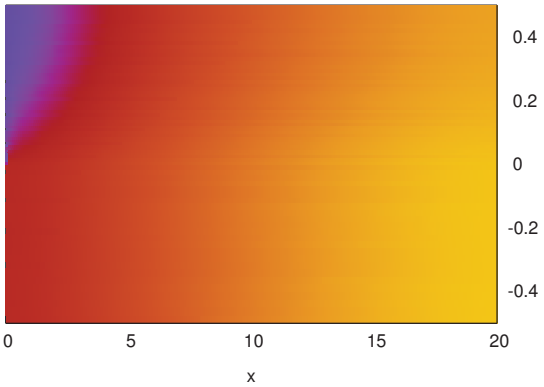

Figure 4.13b: Temperature map for $q" = 200$, $Ma_e = 0.14$.

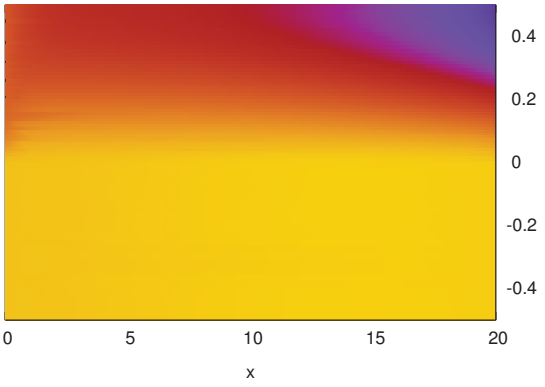

Figure 4.13c: Temperature map for $q" = 10$, $Ma_e = 0.4$.

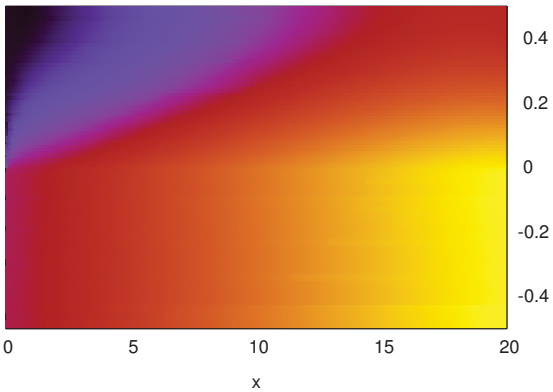

Figure 4.13d: Temperature map for $q" = 200$, $Ma_e = 0.42$.

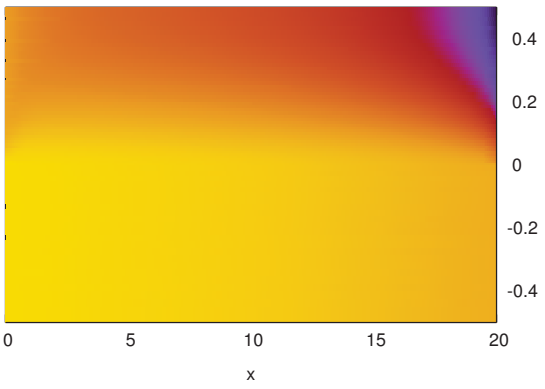

Figure 4.13e: Temperature map for $q" = 10$, $Ma_e = 0.83$.

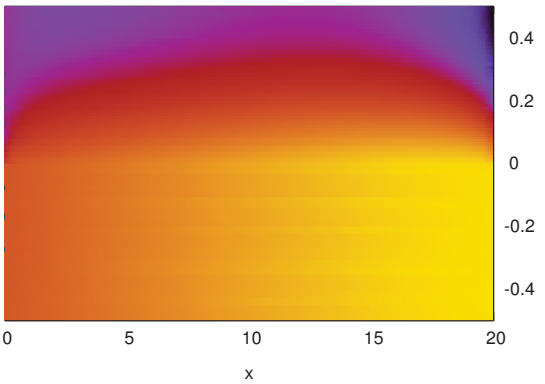

Figure 4.13f: Temperature map for $q" = 200$, $Ma_e = 0.81$

4.2 Micro Heat Exchanger

Several simulations have been carried out using different Reynolds numbers (eq. 4.1), Isentropic Mach number (eq. 4.2, related to the pressure drop) and inlet temperatures for each side of the exchanger.

A plane short heat exchanger of length *L* with channels of height *H* is considered, Fig.4.14. The wall between the hot and the cold side is *H/2* thick. The fluid considered is still air which has a specific heat ratio γ= 1.4 and a Prandtl number *Pr* = 70.

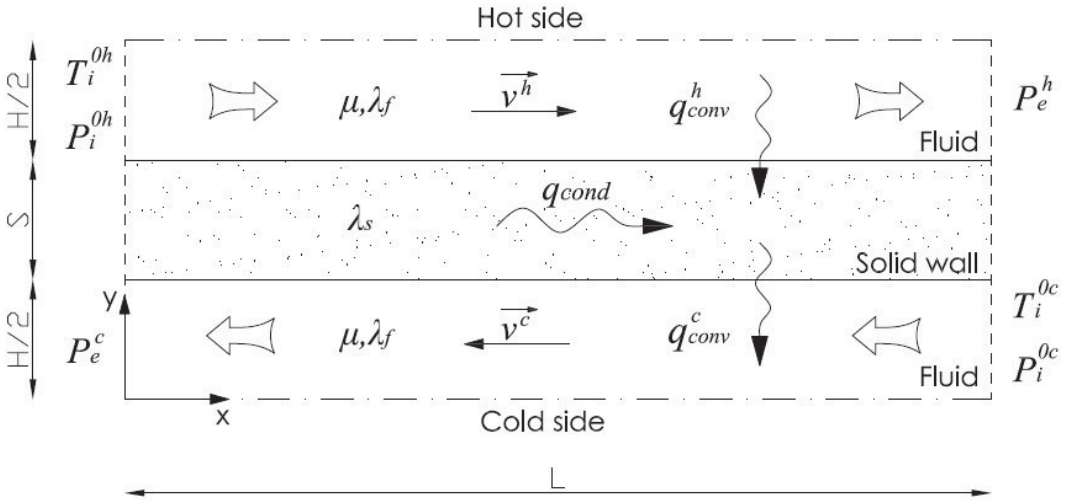

Fig. 4.14: Micro heat exchanger configuration.

Although the equations are cast in non-dimensional terms, the range of values that characterize each case simulated were chosen as representative of a configuration of practical interest. In particular, the ranges of the parameters used, are listed below:

- Fluid: air (γ=1.4)
- Reynolds Number: $18 < Re < 10$
- Pressure Ratio: $1.3 < \beta < 3.0$
- Channel Height: H = 10 μm
- Channel Length: $L = 20H, 100H$
- Conductivity Ratio: $10 < \Lambda < 100$

The conductivity ratio Λ ranges between 20 and 100 and has been chosen specifically to obtain considerable Conjugate Heat Transfer effects. An optimum value of such ratio will be sought. Although these values may seem relatively low (for a metal – gas coupling we can easily get up to 10^3), results will show that higher conductivities are detrimental for the HT performances.

The parameter that characterizes each case (along with the pressure ratio), in analogy with the heat flow rates for the heat sink, is the inlet temperature of the hot fluid which assumes the following values:

- T_i^{0h} = 20, 40, 60 , 80, 100 °C.

Table 4.3 summarizes the ranges of values of all the parameters involved and that characterize the flow under exam.

Parameter	Symbol [dim]	Min value	Max value
Reynolds Number	Re	18	100
Isentropic Mach Number	Ma_{is}	0.6	1.4
Pressure Ratio	β	1.3	3.0
Channel Height	H [μm]	10	
Channel Length	L [H]	20	100
Conductivity Ratio	$\Lambda=\lambda_s/\lambda_f$	10	100
Specific Heat Ratio	γ	1.4	
Temperature Ratio	τ	0.035	0.318
Axial Conduction Number	M	0.05	0.2
Exit Average Mach Number	Ma_e	0.09	0.86
Exit Knudsen Number	Kn_e	0.006	0.009

Table 4.3: Main parameter ranges for the micro heat exchanger.

Another fundamental characteristic in this analysis is the is the conductivity ratio Λ, already mentioned above, because it is the parameter that permits to investigate the conjugate heat transfer effects, while for the heat sink case such effects were investigated comparing each case with its analogous with no wall.

The following tables show all the parameters used in the computation for each simulation carried out.

Heat Exchanger cases analyzed, L=20H , H=10µm, $T_{0,in,C}$=283 K, p_{out}=1 atm, Λ=100 (Counter-C & Co-C)				
N	β (H &C side)	$M_{a,is}$ (H &C side)	Re_{is} (H side)	$T_{0,in,H}$ [K]
1	1.3	0.62	137	293
2	1.3	0.62	142	313
3	1.3	0.62	146	333
4	1.3	0.62	151	353
5	1.3	0.62	155	373
6	1.5	0.78	169	293
7	1.5	0.78	175	313
8	1.5	0.78	180	333
9	1.5	0.78	186	353
10	1.5	0.78	191	373
11	2.0	1.05	217	293
12	2.0	1.05	224	313
13	2.0	1.05	231	333
14	2.0	1.05	238	353
15	2.0	1.05	245	373
16	2.5	1.22	245	293
17	2.5	1.22	254	313
18	2.5	1.22	262	333
19	2.5	1.22	269	353
20	2.5	1.22	277	373
21	3.0	1.36	265	293
22	3.0	1.36	274	313
23	3.0	1.36	283	333
24	3.0	1.36	291	353
25	3.0	1.36	300	373

Table 4.4: First set of simulations and parameters chosen for micro Heat-exchanger analysis.

Each simulation in table 4.4 has been carried out for both counter-current and co-current configurations.

Heat Exchanger cases analyzed, H=10μm, $T_{0,in,C}$=283 K , β=2, p_{out}=1atm (symmetric H & C)			
N	***L***	$T_{0,in,H}$	**Λ**
1-6	20	293	20, 40 ,60 ,80 ,90, 100
7-12	20	313	20, 40 ,60 ,80 ,90, 100
13-18	20	333	20, 40 ,60 ,80 ,90, 100
19-24	20	353	20, 40 ,60 ,80 ,90, 100
25-30	20	373	20, 40 ,60 ,80 ,90, 100
31-35	40	333	20, 40 ,60 ,80, 100
36-40	60	333	20, 40 ,60 ,80, 100
41-46	80	333	10, 20, 40 ,60 ,80, 100
47-52	100	333	10, 20, 40 ,60 ,80, 100

Table 4.5: Second set of simulations and parameters chosen for micro Heat-exchanger analysis: conductivity ratio and channel length are considered as main parameters.

All the simulations are characterized by the same pressure drop on both hot and cold side of the heat exchanger.

The most common performance parameters for heat transfer in micro or macro channels is the Nusselt number *Nu*, related to the ratio between actual total heat transfer and the conductive one from the fluid to the solid; thus, if α is the local heat transfer coefficient we may define a local Nusselt:

$$Nu(x) = \frac{\alpha D_H}{\lambda_f} = 2\frac{q'' H}{\lambda_f \left(T_{w,x} - T_{b,x}\right)} \tag{4.9}$$

Furthermore, for a heat exchanger configuration, it is worth to define the heat exchanger efficiency ε, ratio between the actual heat transfer rate and the maximum possible one (for an infinite surface). Since we have the same pressure ratio in both channels, due to the lower density the hot flow will be characterized by the minimum value of the product $\dot{m}c_p$, so that the efficiency can be defined in terms of stagnation inlet and outlet conditions as:

$$\varepsilon = \frac{T_i^{0h} - T_e^{0h}}{T_i^{0h} - T_i^{0c}} \tag{4.10}$$

4.2.1 Local thermal field

The plots of bulk stagnation temperature along the streamwise direction may give a first indication on the significant discrepancies between the behavior of gas flow in microscale and the standard behavior of nearly incompressible, macroscale heat exchangers. Fig.4.15 shows such a plot for a very short channel (L/H=20) at a low pressure ratio β=1.3. Despite a relatively high conductivity ratio Λ=100, the temperature distribution is qualitatively similar to that of a short macroscale heat exchanger: due to similar mass flow and fluid type on both side, the wall temperature is more or less an average value between the two stream values.

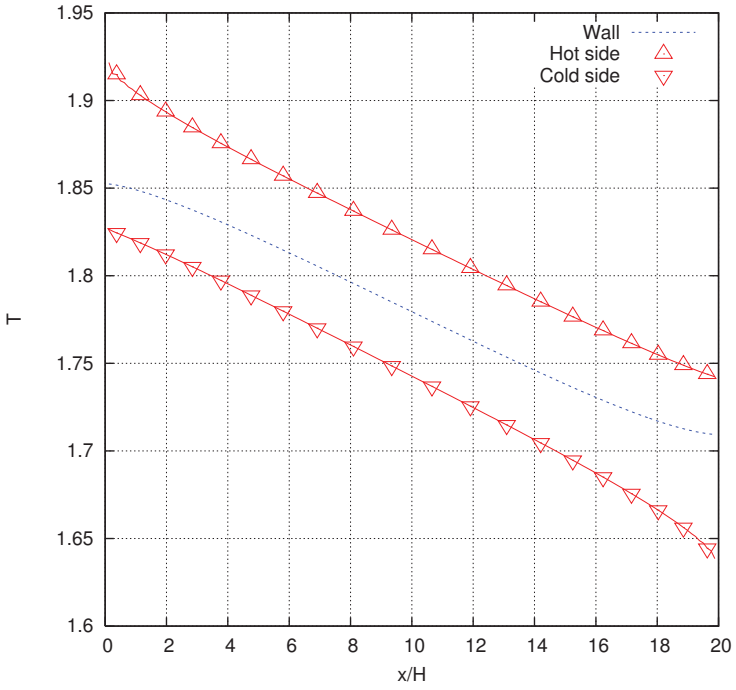

Figure 4.15: Stagnation bulk temperature, β=1.3, τ=0.18, Λ=100

At a higher pressure ratio, β=2.0 (Fig.4.16), the local Mach number increases and the static fluid temperature on both streams drops below the stagnation value. Thus, wall temperature gets closer to the colder stream stagnation one. This is clearly a compressibility effect, not related to the axial flow conduction, since the trend is nearly the same at both Λ=100 and Λ =20: the only difference is in a more pronounced effect of conduction of the wall temperature close to the inlet and exit

section for the case Λ =100. On the other hand, Fig.4.17 demonstrates that for a longer channel (L/H=100), at the same higher pressure ratio β=2.0, there is a much stronger effect of axial conduction, with a different temperature shape corresponding to different Λ. In particular, the result at Λ=100 shows temperature dropping below the inlet temperature of the cold stream. This behavior is explained in Fig.4.18, which shows the temperature profile in y direction at x=100 (hot side exit, cold side inlet).

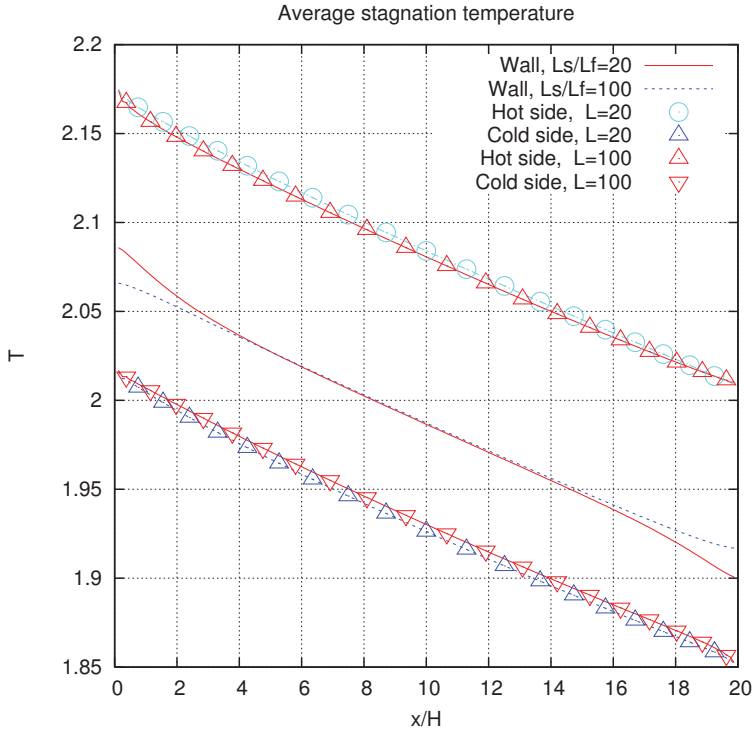

Figure 4.16: Stagnation bulk temperature, β=2.0, τ=0.18, Λ=20,100, L=20

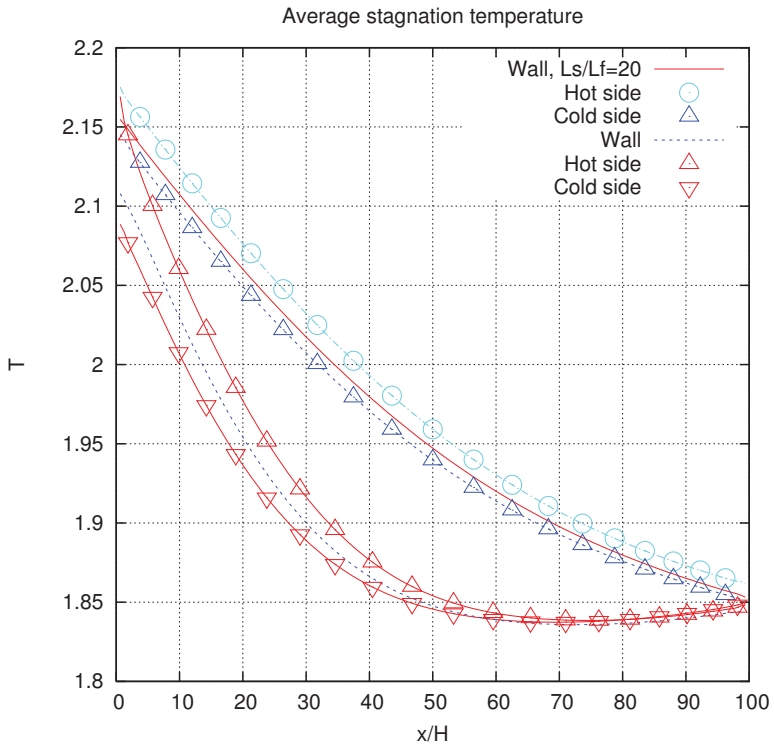

Figure 4.17: Stagnation bulk temperature, β=2.0, τ=0.18, Λ=20,100, L=100

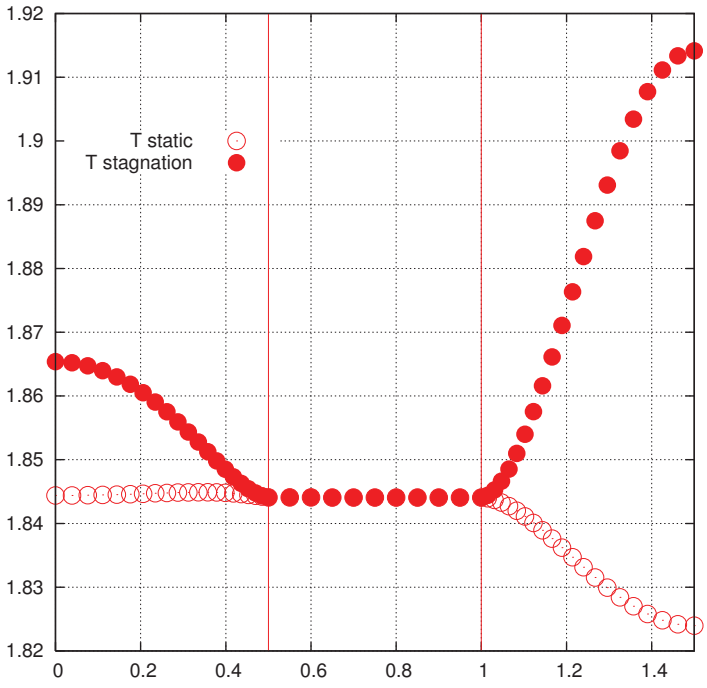

Figure 4.18: Temperature profiles normal to the wall, x=100, β=2.0, τ=0.18, Λ=100

The stagnation bulk temperature difference between the upper (1<*y*<1.5) hot stream and the lower (0<y<0.5) cold one is so small that the cooling to the core flow acceleration is large enough to lower the static temperature of the hot stream actually below that of the cold one, and the lower channel fluid is cooled by the upper flow. With the higher solid conductivity, this overcooling is redistributed over a longer portion of the channel. This is an effect that penalizes the efficiency of the device.

Finally, Fig.4.19 shows an example of local distribution of Nusselt number, typically different on the hot and the cold side.

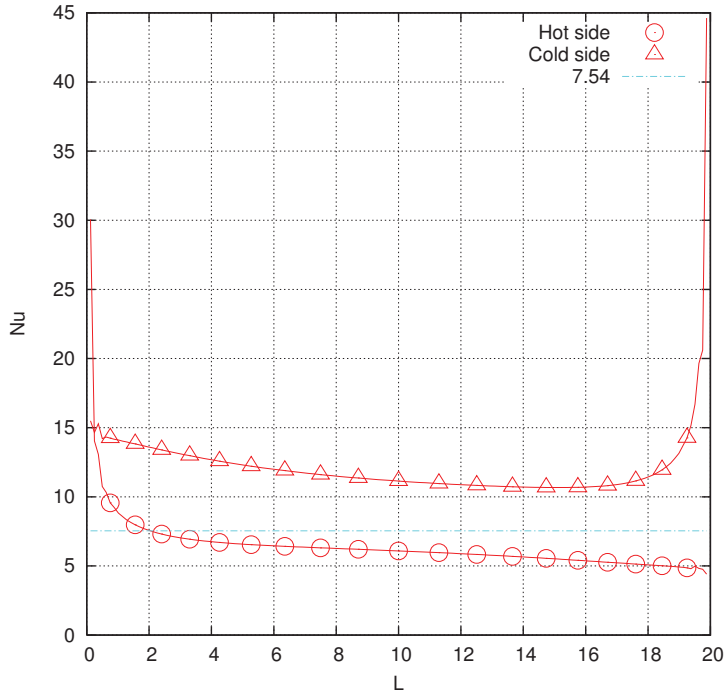

Figure 4.19: Nusselt, β=2.0, τ=0.18, Λ=20

4.2.2 Counter current layout: optimal conductivity

As previously noted, for a microscale heat exchanger the best material is often a relatively low conductive one, in order to avoid efficiency penalization due to the axial conduction through the wall. This effect is verified also in the present configuration of short, compressible flow channels. In particular, Fig.4.20 shows the contour of iso-efficiency for the shortest channel and the whole range of lengths and

conductivity ratios, with a fixed pressure ratio equal to 2 and the same τ=0.18. For the shorter channels the efficiency depends only on the length itself (the longer the channel, the larger the active surface, the larger the efficiency). But when approaching a length to height ratio of 80-100, the iso-lines assume a characteristic curved shape, so that, as an example, for L=60 the maximum efficiency is obtained with a conductivity ratio of around 30. The longer the channel, the smaller the optimal conductivity ratio.

This is clearer in Fig.4.21, where we compare the profile of efficiency as a function of Λ for several channel lengths L. For each channel length all the values are normalized with respect to its efficiency at Λ=100. This allows us to mask the straightforward effect on ε of the mere increase in available surface in the longer channel. For the longest channel the optimal conductivity is of the order of 1, which is qualitatively consistent with experimental considerations and design choice in [1], where a PEEK foil, with Λ of the order of 1 if coupled with air, is chosen as the best material for a heat exchanger with L of the order of 10^2. The same kind of plot of Fig.4.20 may also be expressed in terms of length and Maranzana number M, as given in Fig.4.22.

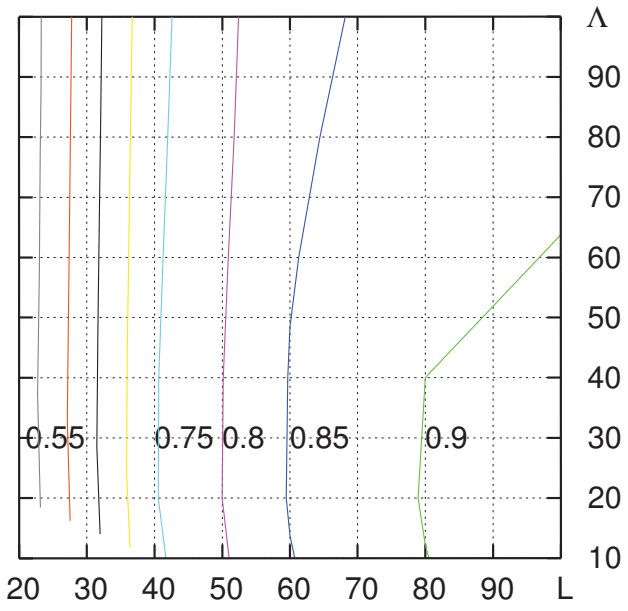

Figure 4.20: Contour plots of heat exchanger efficiency as a function of the channel length L and conductivity ratio Λ.

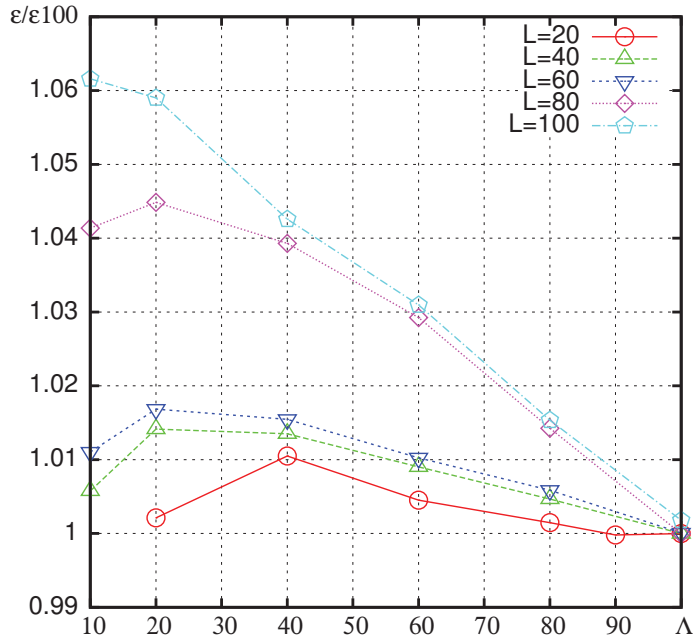

Figure 4.21: Heat exchanger efficiency, normalized for each length via its value at *Λ=100.*

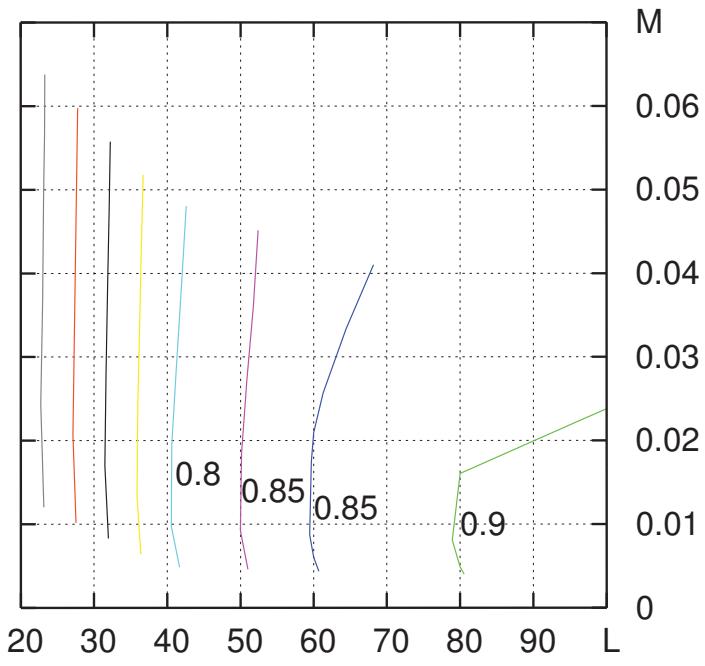

Figure 4.22:. Contour plots of heat exchanger efficiency as a function of the channel length *L* and Maranzana conductivity number.

4.2.3 Counter and co-current configurations

Although the counter-current configuration offers the best efficiencies, local geometrical constraints may force the designer to choose a co-current layout. We can expect that the difference between the two layouts becomes smaller at higher *L*, since the wall tends to become isothermal, but we have also a significant effect of compressibility, if present. In Fig.4.23 the computed efficiency is plotted as a function of the exit Mach number. It is evident that, at low Mach, i.e. negligible compressible effect, we have the maximum gain from the counter-current arrangement. By raising the pressure ratio and the resulting exit *Ma*, the performance reduces due to the fact that conversion of thermal to kinetic energy is dominant, and the two layouts have roughly equivalent performances. This is confirmed in Fig.4.24: the wall temperature contours for the lower pressure ratio, counter current layout (left) show a nearly linear distribution, and the wall is quite far from isothermal. Under the same boundary conditions, the co-current arrangement shows a nearly isothermal wall (Fig.4.24, right). For the highest pressure ratio (Fig.4.25), on the other hand, the streamwise temperature gradients along the wall are smaller, reducing the counter-current advantage.

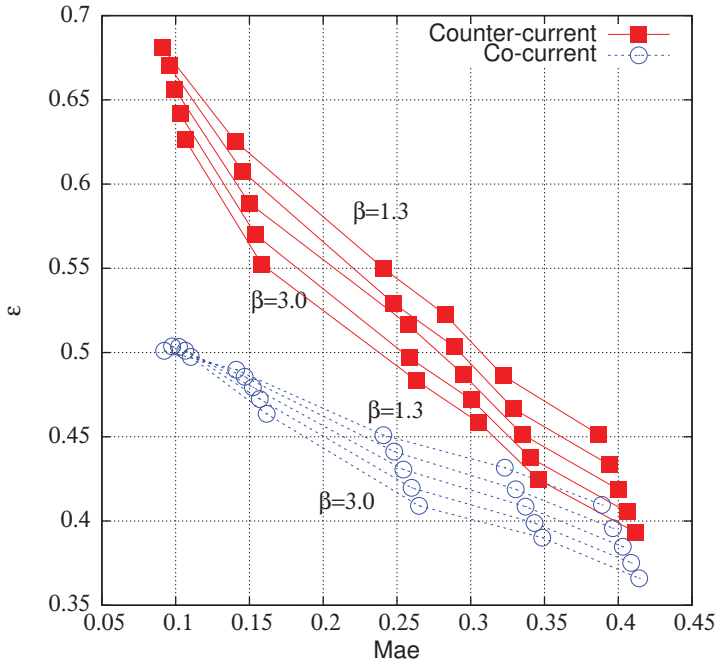

Figure 4.23: Heat exchanger efficiency vs. exit Mach number (hot side) at various pressure ratios, *L*=20.

Looking at the longer channel, Fig.4.26, we notice a much better behavior. Temperature difference on the two sides of the intermediate wall is small, if compared with transverse gradients. This will not only improve the efficiency, but also reduce the entropy production and exergy losses.

4.2.4 Effect of temperature difference

Since temperature and velocity fields are coupled in compressible flow, we may expect an effect of the temperature difference on the performances. In Fig.4.27 we plot the efficiency contours as a function of both exit Mach number (hot side) and the temperature difference. Again, in order to increase the efficiency, lower Mach numbers are required, as well as smaller temperature differences. Since rarefaction and compressibility are correlated, due to equation (3.6), we can expect a similar behavior in Fig.4.28, where the same performance is plotted versus exit Knudsen (hot side) and temperature difference [51].

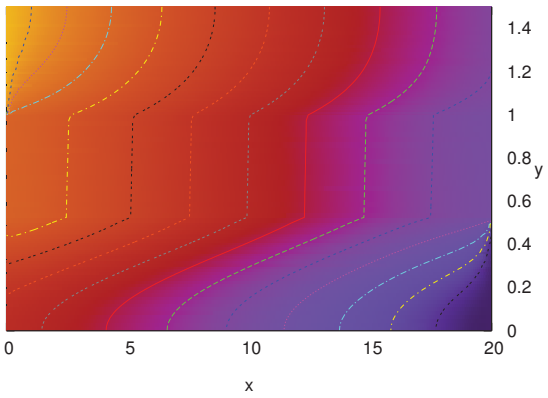

Figure 4.24a: Temperature map and contour (x-y not to scale) for β= 1.3, L=20. - Counter-current configuration.

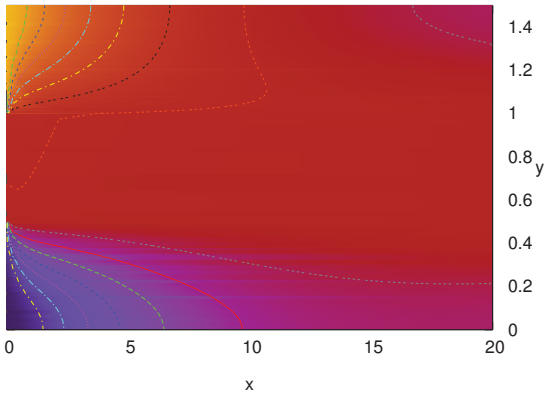

Figure 4.24b: Temperature map and contour (x-y not to scale) for β= 1.3, L=20. - Co-current configuration.

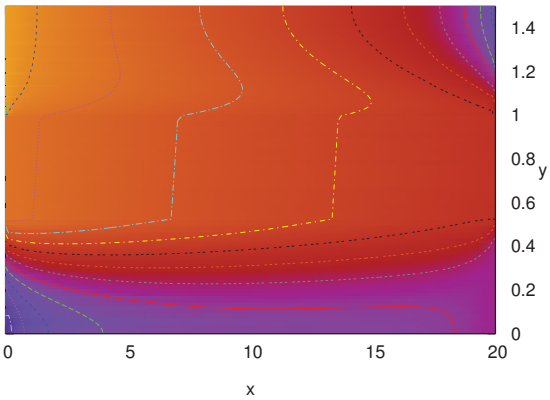

Figure 4.25a: Temperature map and contour (x-y not to scale) for β= 3.0, L=20. - Counter-current configuration.

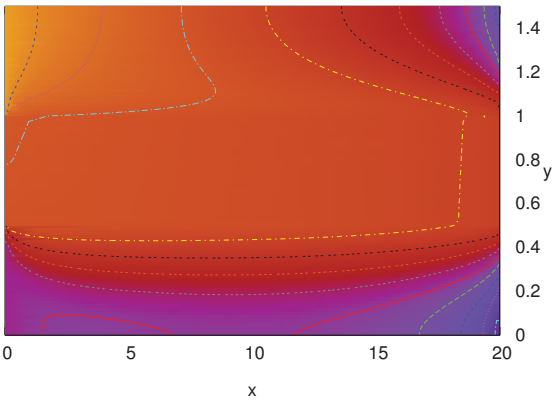

Figure 4.25b: Temperature map and contour (x-y not to scale) for β= 3.0, L=20. - Co-current configuration.

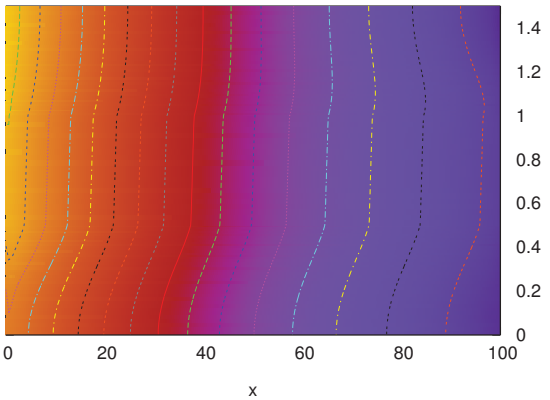

Figure 4.26a: Temperature map and contour (x-y not to scale) for β= 2.0, L=100. - Counter-current configuration, Λ=20.

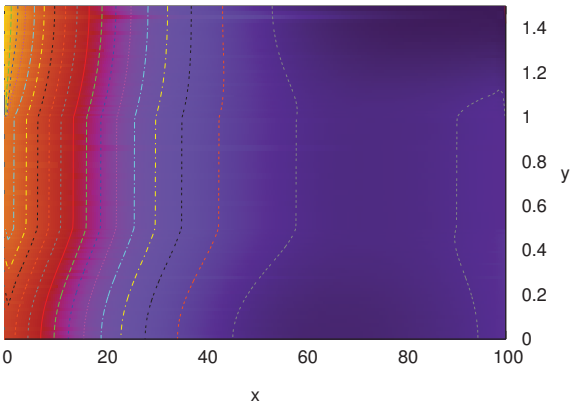

Figure 4.26b: Temperature map and contour (x-y not to scale) for β= 2.0, L=100. - Counter-current configuration, Λ=100.

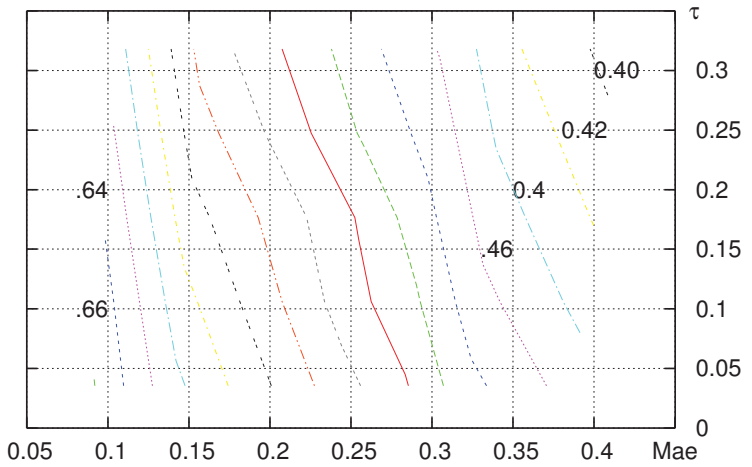

Figure 4.27: Contour plots of heat exchanger efficiency as a function of the channel exit Mach number (hot side) and hot/cold temperature difference.

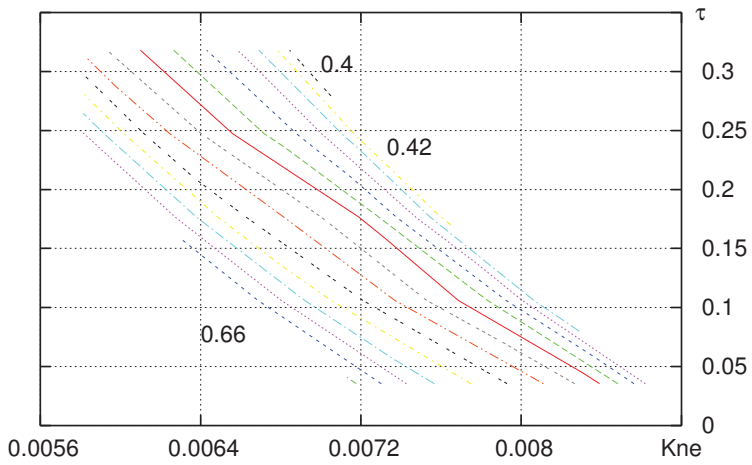

Figure 4.28: Contour plots of heat exchanger efficiency as a function of the channel exit Knudsen number (hot side) and hot/cold temperature difference.

4.3 Correlation for the local stagnation Nusselt number

As demonstrated in the previous sections, the heat transfer performances of the Micro Heat Exchanger are highly dependent on the flow conditions, length of the channel and temperature differences. However, from an engineering point of view, it is not practical to perform a full CFD computation for every single application.

Thus, it would be important to derive a suitable correlation, useful for the heat transfer design process. In particular, it is essential to express such correlation exclusively in terms of local parameters: this, as an example, will allow to use such correlation also in the framework of a porous media model of a heat exchanger.

In the following section, we'll look for such a correlation, possibly expressed in terms of local non dimensional parameters (*Ma, Kn, Re*) and suitable local non-dimensional temperature differences. The main aim is to have a formulation useful for any channel length, flow configuration and inlet temperature differences between the two streams.

4.3.1 Correlation derivation

As inferred from the results obtained from the simulations carried out for the Micro Heat Exchanger, it is evident that Heat Transfer in such devices is strongly determined by the compressibility effects which are represented by the Mach number. In particular, it is important to point out that for a compressible flow the temperature variation is driven by two different phenomena:

- heat transfer between fluid and solid wall;

- conversion of heat into kinetic energy of the flow (or the other way round).

The higher the Mach number more the second effect becomes important. Compressible flows imply that a remarkable amount of heat is transferred to the stream in the form of kinetic energy: as described by the Rayleigh flow theory, we can even have a flow cooling as a consequence of an incoming heat flux.

This is an interesting aspect because the acceleration of the flow contributes in the heat removal along with the convection, and thus enhances the total cooling effect (when heat is removed).

It is important to remind that the ratio behind the definition of the usual Nusselt number is the one to one correlation between the heat flux and a temperature difference: thus, if the chosen temperature difference is a function not only of the heat flux, but also of the flow acceleration, the Nusselt definition loses any physical meaning (hence, the unphysical asymptotes and the negative values). Thus, the choice of a proper temperature difference will be a key point in the search for a useful correlation.

Therefore, as a first step, we define the total (or stagnation) Nusselt number Nu^0 (or for simplicity *Nu,st*) in terms of bulk stagnation temperature as follows:

$$Nu,st(x)=\frac{\alpha D_H}{\lambda_f}=2\frac{q''H}{\lambda_f\left(T_{w,x}-T^0_{T\,b,x}\right)} \tag{4.11}$$

The total bulk temperature, in fact, is a measure of the total energy of the fluid and does not change with the conversion between kinetic and internal energy. This Nusselt number should be correlated to local flow parameters, and such correlation can be sought using all the results available from the computations carried out to study the gas micro heat exchanger behavior.

Due to the previously remarked strong influence of compressibility, a first attempt is to try to fit the *Nu,st* in terms of the local Mach number *Ma*, and possibly in terms of the local Reynolds number *Re*, which is the most representative flow parameter and is present in most of the known convection correlations.

The following figures show that there could be a kind of correspondence between *Nu,st* and *Ma* as well as between *Nu,st* and *Re*.

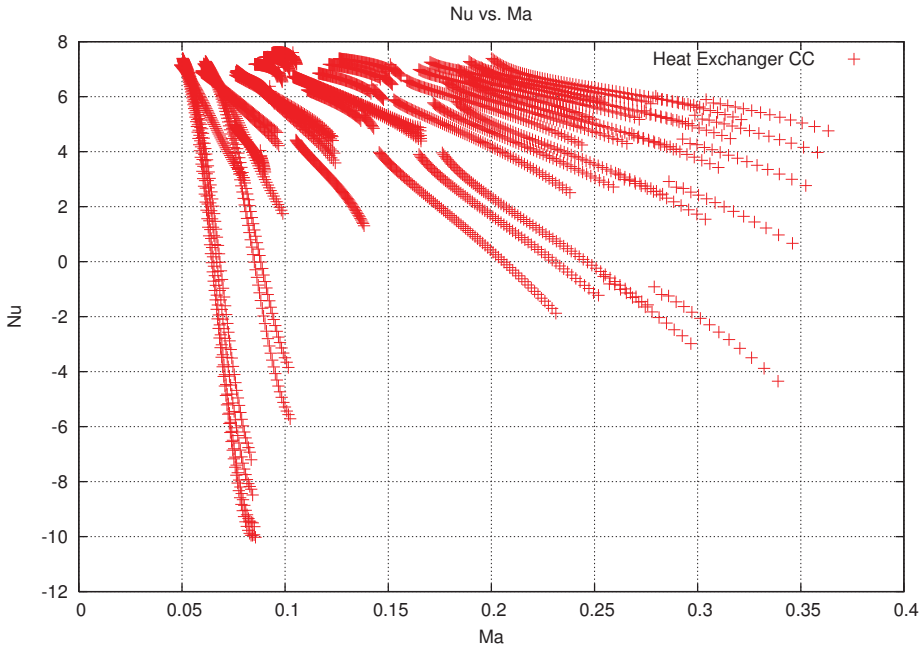

Fig. 4.29: Stagnation Nusselt number plotted vs. the local Mach number. Results from the short micro heat exchanger in counter current configuration.

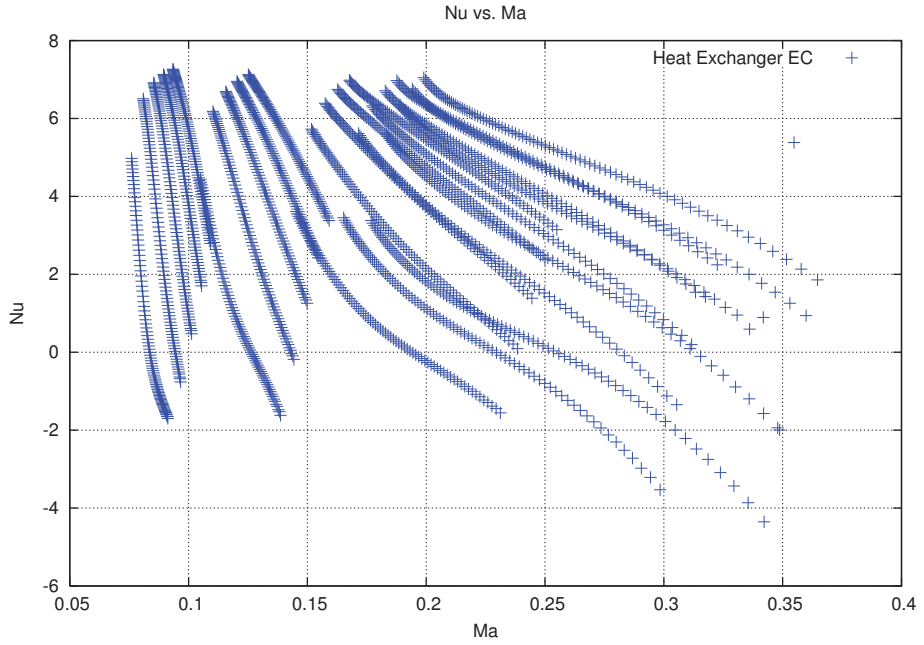

Fig. 4.30: Stagnation Nusselt number plotted vs. the local Mach number. Results from the short micro heat exchanger in parallel flow configuration.

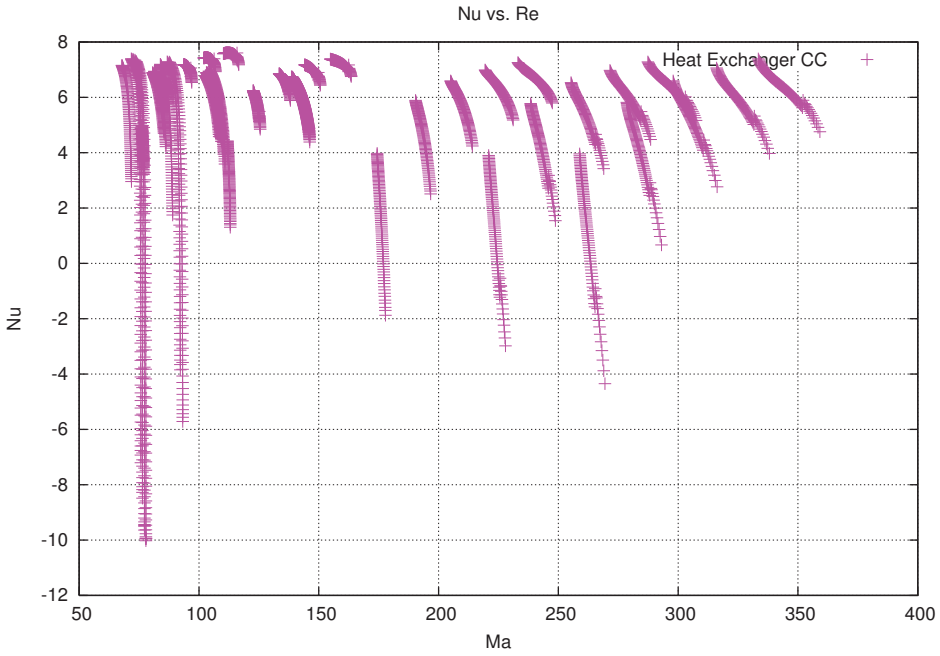

Fig. 4.31: Stagnation Nusselt number plotted vs. the local Reynolds number. Results from the short micro heat exchanger in counter current configuration.

Figs. 4.29-4.31 show some trend, and in particular a clear decrease of *Nu* with either *Ma* or *Re*: however, since we still have a large spread in the quantitative results, it is clear that we have to take in to account some other parameter.

Introducing a significant non dimensional temperature difference, such as $T_b^0 - T_b$, which is proportional to the total amount of energy exchanged in the process, and combining the two parameters *Ma* and *Re*, we can look for a correlation of the form

$$Nu, st(x) = f(Ma(x)) \cdot g(\mathrm{Re}(x)) \cdot h(T_b^0 - T_b) \tag{4.12}$$

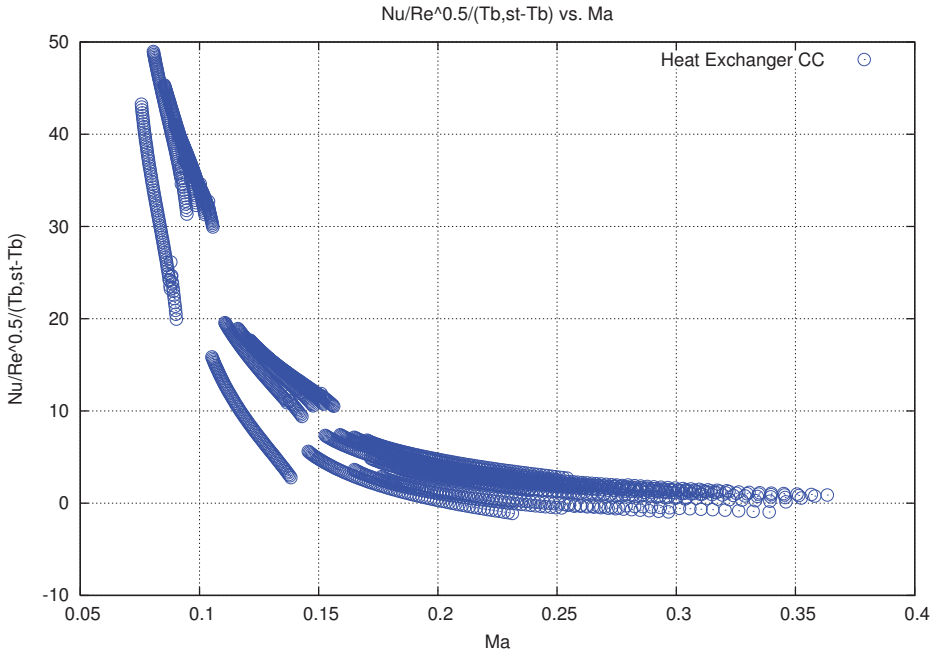

Fig. 4.32: New function of the Nusselt number plotted vs. the local Mach number. Results from the short micro heat exchanger in counter current configuration.

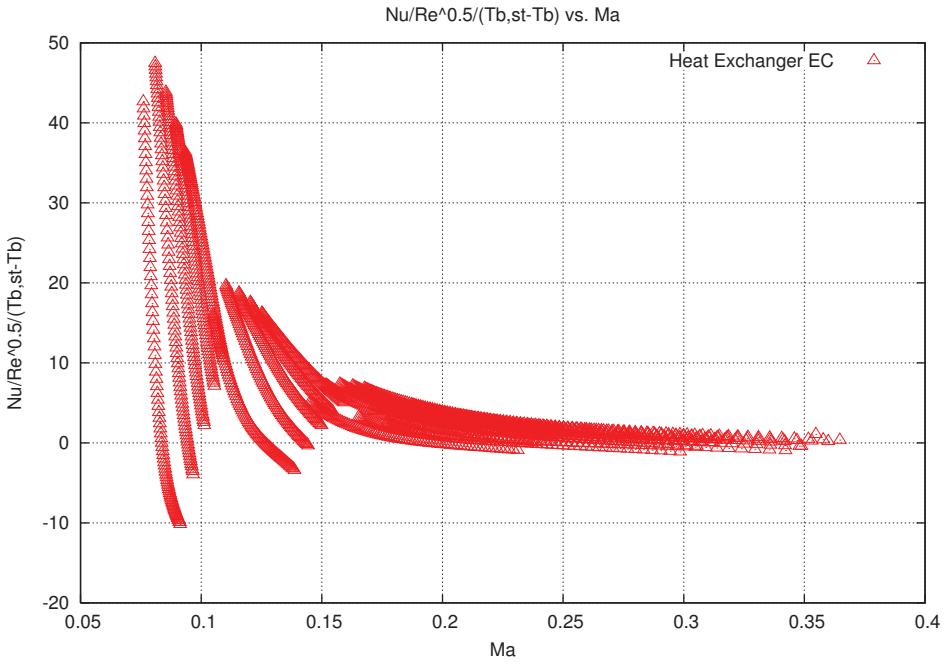

Fig. 4.33: New function of the Nusselt number plotted vs. the local Mach number. Results from the short micro heat exchanger in parallel flow configuration.

In particular, the best results are obtained choosing:

$$Nu, st(x) = \sqrt{\mathrm{Re}} \cdot (T_b^0 - T_b) \cdot f(Ma(x)) \tag{4.13}$$

However, Figs 4.32-4.33 show that we still have several families of curves, and therefore we are not able to have a single definition of *f(Ma)*.

This result suggests that there might be another possible parameter involved, the one necessary to fully align these curves and therefore to lead to the correlation that is being sought. An idea is to try to adopt a different temperature difference but the attempt has not lead to any significant solution.

A meaningful parameter to use that could potentially lead to a correlation could be something that takes into account both the heat transferred from the fluid to the solid wall and the fraction of thermal energy converted to kinetic energy. A reasonable factor should be expressed in terms of two temperature differences such as $(T_{b,st}-T_b)$ and $(T_{b,st}-T_w)$. The first term, as previously mentioned, expresses the amount of energy transferred to the flow as kinetic energy and the second one is proportional to the total heat transferred in the process. Thus a good local parameter to use to correlate the Stagnation Nusselt number could be the non-dimensional parameter

$$\phi = \frac{T_b^0 - T_w}{T_b^0 - T_b} \tag{4.14}$$

a factor that measures the ratio of the intensity of the two energy conversion modalities. A large value of ϕ implies that the temperature variation is essentially driven by the heat transfer, while at small value of ϕ the conversion in kinetic energy is dominant. As φ takes into account the compressibility effects, it is no longer necessary to correlate with the Mach number.

By plotting the *Nu,st* for different configurations of the micro heat exchanger, namely counter flow, parallel flow and long counter flow, all for the hot side of the exchanger, the following four graphics are obtained.

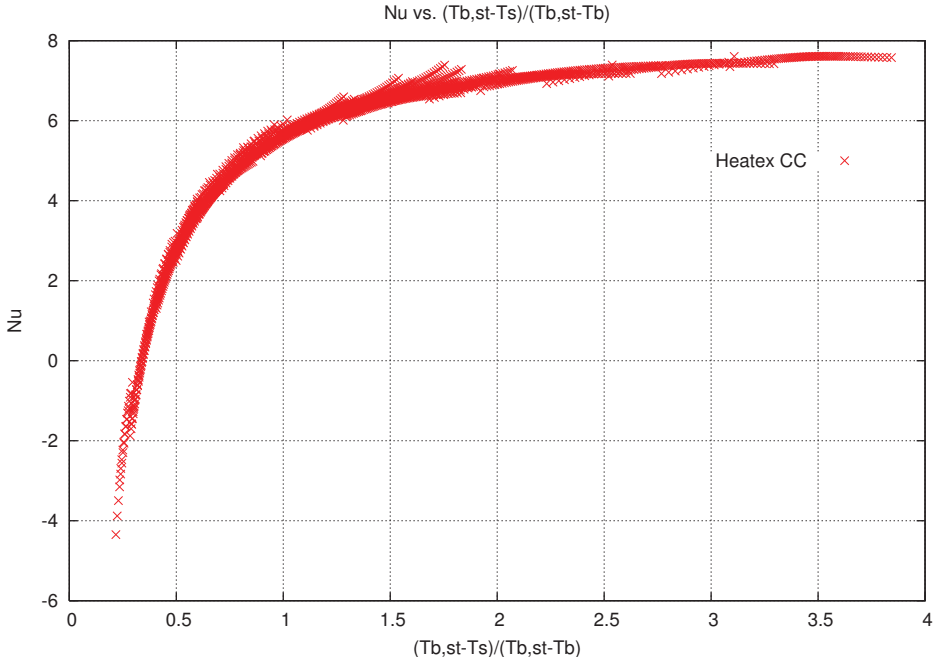

Fig. 4.34: Stagnation Nusselt number plotted vs. the non-dimensional temperature ratio φ. Results from the short micro heat exchanger in counter current configuration.

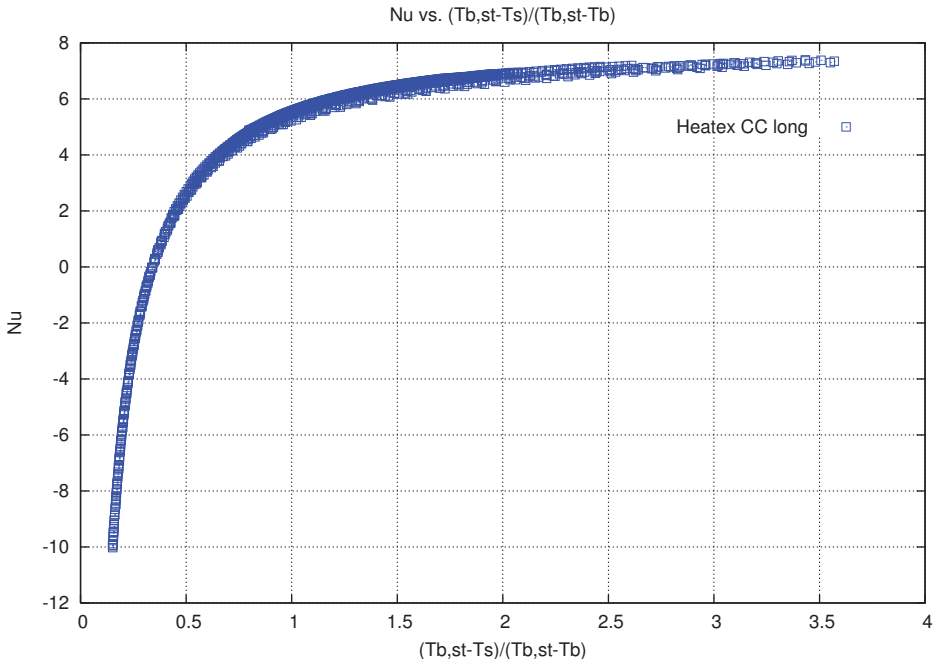

Fig. 4.35: Stagnation Nusselt number plotted vs. the non-dimensional temperature ratio φ. Results from the short micro heat exchanger in long counter current configuration.

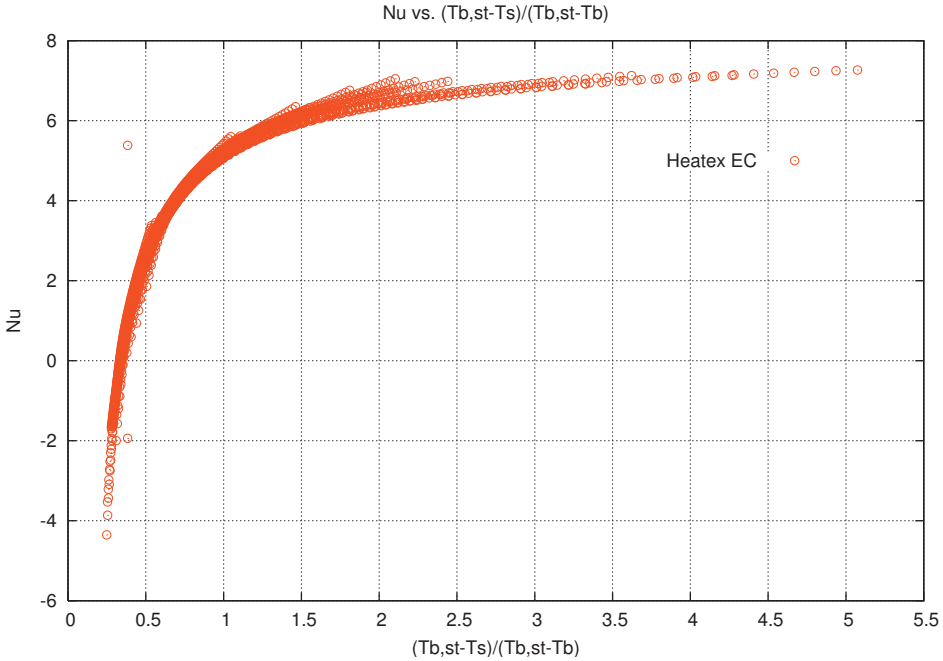

Fig. 4.36: Stagnation Nusselt number plotted vs. the non-dimensional temperature ratio φ. Results from the short micro heat exchanger in parallel flow configuration.

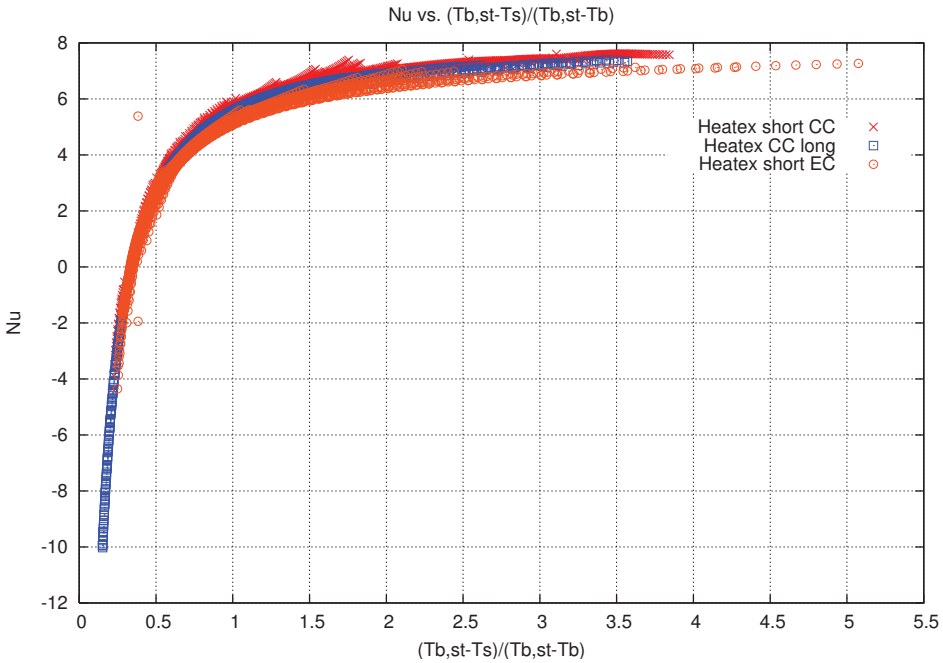

Fig. 4.37: Stagnation Nusselt number plotted vs. the non-dimensional temperature ratio φ. All the results previously displayed.

The last plots show that the data for the hot side of the micro heat exchanger lie with good approximation on a single curve. The shape of the function that interpolates the stagnation Nusselt numbers looks like an hyperbole with asymptotes *x=0* and *y=const*. A reasonable value to give to the constant that defines the asymptote *y* is *7.54* which corresponds to the limit Nusselt for incompressible flows (*Ma→0*).

With these assumptions the function *f(x)* that should fit the results must have the following form:

$$f(x) = 7.54 + \frac{a}{x^b} \tag{4.15}$$

A least-square fitting gives a=-2 and b=1.2, the function is shown in figure 4.38.

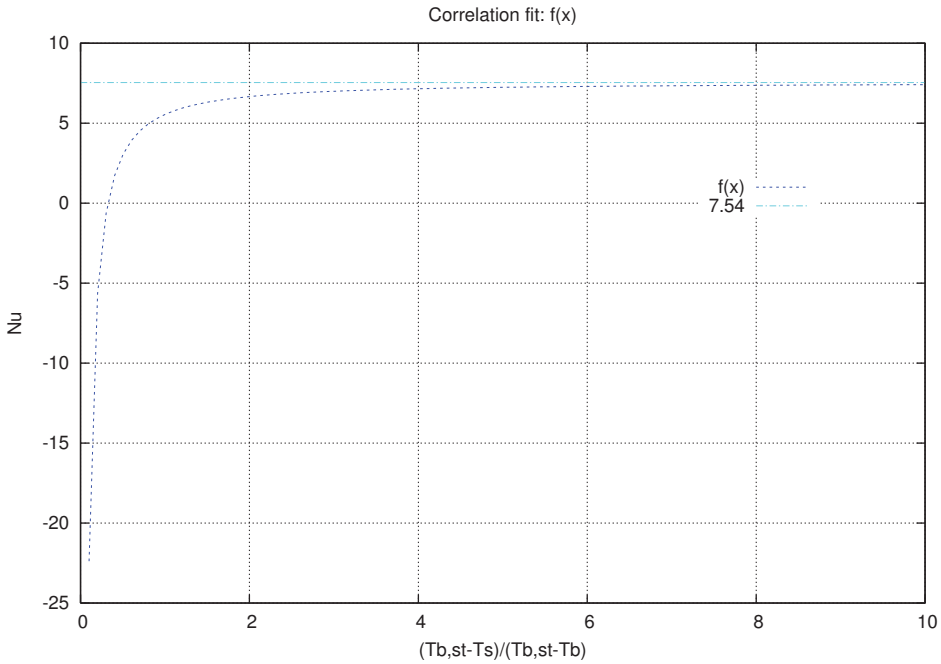

Fig. 4.38: *f(x)* shape with asymptote *y=7.54*.

In figure 4.39 it is shown that such function fits the results pretty well confirming that the approach adopted is correct.

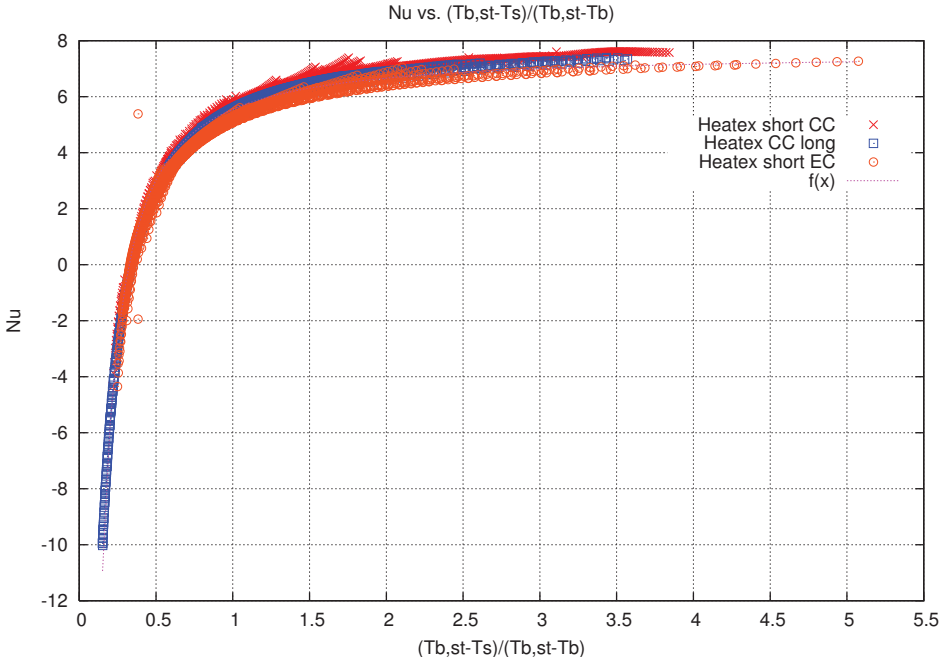

Fig. 4.39: Results fitted for the hot side of the Micro Heat exchanger in different configurations such as parallel flow and long and short counter current.

Therefore the right expression for the *Nu,st* correlation that applies for the hot side of the Micro Heat exchanger is:

$$Nu, st^{h} = 7.54 - 2 \cdot \left(\frac{T_b^0 - T_b}{T_b^0 - T_w} \right)^{1.2} \tag{4.16}$$

The results also fit with good approximation on the cold side as shown in 4.40 and 4.41.

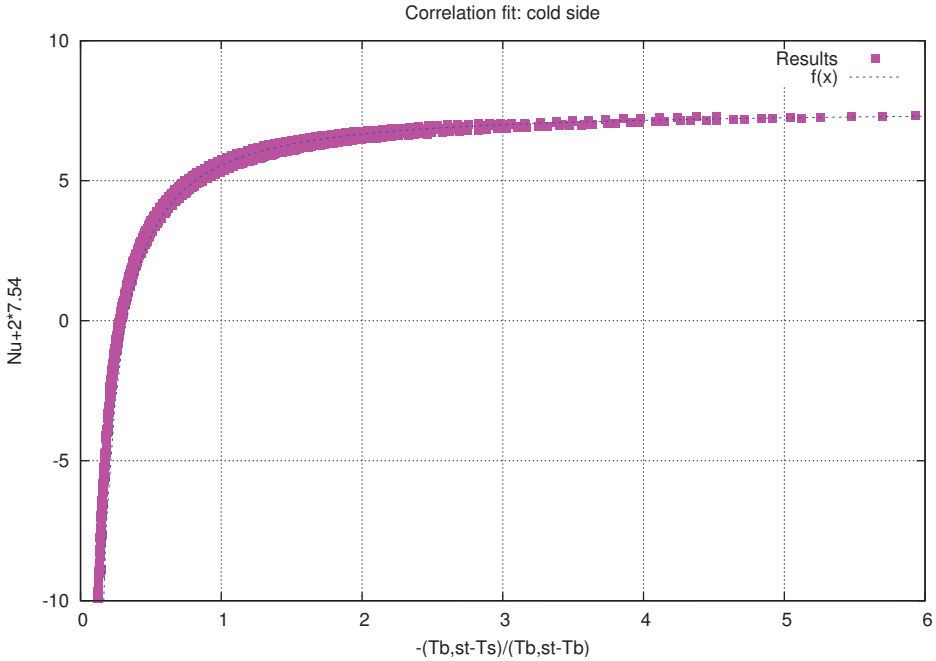

Fig. 4.40: Some results fitted for the cold side of the Micro Heat exchanger. On this side of the device the function has opposite sign since the thermal flux has opposite direction (from wall to fluid).

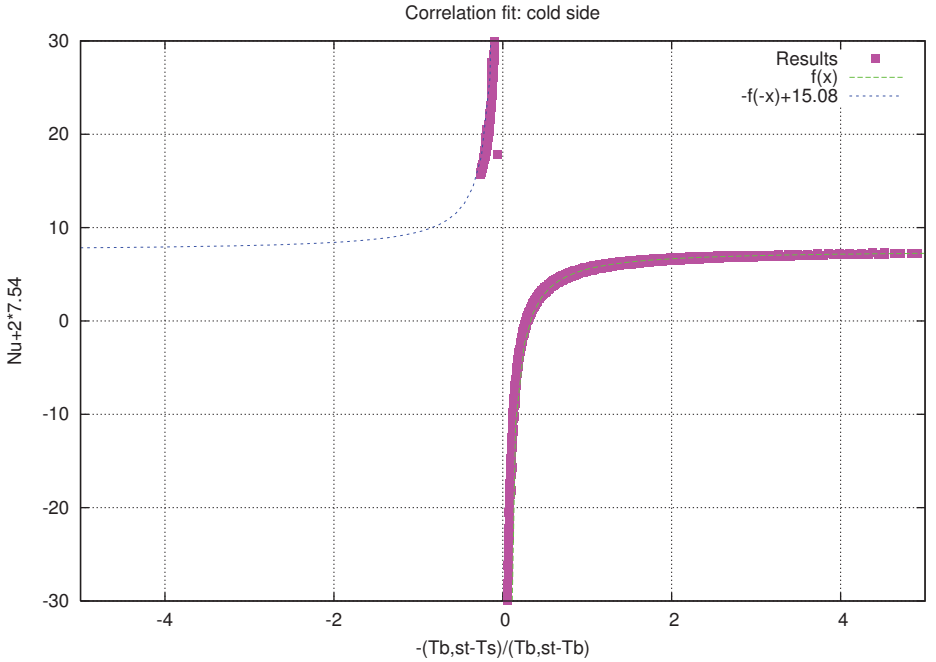

Fig. 4.41: Some results fitted for the cold side of the Micro Heat exchanger. On this side of the device the function has opposite sign since the heat flux has opposite direction (from wall to fluid).

Since the heat flux has an opposite direction on this side of the heat exchanger, from the wall to the fluid, the function must have opposite sign, that is:

$$Nu,st^c = -7.54 + 2 \cdot \left(\frac{T_b^0 - T_b}{T_b^0 - T_w} \right)^{1.2} = -Nu,st^h \tag{4.17}$$

with asymptote equal to y=-7.54.

In the last two figures the results are plotted so as to be displayed concordantly with those of the hot side.

Finally, to confirm and validate the *f(x)* found, and thus the correlation, each *Nu,st* resulted from each computation has been compared with the corresponding one calculated with the correlation.

The results lie in an error band between -15% and + 15%.

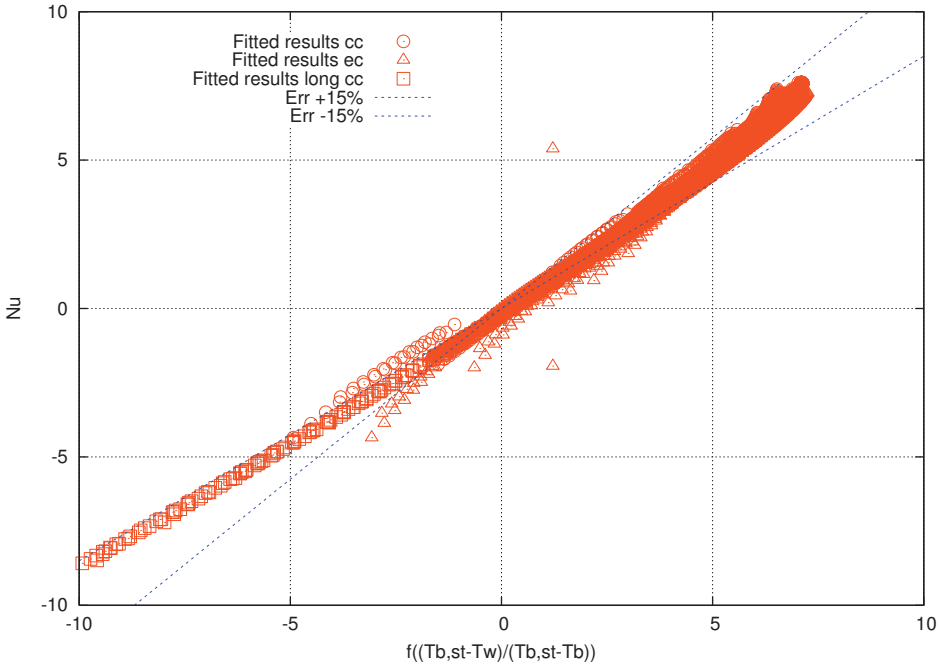

Fig. 4.42: Hot side *Nu,st* resulted from the computations vs. the ones of each corresponding case calculated with the correlation.

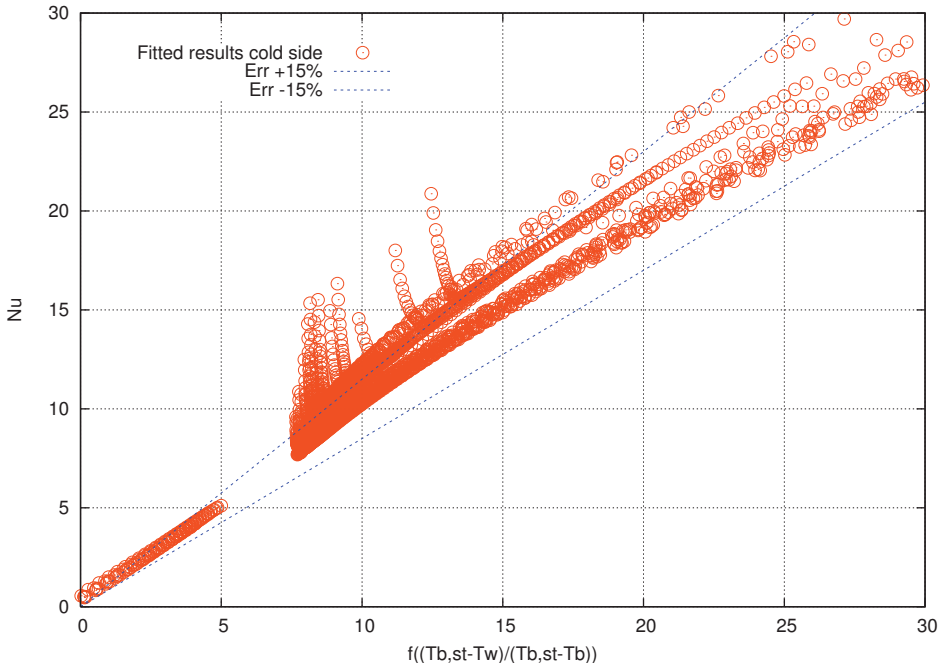

Fig. 4.43: Cold side *Nu,st* resulted from the computations vs. the ones of each corresponding case calculated with the correlation.

A further test, in order to investigate whether the correlation could also depend on the type of gas used, and thus on its thermophysical properties, identified by the two parameters γ and *Pr,* a fair number of simulations has been carried for argon gas instead of air. Argon is characterized by $\gamma \sim 1.66$ *and* $Pr \sim 0.65$.

The results show that a dependence exists and that a reliable first guess is that eq. 4.16 has the following form:

$$Nu, st^h = 7.54 - \frac{3\gamma}{2\varphi^{\frac{6}{5}}} = 7.54 - \frac{3}{2}\gamma\left(\frac{T_b^0 - T_b}{T_b^0 - T_w}\right)^{1.2} \tag{4.18}$$

The last algebraic approximation, obtained fitting the data for air and argon, expresses that the local stagnation Nusselt number depends on both the local flow parameters and on the thermophysical properties of the fluid.

In the following figures a fit for the argon stagnation Nusselt number and total errors for eq. 4.18 are reported.

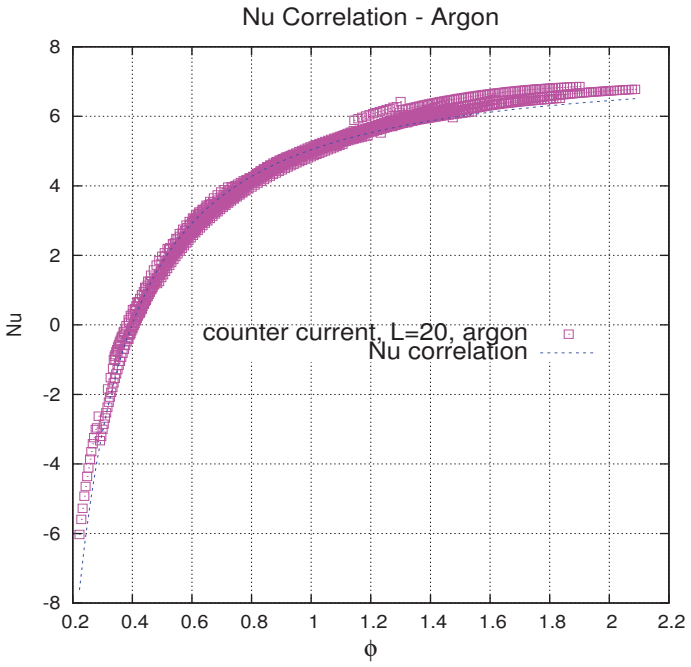

Fig. 4.44: Results fitted for the hot side of the Micro Heat exchanger counter current configuration for argon.

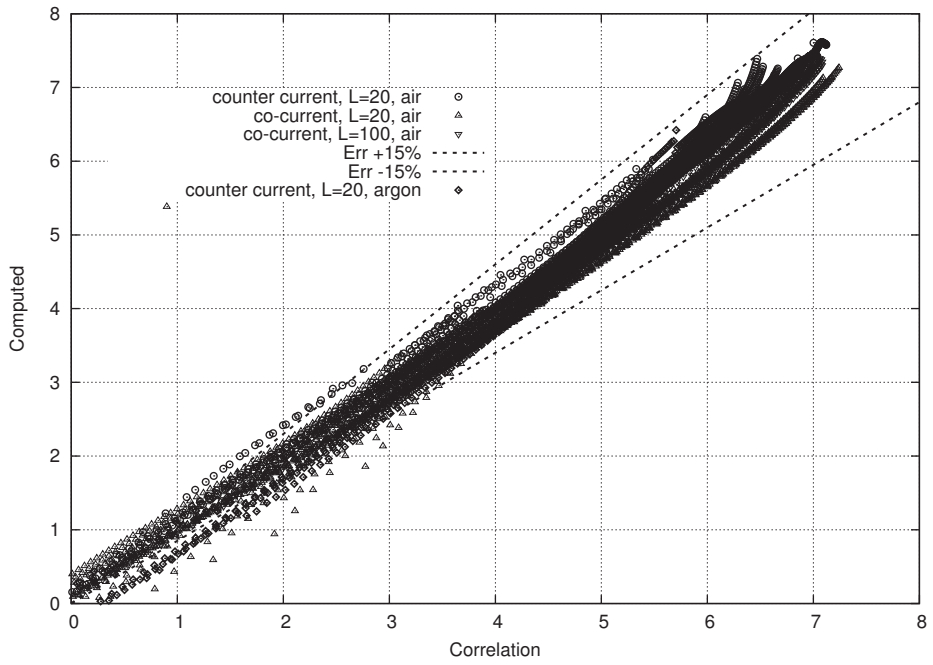

Fig. 4.45: Correlation error in the positive range of Nu^0 for both air and argon.

4.4.2 Applications

Due to several reasons, such as conjugate heat transfer effect, wide range of solid boundary conditions dependent on the heat exchanger arrangement, different possible inlet/outlet configuration, including the possible flow non-uniformity, lack of fully developed condition for compressible flows, the whole micro heat exchanger performances cannot be easily predicted via the standard macro scale approach (based on NTU charts, global transmission coefficients, correction factors for the different configurations). Despite the high efficiency of current CFD tools, however, the detailed simulations of the whole device geometry (including tens, if not hundreds, of micro-channels) is not practical as standard design tool.

A commonly used approximation is based on modelling the whole device as a continuum porous media. Such an approach is offered also in commercial codes, usually only for the purely dynamical analysis (i.e. neglecting the heat transfer): the computational domain covers the whole device, and the single control includes both fluid and solid sections, and the wall effect is introduced via a porous resistance.

This approach is easily implemented for uncompressible macro-flows, where the friction factor is easily determined via correlation based only on the local *Re*, and could be extended to the heat transfer case by defining, at each control volume, three different temperatures (hot side, cold side, wall) and solving the respective energy equations. Nusselt correlation defines the heat transfer, i.e. the source term in each energy equation due to the heat flux from the other components. Some examples are given in open literature [52].

The proposed correlation is, thus, an essential step in order to extend this approach to the microscale compressible case: in fact, since it is based exclusively on local flow parameters, neglecting any global data (channel length, inlet and outlet temperature, pressure ratios), it is capable to reliably compute a local heat flux between fluid and solid under any possible flow arrangement. Furthermore, since we reduced to a dependence only on a single non-dimensional parameter, it ensures high computational efficiency.

CONCLUSIONS

The analysis was at first focused on the wall axial conduction influence, thus on the CHT effect inducing a significant reduction in the wall temperature average slope, for gaseous heat transfer devices consisting of short channels under slip flow regime. Both Heat Sinks and micro Heat Exchangers have been considered.

In every case, in the range of parameters representative of practical applications, compressibility was the dominant factor rather than rarefaction, thermal creep or whatever.

The first conceptual remark is that, in compressible flows, temperature is driven by both heat transfer and kinetic/internal energy conversion. In such devices, the second effect is remarkable, comparing to macro scale analogous configurations, so that it can be considered that the Rayleigh flow effects strongly manifest in gaseous micro flows. Therefore, CHT effect coupled with severe compressibility effect, induces significant difference in behaviour with respect to standard macroscale channels, or even with respect to long micro channels.

Under such conditions the standard definitions of *Nu* and Heat Sink Efficiency ε offer unphysical results (such as asymptotes and negative values): in order to avoid misleading information, such difficulty was overcome introducing the concept of total temperature (measure of total energy, namely internal plus kinetic) in such definitions. In this way the usual performance parameters take into account the flow cooling related to flow acceleration.

Thus:

a) we redefined the Heat Sink efficiency in terms of exit isentropic temperatures (i.e., the actual minimum temperature attainable by the cooling flow, based on the inlet total temperature and isentropic exit Mach number).

This allows to cancel any unphysical behaviour, and compute a Heat Sink Efficiency that correctly monotonically increases with a decrease of the effective wall temperature.

b) we introduced a non-dimensional parameter φ, defined as the ratio between the cooling due to the kinetic component of flow total energy and the temperature difference driving the convective heat transfer. *This single parameter provides a satisfying correlation with the actual local Stagnation Nusselt number*. Such efficient and reliable correlation can be the first building block for an accurate porous media modeling of an actual complex HEX configuration.

It has also been verified that using such modified parameters for the Heat Sink it is apparent that, in particular, wall axial conduction at higher heat fluxes may even enhance the heat removal from the solid.

Moreover, for the Micro HEX, strong CHT effects may induce a significant efficiency penalization for the counter-current approach. This is true especially at low pressure ratios, while increasing the Mach number the performances of both configurations get closer. Since in compressible flow thermal and dynamic fields are coupled, an effect of the value of the inlet temperature difference between hot and cold fluid is detected: in particular, an increase in inlet temperature difference reduces the efficiency.

The new Heat Sink efficiency definition and the Stagnation Nusselt number correlation found, along with all the heat transfer aspects and consequences investigated for the gaseous micro flows analyzed, will allow a deeper understanding and further detailed analysis of the behavior of the gas flow micro devices for engineering applications.

REFERENCES

[1] Yang, Y.H., Morini, G.L., Brandner, J. 2014, "Experimental analysis of the influence of wall axial conduction on gas-to-gas micro heat exchanger effectiveness", *Int. J. Heat Mass Transfer*, 69, pp. 17-25.

[2] Hetsroni, G., Mosyak, A., Pogrebnyak, E., and Yarin, L. P., 2005, "Heat Transfer in Micro-Channels: Comparison of Experiments With Theory and Numerical Results," *Int. J. Heat Mass Transfer*", 48, pp. 5580–5601.

[3] Yarin, L. P., Mosyak, A., and Hetsroni, G., 2009, Fluid Flow, "Heat Transfer and Boiling in Micro-Channels", Springer, Berlin Heidelberg.

[4] Herwig, H., and Hausner, O., 2003, "Critical View on 'New Results in Micro-Fluid Mechanics': An Example", *Int. J. Heat Mass Transfer*, 46, pp. 935–937.

[5] R.B. Peterson, "Numerical modelling of conduction effects in microscale counterflow heat exchangers", Microscale Thermophys. Eng. 3 (1) (1999) 17–30.

[6] T. Stief, O.-U. Langer, K. Schubert, "Numerical investigations of optimal heat conductivity in micro heat exchangers", Chem. Eng. Technol. 22 (4) (1999) 297– 303.

[7] A. Moreno, K. Murphy, B.A. Wilhite, "Parametric study of solid-phase axial heat conduction in thermally integrated microchannel networks", Ind. Eng. Chem. Res. 47 (23) (2008) 9040–9054.

[8] T.-C. Hung, W.-M. Yan, W.-P. Li, "Analysis of heat transfer characteristics of double-layered microchannel heat sink", Int. J. Heat Mass Transfer 55 (2012) 3090–3099.

[9] K. Koyama, C. Hong, Y. Asako, "Effect of partition wall on heat transfer characteristics of a gas-to-gas counterflow microchannel heat exchanger", Heat Transfer Eng. 33 (6) (2012) 533–547.

[10] C. Harris, K. Kelly, T. Wang, A. McCandless, S. Motakef, "Fabrication, modeling, and testing of micro-cross-flow heat exchangers", Journal of Microelectromechanical Systems, 11 (6) (2002) 726–735.

[11] J.J. Brandner, E. Anurjew, L. Bohn, E. Hansjosten, T. Henning, U. Schygulla, A. Wenka, K. Schubert, "Concepts and realization of microstructure heat exchangers for enhanced heat transfer", Exp. Therm. Fluid Sci. 30 (8) (2006) 801–809.

[12] B. Alm, U. Imke, R. Knitter, U. Schygulla, S. Zimmermann, "Testing and simulation of ceramic micro heat exchangers", Chem. Eng. J. 135 (1) (2008) S179–S184.

[13] N. Garcia-Hernando, A. Acosta-Iborra, U. Ruiz-Rivas, M. Izquierdo, "Experimental investigation of fluid flow and heat transfer in a single-phase liquid flow micro-heat exchanger", Int. J. Heat Mass Transfer 52 (2009) 5433– 5446.

[14] W. Bier, W. Keller, G. Linder, D. Seidel, K. Schubert, H. Martin, "Gas to gas heat transfer in micro heat exchangers", Chem. Eng. Process.: Process Intensification 32 (1) (1993) 33–43.

[15] F. Meschke, G. Riebler, V. Hessel, J. Schuerer, T. Baier, "Hermetic gas-tight ceramic microreactors", Chem. Eng. Technol. 28 (4) (2005) 465–473.

[16] K. Koyama, Y. Asako, "Experimental investigation of heat transfer characteristics on a gas-to-gas parallel flow microchannel heat exchanger", Exp. Heat Transfer 23 (2010) 130–143.

[17] Y. Yang, G.L. Morini, J.J. Brandner, "Experimental investigation of thermal performance of gas-to-gas micro heat exchangers as function of the flow arrangement", in: Proceedings of 11th International Conference on Nanochannels, Microchannels and Minichannels, ICNMM2013-73125, Sapporo, June 16–19, 2013.

[18] R. Shah, D. Sekulic, "Fundamentals of Heat Exchanger Design, John Wiley & Sons", 2003.

[19] V.D.I. Gesellschaft, VDI Heat Atlas, Springer, 2010.

[20] Maranzana, G., Perry, I., Maillet, D., "Mini and micro-channels: influence of axial conduction in the walls", 2004, *Int. J. Heat Mass Transfer* 47, pp. 3993-4004.

[21] Croce, G., Comini, G., D'Agaro, P.: "Coupled conduction and convection in coolant passages with arrays of pin fin", 2010, *Computational Thermal Sciences*, 2, pp 43-54.

[22] Lin, T.Y., Kandlikar, S.G.: "A Theoretical Model for Axial Heat Conduction Effects During Single-Phase Flow in Microchannels", 2012, *ASME J. Heat Transfer*, 134.

[23] Croce G., Rovenskaya O, D'Agaro P.: "Computational Analysis of Conjugate Heat Transfer in Gaseous Micro Channels", *ASME J. Heat Transfer*, in press.

[24] Rovenskaya, O. , Croce, G., "Numerical investigation of microflow over rough surfaces: Coupling approach", Journal of Heat Transfer, Volume 135, Issue 10, 2013.

[25] W. Bier, W. Keller, G. Linder, D. Seidel, K. Schubert, H. Martin: "Gas to gas heat transfer in micro heat exchangers", Chemical Engineering and Processing: Process Intensification 32 (1) (1993) 33–43.

[26] F. Meschke, G. Riebler, V. Hessel, J. Schuerer, T. Baier: "Hermetic gas-tight ceramic microreactors", Chemical Engineering & Technology 28 (4) (2005) 465–473.

[27] K. Koyama, Y. Asako: "Experimental investigation of heat transfer characteristics on a gas-to-gas parallel flow microchannel heat exchanger", Experimental Heat Transfer 23 (2010) 130–143

[28] G. Croce, Capitolo 5, "Fondamenti di Termofluidodinamica Computazionale", *Facoltà di Ingegneria, Università degli studi di Udine.*

[29] Bird, G.A., 1998, "Molecular gas dynamics and the direct simulation of gas flows", Clarendon Press, Oxford.

[30] Gad-el-Hak M., 1999, "The fluid mechanics of microdevices-the Freeman scholar lecture", J. Fluid Eng., 121:5-33.

[31] Lengrand J-C, Elzirova TG, 2004, "Microécoulements gazeux". In: Colin S (ed) Microfluidique, chapter 2. Hermès, Paris, France.

[32] Karniadakis G.E., Beskok A., 2002, "Microflows: fundamentals and simulation", Springer, Berlin Heidelberg New York.

[33] Maxwell J.C., 1879, "On stresses in rarefied gases arising from inequalities of temperature", Philos Trans R. Soc., 170:231-256.

[34] Kennard E.H, 1938, "Kinetic theory of gases", 1st ed. McGraw-Hill, New York.

[35] Elbert W.A., Sparrow E.M., 1965, "Slip flow in rectangular and annular ducts", J. Basic Eng., 87:1018-1024.

[36] Morini G.L., Spiga M., 1998, "Slip flow in rectangular microtubes", Microscale Therm. Eng., 2(4):273-282.

[37] Chapman S., Cowling T.G., 1952, "The mathematical theory of non-uniform gases", Cambridge University Press, Cambridge.

[38] Deissler R.G., 1964, "An analysis of second-order slip flow and temperature-jump boundary conditions for rarefied gases", Int. J. Heat Mass Transf., 7:681-694.

[39] Lalonde P., 2001, "Etude expérimentale d'écoulements gazeux dans les microsystems à fluids", *PhD thesis, Institut national des Sciences Appliquées*, Tolouse, France.

[40] Colin S., 2005, "Rarefaction and compressibility effects on steady and transient gas flows in microchannels", Microfluid Nanofluid, 1:268-279.

[41] O. Rovenskaya, G. Croce, Heat Transfer Eng. 34 (2013) 192-203

[42] Croce, G., 1995, "Viscous 3D Cascade Flow Analysis Using an RNG Algebraic Turbulence Mode", ASME Paper No. 95-CTP-78

[43] T.H. Pulliam, J. AIAA 24 (1986) 1931-1940.

[44] Hirsh, C.: "Numerical computation of internal and external flows", John Wiley& Sons Ltd, Chichester, 1990

[45] G. Croce: "A Conjugate Heat Transfer Procedure for Gas Turbine Blades", in Heat Transfer in Gas Turbine Systems, R.J. Goldstein, ed., Annals of NY Academy of Sciences, 2001, pp.273-280

[46] Croce, G., D'Agaro, P., Filippo, a., "Compressibility and rarefaction effects on pressure drop in rough microchannels", 2007, heat transfer Engineering, 28, Issue 8-9, pp. 688-695.

[47] Ebadian, M.A., Lin, C.X., "A Review of High-Heat-Flux Heat Removal Technologies", 2011, *ASME J. Heat Transfer*, 133.

[48] Peles Y., Kosar A., Mishra C., Kuo C.J., Schneider B., 2005, "Forced convective heat transfer across a pin fin micro heat sink", *Int. J. Heat Mass Transfer*, 48, pp. 3615-3627.

[49] C. Nonino, Capitolo 5, "Appunti di Gas Dinamica", *Facoltà di Ingegneria, Università degli studi di Udine.*

[50] Croce, G., Coppola, M.A., Rovenskaya, O., "Conjugate Heat Transfer performances for gaseous flows in short Micro Channels", *ASME 2014.*

[51] Croce, G., Coppola, M.A., "Conjugate Heat Transfer simulation in gaseous flow Micro Heat Exchanger", *ASME 2015.*

[52] Pascoli O., "Analysis and characterization of heat and mass transfer in rotatory exchangers", 2012, *PhD thesis, Università degli studi di Udine.*

APPENDIX A

In the present appendix we describe in detail the non-dimensionalization of the equation, as well as the definition of relevant non-dimensional groups used throughout the thesis.

A.1 General Framework

We first choose a set of reference dimensional quantities. Tildas identify dimensional quantities. Thermophysical properties such as C_p, R, λ and v are always dimensional.

The chosen primary reference quantities are:

- Length: $\tilde{L}$
- Velocity: $\tilde{U}_0$
- Density: $\tilde{\rho}_0$
- Viscosity: $\tilde{\mu}_0$
- Conductivity: $\tilde{\lambda}_0$

The primary reference values allow us to consistently derive the normalization groups for the derived quantities:

- Temperature: $\frac{\gamma \cdot \tilde{U}_0^2}{c_p}$
- Internal energy per unit volume: $\tilde{\rho}_0 \tilde{U}_0^2$
- Pressure: $\tilde{\rho}_0 \tilde{U}_0^2$
- Time: $\frac{\tilde{L}}{\tilde{U}_0}$

A.2 Equation non-dimensionalization

Dimensional form of compressible flow Navier-Stokes (skipping tildas for sake of simplicity) equations:

$$\frac{\partial q}{\partial \vartheta}+\frac{\partial\left(F-F_v\right)}{\partial x}+\frac{\partial\left(G-G_v\right)}{\partial y}+\frac{\partial\left(H-H_v\right)}{\partial z}=0 \tag{A1}$$

The inviscid and viscous flux vectors are defined as in the following:

$$q=\left[\rho,\rho u,\rho v,\rho w,e\right] \tag{A2}$$

$$F=\left[\rho,\rho u^2+p,\rho uv,\rho uw,u\left(e+p\right)\right] \tag{A3}$$

$$F_v=\left[0,\tau_{xx},\tau_{xy},\tau_{xz},\lambda\frac{\partial T}{\partial x}+u\tau_{xx},y\tau_{xy}+w\tau_{xz}\right] \tag{A4}$$

$$\tau_{ij}=\mu\left(\frac{2}{3}\delta_{ij}\frac{\partial u_k}{\partial x_k}+\frac{\partial u_i}{\partial x_i}+\frac{\partial u_i}{\partial x_j}\right) \tag{A5}$$

As an example we explicit the momentum equation in the x-direction:

$$\frac{\partial \rho u}{\partial \vartheta}=-\frac{\partial\left(\rho u^2+p\right)}{\partial x}+\ldots+\frac{\partial\left(\mu\left(\frac{2}{3}\frac{\partial u_k}{\partial x_k}+\frac{\partial u}{\partial x}+\frac{\partial u}{\partial x}\right)\right)}{\partial x}+\ldots \tag{A7}$$

Substituting non-dimensional values (now non-tilda values are dimensionless, 0-quantities and L are reference values) we obtain:

$$\rho_0 U_0\frac{\partial \rho u}{\frac{\tilde{L}}{\tilde{U}_0}\partial \vartheta}=-\rho_0 {U_0}^2\frac{\partial\left(\rho u^2+p\right)}{L\partial x}+\ldots+\frac{\partial\frac{U_0\mu_0}{L}\left(\mu\left(\frac{2}{3}\frac{\partial u_k}{\partial x_k}+\frac{\partial u}{\partial x}+\frac{\partial u}{\partial x}\right)\right)}{L\partial x}+\ldots \tag{A8}$$

Then, dividing everything by $\frac{\rho_0 U_0{}^2}{L}$ we get:

$$\frac{\partial \rho u}{\partial \vartheta} = -\frac{\partial\left(\rho u^2 + p\right)}{\partial x} + \ldots + \frac{\mu_0}{\rho_0 U_0 L}\frac{\partial\left(\mu\left(\frac{2}{3}\frac{\partial u_k}{\partial x_k} + \frac{\partial u}{\partial x} + \frac{\partial u}{L\partial x}\right)\right)}{\partial x} + \ldots \tag{A9}$$

$$\frac{\partial \rho u}{\partial \vartheta} = -\frac{\partial\left(\rho u^2 + p\right)}{\partial x} + \ldots + \frac{1}{\mathrm{Re}_0}\frac{\partial\left(\mu\left(\frac{2}{3}\frac{\partial u_k}{\partial x_k} + \frac{\partial u}{\partial x} + \frac{\partial u}{L\partial x}\right)\right)}{\partial x} + \ldots \tag{A10}$$

The energy equation has the following form:

$$\frac{\partial e}{\partial \vartheta} = -\frac{u\partial\left(e + p\right)}{\partial x} + \ldots + \frac{\partial\left(\lambda\left(\frac{\partial T}{\partial x} + \ldots\right)\right)}{\partial x} + \ldots \tag{A11}$$

By substituting again non-dimensional values we have:

$$\frac{\rho U_0^3}{L}\frac{\partial e}{\partial \vartheta} = -\frac{\rho U_0^3}{L}\frac{u\partial\left(e + p\right)}{\partial x} + \ldots + \frac{\partial\left(\lambda\left(\frac{\gamma\lambda_0 U_0^3}{L c_p}\frac{\partial T}{\partial x} + \ldots\right)\right)}{L\partial x} + \ldots \tag{A12}$$

and dividing everything by $\frac{\rho U_0^3}{L}$

$$\frac{\partial e}{\partial \vartheta} = -\frac{u\partial\left(e + p\right)}{\partial x} + \ldots + \frac{\gamma\lambda_0}{c_p}\frac{1}{\rho_0 U_o L}\frac{\partial\left(\lambda\left(\lambda\frac{\partial T}{\partial x} + \ldots\right)\right)}{\partial x} + \ldots \tag{A13}$$

$$\frac{\partial e}{\partial \vartheta} = -\frac{u\partial\left(e + p\right)}{\partial x} + \ldots + \frac{\gamma\lambda_0}{\mu_0 c_p}\frac{\mu_0}{\rho_0 U_o L}\frac{\partial\left(\lambda\left(\lambda\frac{\partial T}{\partial x} + \ldots\right)\right)}{\partial x} + \ldots \tag{A14}$$

$$\frac{\partial e}{\partial \vartheta} = -\frac{u\partial(e+p)}{\partial x} + ... + \frac{1}{\mathrm{Re}_0 \mathrm{Pr}_0} \frac{\partial\left(\lambda\left(\lambda \frac{\partial T}{\partial x} + ...\right)\right)}{\partial x} + ... \qquad \text{(A15)}$$

A.3 Reference quantities

The choice of the actual value of *L*, U_0 and the other reference quantities is problem dependent. Here, the chosen primary reference quantities are:

- Reference length: $L = \tilde{D}_h$ is the hydraulic diameter

All of the other quantities are defined on the basis of the exit isentropic state, i.e. the state attained after an isentropic expansion from inlet stagnation state to exit pressure.

- Reference velocity: $U_0 = \tilde{a}_{is}$, exit isentropic speed of the sound
- Density: $\tilde{\rho}_0 = \tilde{\rho}_{is}$, exit isentropic density
- Viscosity: $\tilde{\mu}_0$, viscosity at isentropic exit temp.
- Conductivity: $\tilde{\lambda}_0$, conductivity at isentropic exit temp.

Where tildas identify *dimensional* quantities. And, thus the secondary reference quantities are:

- Reference temperature: $\frac{\gamma \tilde{a}_{is}^{\,2}}{c_p}$, i.e., the isentropic temperature
- Internal energy per unit volume: $\tilde{\rho}_0 \tilde{U}_0^2$
- Pressure: $\tilde{\rho}_0 \tilde{U}_0^2$

- Time: $\frac{\tilde{L}}{\tilde{U}_0}$

A.4 Exit isentropic state

Given the inlet stagnation temperature $\tilde{T}_0$, the exit isentropic conditions are computed as:

$$\tilde{T}_{is} = \frac{\tilde{T}_0}{1 + \frac{\gamma - 1}{2} Ma_{is}^2} \tag{A16}$$

$$\tilde{a}_{is} = \sqrt{\gamma R \tilde{T}_{is}} \tag{A17}$$

$$\tilde{u}_{is} = Ma_{is} \sqrt{\gamma R \tilde{T}_{is}} \tag{A18}$$

A.5 Non-dimensional groups definitions

$$Ma_{is} = \frac{\tilde{u}_{is}}{\tilde{a}_{is}} = \frac{\tilde{u}_{is}}{\sqrt{\gamma R \tilde{T}_{is}}} \tag{A19}$$

$$Ma_{is} = \tilde{u}_{is} \sqrt{\frac{1 + \frac{\gamma - 1}{2} Ma_{is}^2}{\gamma R \tilde{T}_0}} \tag{A20}$$

$$\tilde{u}_{is} = Ma_{is} \frac{\sqrt{\gamma R \tilde{T}_0}}{\sqrt{1 + \frac{\gamma - 1}{2} Ma_{is}^2}} \tag{A21}$$

$$\mathrm{Re}_{is} = \frac{\tilde{u}_{is}\tilde{D}_h}{\nu} = Ma_{is}\frac{\sqrt{\gamma R\tilde{T}_0}}{\sqrt{1+\frac{\gamma-1}{2}Ma_{is}^2}}\frac{\tilde{D}_h}{\nu} \tag{A22}$$

$$\tilde{D}_h = \nu\frac{\mathrm{Re}_{is}}{Ma_{is}}\frac{\sqrt{1+\frac{\gamma-1}{2}Ma_{is}^2}}{\sqrt{\gamma R\tilde{T}_0}} \tag{A23}$$

A.6 Flux non-dimensionalization

In the code the heat flux is normalized via the group $\mu\frac{a_{is}^2}{\tilde{D}_h}$, so that:

$$\tilde{q}_w = q_w\mu\frac{a_{is}^2}{\tilde{D}_h} \tag{A24}$$

$$\tilde{q}_w = \lambda q_w\frac{c_p\mu}{\lambda}\frac{a_{is}^2}{c_p\tilde{D}_h} \tag{A25}$$

$$\tilde{q}_w = \lambda q_w\,\mathrm{Pr}\frac{a_{is}^2}{c_p\tilde{D}_h} \tag{A26}$$

$$\tilde{q}_w = \lambda q_w\frac{\mathrm{Pr}}{\gamma}\frac{\gamma a_{is}^2}{c_p\tilde{D}_h} \tag{A27}$$

$$\tilde{q}_w = \lambda\frac{\partial T}{\partial y}\frac{\gamma a_{is}^2}{c_p\tilde{D}_h} \tag{A28}$$

$$\tilde{q}_w = \lambda\frac{\partial\tilde{T}}{\partial y} \tag{A28}$$

$$q_w\frac{\mathrm{Pr}}{\gamma} = \frac{\partial T}{\partial y} \tag{A30}$$

ACKNOWLEDGMENTS

In the first place I would like to express my sincere gratitude to Professor Giulio Croce, my PhD supervisor, who always provided his guidance, helpfulness, assistance, ideas, support and encouragement during the whole research period.

Then I would like to thank the University of Udine and, in particular, the DIEGM Department for giving me this opportunity and letting me use their facilities to carry out the work.

Lastly, a thank you to all the people that have supported and encouraged me during the PhD course.